國立台灣大學 電機工程學研究所

博士論文

指導教授：李百祺 教授

以同調因子為基礎之超音波可適性影像

Coherence-Factor-Based Adaptive Ultrasound Imaging

研究生：李夢麟　撰

中華民國九十三年一月

中文摘要

因聲波在人體不同組織中的傳播速度並不均勻，而在超音波影像系統中，通常是假設聲速為定值，並依此計算聚焦用的延遲，使得超音波影像系統聚焦成像時產生誤差，這樣的聚焦誤差，亦稱之為相位偏移(phase aberration)。該誤差降低了信號間的同調性，往往會提高超音波陣列影像系統的波束旁瓣，進而造成超音波聚焦及影像品質的下降。在本論文中，我們基於同調因子(coherence factor, CF)此參數的特性及概念，提出了二項可適性旁瓣消除技術 – 以廣義同調因子(generalized coherence factor, GCF)為基礎之可適性權重技術以及可適性接收孔徑技術，來降低因相位偏移對影像品質所造成的影響。其中，同調因子是用來量化探頭通道信號間同調性的參數，因而亦可作為聚焦品質的指標。

在所提出的可適性權重技術中，所使用的權重係數 – 廣義同調因子，是由施加適當接收延遲後的探頭通道信號，其沿著孔徑方向的空間頻譜衍生而來。廣義同調因子的定義為該空間頻譜於某低頻區域的能量與頻譜總能量的比值。本論文中證明該頻譜低頻的成份對應通道信號同調的部份，而高頻的成份則對應到非同調的部份。此外，當低頻區域僅取直流(dc)成份時，廣義同調因子便簡化為同調因子，即同調因子為廣義同調因子的特例。廣義同調因子亦可作為聚焦品質的指標，因此廣義同調因子被選為此技術中的權重係數，用來消除波束旁瓣以改進影像的對比解析度。本論文中對於廣義同調因子的特性，包括訊雜比(signal-to-noise ratio)及探頭通道數的影響，亦加以探討。

另外，在所提出的可適性接收孔徑技術中，同調因子則被用來作為分辨波束主瓣及旁瓣信號的閾值(threshold)。一旦分辨出主瓣及旁瓣信號後，便可找出每個影像點上最佳的接收孔徑大小，來加強主瓣的信號，壓低旁瓣的信號。因此，便可減少相位偏移所造成影像品質的下降。此外，廣義同調因子亦可取代同調因子作為分辨信號源的閾值，然而為了提高運算的效率，故在此技術中我們採用同調因子作為閾值。

在本論文中，使用模擬及實驗取得的超音波信號來驗證我們所提出這二項可適性旁瓣消除技術的效能。這二項技術的效能亦與另一種旁瓣消除技術 – 平行可適性接收補償法(parallel adaptive receive compensation algorithm)相比較。我們所提出的方法對於影像品質的改進可以與平行可適性接收補償法相匹敵，但是所需的運算量卻較低。此外，因我們所提出的技術不管造成聚焦誤差的來源，而是直接將旁瓣信號於影像強度上的貢獻加以壓低，所以這二項技術也可延伸到其他成像問題上。例如，在本論文中，廣義同調因子權重技術便延伸用來改善以傅利葉轉換(Fourier transform)為基礎之平行接收波束成像法以及應用於高頻超音波影像之合成孔徑聚焦技術的影像品質。

Abstract

Focusing errors resulting from sound-velocity inhomogeneities in human tissue, also known as phase aberrations, reduce the signal coherence and hence degrade the focusing quality. Such errors are often associated with un-wanted sidelobe contribution from off-axis targets in a coherent array imaging system. In this dissertation, two adaptive sidelobe-reduction techniques – the adaptive weighting technique using the generalized coherence factor (GCF) and the adaptive receive aperture technique – are proposed based on the concept of coherence factor (CF). The CF is a quantitative measure of coherence of the received signals, and thus can be used as a focusing quality index.

For the adaptive weighting technique, the GCF is derived from the spatial spectrum of the received aperture data after proper receive delays have been applied. It is defined as the ratio of the spectral energy within a prespecified low-frequency range to the total energy. It is demonstrated that the low-frequency component of the spectrum corresponds to the coherent portion of the received data, and that the high-frequency component corresponds to the incoherent portion. In addition, the GCF reduces to the CF if the coherent portion of the signal is restricted to dc only. Because the GCF is also a focusing quality index, it can be used as a weighting factor during image formation to suppress the sidelobe level and thus to improve the contrast resolution. Characteristics of the GCF, including effects of the signal-to-noise ratio and the number of channels, are also discussed in this dissertation.

For the adaptive receive aperture technique, the CF is used as a threshold to distinguish the mainlobe signal from the sidelobes. Once the mainlobe and the sidelobes are distinguished, the receive aperture size at each imaging position can be optimally determined so that the mainlobe signals are enhanced and the sidelobe signals are suppressed. Thus, image quality degradation resulting from sound-velocity inhomogeneities can be reduced. Note that the CF thresholding can also be generalized to GCF thresholding. Nonetheless, CF is used in this case due to the implementation efficiency.

Simulations and real ultrasound data are used to evaluate the efficacy of the two proposed techniques. The two proposed techniques are also compared with the parallel adaptive receive compensation algorithm. It is found that the improvement in image quality obtained with the proposed techniques rivals that of the conventional technique with lower computational complexity. Note that the proposed techniques

can be extended to other imaging problems because they reduce un-wanted sidelobe contributions regardless of the source of the focusing errors. In this dissertation, the GCF weighting technique is extended to improve the Fourier-transform-based parallel receive beam formation and the synthetic aperture focusing technique in high-frequency ultrasound imaging.

Table of Contents

List of Figures

List of Tables

Chapter 1 Introduction

1.1 Array Beamformation

The process of steering and focusing received array signals in ultrasonic array imaging to a particular image point is also known as “array beamformation”. Array beamformation is typically achieved using the delay-and-sum approach, in which the ultrasound signal received by each array channel is delayed according to the geometrical path-length difference prior to being summed across the aperture. A real-time ultrasonic imaging system usually assumes a constant sound velocity when calculating the time delays required for beam formation. Fig. 1.1 illustrates the delay-and-sum based array beamformation architecture in a phased array ultrasound imaging system. A phased-array ultrasound imaging system consists of a 1D array transducer for transmitting and receiving acoustic signal. For one transmit event, each array element receives the back-scattered signal from a particular image point at different times due to the geometrical path-length difference between the imaging point and array elements. The relative time delays across the array are also known as the delay profile as illustrated in Fig.1.1. With the delay profile, the back-scattered signals from the image point can then be added constructively, and the coherently summed signal is then sent to the beam buffer. The transmit beamformation can be viewed as the reversal of receive beamformation.

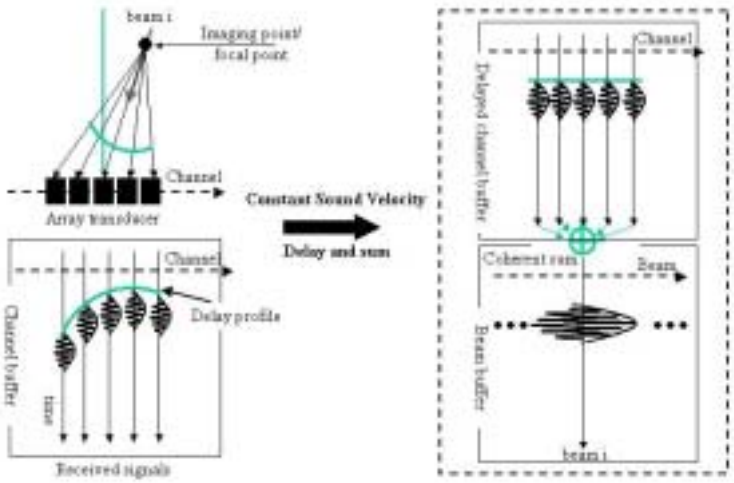

Fig. 1.1. Illustration of delay-and-sum based array beamformation in a phased array imaging system.

1.2 Beamformation Errors

From section (1.1), it is known that focusing in ultrasonic array imaging is typically achieved using the delay-and-sum approach. The focusing quality of such an approach, however, is inherently susceptible to focusing imperfections arising from deviations between the applied time delays and the actual propagation delays. Such imperfections include delay quantization errors, fixed transmit focusing, and sound-velocity inhomogeneities. The imperfections must be corrected if the spatial resolution is to approach the diffraction limit. Many techniques have been proposed to reduce the focusing errors.

1.2.1 Delay Accuracy

Several papers and patents have addressed the delay-accuracy requirements and implementation issues for dynamic focusing [1]–[8]. Coherence of the received signal is directly related to the delay accuracy, and a low coherence results in high sidelobes in the radiation pattern and degrades the contrast resolution. In order to achieve the required delay accuracy, most current digital systems perform real-time data interpolation in order to increase the effective data sampling rate. Considering the large number of system channels in such systems, real-time interpolation results in complicated system architectures.

1.2.2 Fixed Transmit Focusing

Another contributor to focusing imperfections is fixed transmit focusing [9]–[15]. Current real-time array imaging systems perform fixed focusing on transmit and dynamic focusing on receive. The focusing quality of such a system is less than optimal at imaging depths away from the transmit focal zone. Fully realizing the image quality achievable by an array imaging system requires the use of dynamic transmit focusing. Various methods have been proposed to increase the depth of transmit focus. One straightforward method is to simply apodize the transmit aperture [1]. Although apodization extends the transmit focal zone, it also degrades lateral resolution. Another method based on nondiffracting beam propagation has also been proposed [9], [10]. Although a nondiffracting beam produces a longer transmit focal zone, high sidelobes are also introduced.

1.2.2.1 Retrospective Dynamic Transmit Focusing Technique

As an alternative, a retrospective dynamic transmit focusing technique suitable for

real-time applications has been proposed [14], [15]. This technique treats dynamic focusing as a deconvolution problem, with the length of the transmit focal zone being extended by filtering the pre-detection image data. Fig. 1.2 illustrates the concept of the retrospective focusing technique. An out-of-focused image can be viewed as the convolution of an out-of-focused pulse-echo beam pattern with a scattering distribution function. Deconvolution for acquiring a focused image is done by laterally filtering the image data after beam formation and before envelope detection. Such a filter (e.g., inverse filter illustrated in Fig. 1.2) is range dependent. Based on the discrete spatial Fourier transform (FT) relationship between a beam pattern and the corresponding aperture function, it is straightforwd to see that spectrum of the inverse filter is the ideal pulse-echo effective aperture (i.e., dynamic focusing on both transmit and receive) divided by the out-of-focused pulse-echo aperture function, as illustrated in Fig. 1.2.

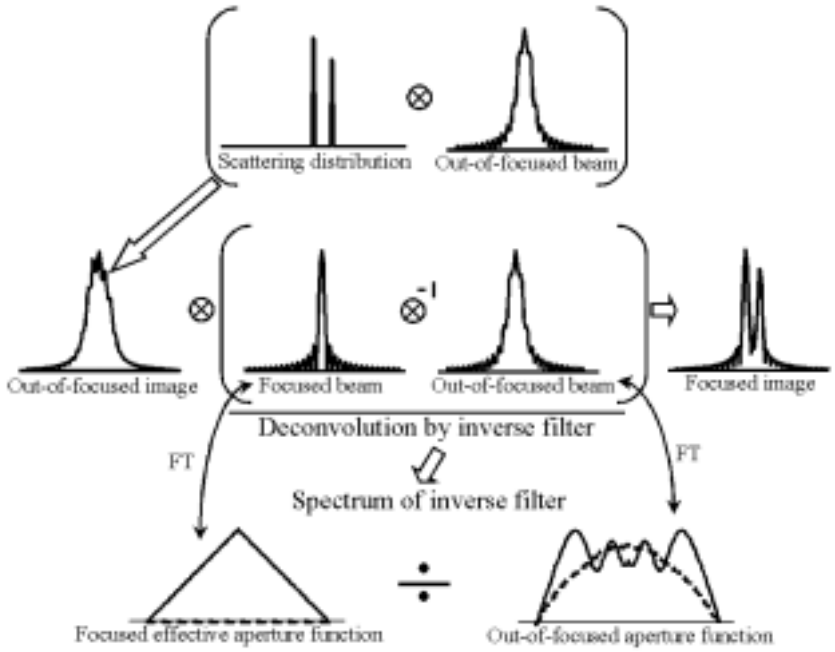

Fig. 1.2. Illustration of the retrospective dynamic transmit focusing technique. Focused beam means ideal pulse-echo beam pattern (i.e., dynamic focusing on both transmit and receive). $\otimes$ represents convolution; $\otimes^{-1}$ denotes deconvolution; $\div$ denotes division.

Robust results can be obtained using the inverse filter only if there are no singular points (i.e., points with small amplitudes) and the SNR is sufficiently high. Otherwise, direct application of the inverse filter amplifies the noise and degrades the beam quality. In addition, the inverse filter with the number of taps equaling the number of beams in the image is also not practical. Hence, an alternative filtering approach based on a minimum mean squared error criterion is used. The filter is also known as the optimal filter in the sense that the mean squared error between the filter

output and a desired beam pattern is minimized. The desired beam pattern is typically the dynamically focused beam at the same image position. Let the column vector $\underline{d}$ represent the desired beam pattern, the column vector $\underline{b}$ be the out-of-focused beam pattern and the column vector $\underline{f}$ describes the filter coefficients, the optimal filter can be express as

$$\underline{f}^{opt} = (B^H B)^{-1} B^H \underline{d}, \tag{1.1}$$

where H denotes the Hermitian conjugate and $B\underline{f}$ is the matrix representation of the convolution of $\underline{b}$ and $\underline{f}$. A system block diagram for retrospective focusing is illustrated in Fig. 1.3.

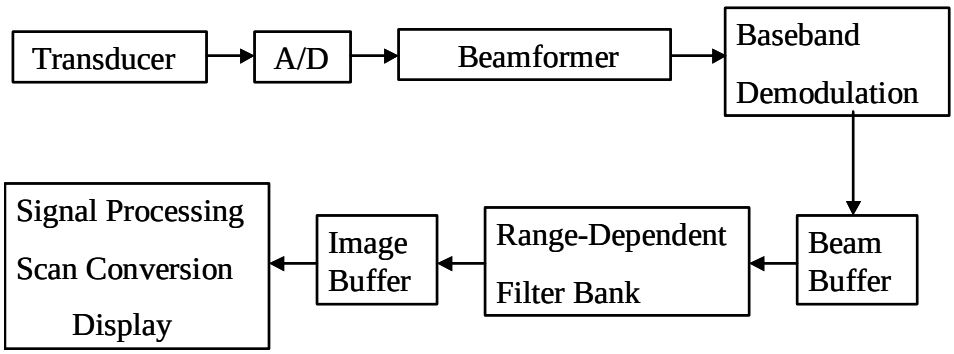

Fig. 1.3. System block diagram for retrospective focusing.

The optimal filter or the inverse filter converts a distorted pulse-echo aperture function into an ideal one. Hence, effectiveness of the filter is primarily determined by characteristics of the aperture function and the filter length. First, the effective width of the aperture function fundamentally limits the width of the filtered beam. The wider the aperture is, the narrower the beam width can be achieved. Second, singular points within the aperture affect robustness of the deconvolution process. To evaluate performance of the filter based approach, pulse-echo effective apertures with all possible combinations of the transmit and the receive focal depths are studied.

Without loss of generality, a 1-D array focused at range R_0 and zero steering angle is assumed. Further assuming continuous wave propagation, the phase ψ_n of the one-way aperture at range R can be written as [14]

$$\phi_n = k \frac{x_n^2}{2} \left(\frac{1}{R} - \frac{1}{R_0} \right), \tag{1.2}$$

where k is the wave number and x_n is the distance between the n-th element and the

array center. Note that the phase is equal to zero at the focal depth, whereas quadratic phase across the aperture exists in the out-of-focused region. Since the convolution of transmit and receive apertures is the pulse-echo effective aperture, the quadratic phase distorts the pulse-echo effective aperture and possibly generates singular points. In the examples shown below, a 128 element 1-D array with a 3.5 MHz center frequency and half-wavelength pitch is assumed. The sound velocity is 1.48 mm/us.

Fig. 1.4 Shows the -6 dB and –30 dB aperture widths of pulse-echo effective apertures with all possible combinations of the transmit and the receive focal depths. The widths are normalized to the corresponding widths of the ideal aperture function. The horizontal axis is the transmit focal depth, the vertical axis represents the receive focal depth and the target depth is fixed at 80 mm. The image brightness represents the normalized effective aperture width. The following observations are made. First, both the –6 dB and the –30 dB widths are the largest along the diagonal (upper left to lower right) where the transmit and receive focal depths are the same. Second, the horizontal line with the receive focus at 80 mm represents fixed transmit and dynamic receive focusing since the target depth is also at 80 mm. Third, the upper right region corresponds to the cases where the transmit focus is deeper and the receive focus is shallower than the target depth. Fourth, the lower left region represents the cases that the transmit focus is shallower and the receive focus is deeper than the target depth. In all cases, fixed transmit and fixed receive focusing at the same depth has the largest width. Thus, the best performance of the retrospective focusing technique is expected.

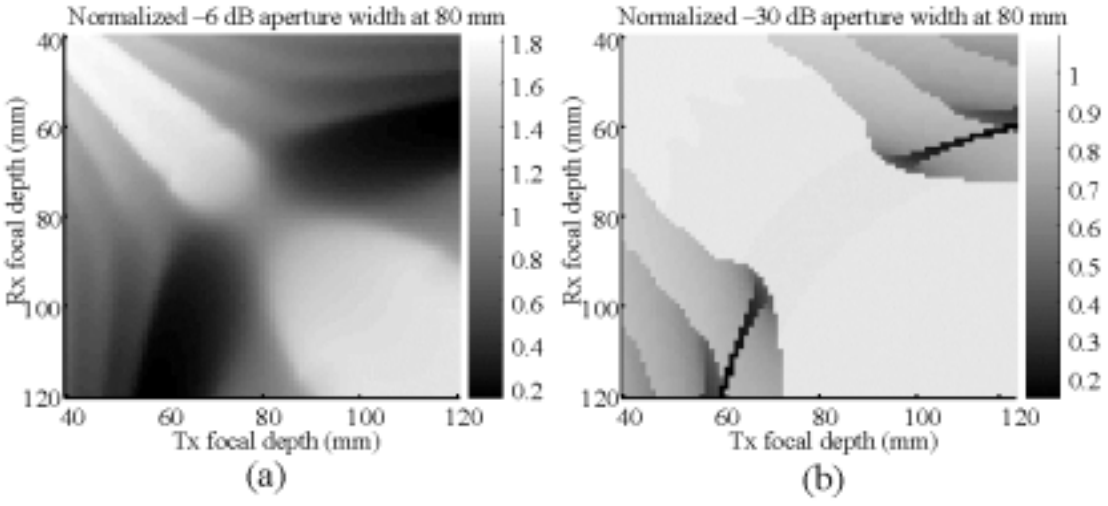

Fig. 1. 4. Normalized –6 dB and –30 dB effective aperture width

Fig. 1.5 shows 40 dB images of a six-wire phantom for dynamic transmit and dynamic receive focusing (Fig. 1.5(a)), fixed transmit focusing at 60 mm and dynamic receive focusing before filtering (Fig. 1.5(b)) and after filtering (Fig. 1.5(c)), fixed

transmit and fixed receive focusing at 60 mm before filtering (Fig. 1.5(d)) and after filtering (Fig. 1.5(e)). Note that the images are sector scan images prior to scan conversion and the different wires along different directions are aligned along the same line for ease of display. The vertical axis is the azimuth and the horizontal axis is the range. Comparing Fig. 1.5(d) to Fig. 1.5(e), the beam quality with fixed transmit and fixed receive focusing is significantly improved with filtering. It is also shown that the filtering technique with fixed receive focusing (Fig. 1.5(e)) can provide similar imaging performance to that of the image shown in Fig. 1.5(c) (i.e., dynamic receive focusing with filtering).

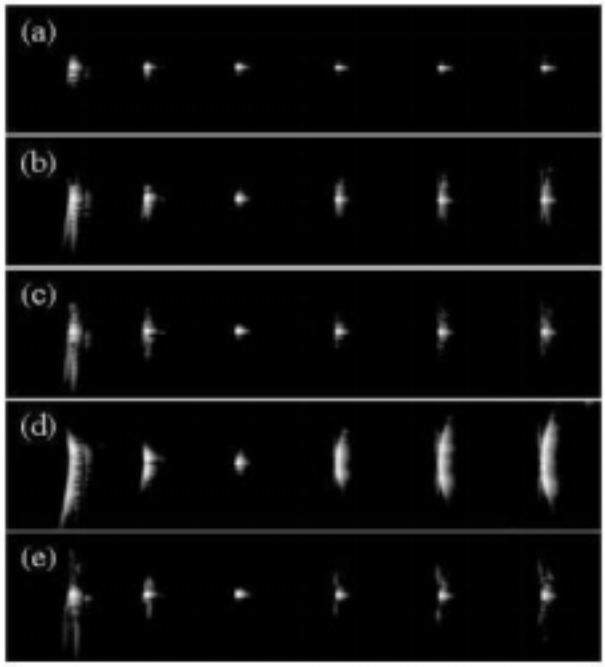

Fig. 1.5. Images of six wires over a 40 dB dynamic range. (a) is dynamic transmit and dynamic receive focusing. (b) is fixed transmit focusing at 60 mm and dynamic receive focusing. (c) is (b) with the retrospective filtering technique. (d) is fixed transmit and fixed receive focusing at 60 mm. (e) is (d) with the retrospective filtering technique.

Fig. 1.6 shows 30 dB images in the vicinity of a cyst at 65 mm. The vertical axis is the range and the horizontal axis represents the azimuth. Fig. 1.6(a) is the ideal image with dynamic transmit and dynamic receive focusing. Figs. 1.6(b) and (d) are the unfiltered images corresponding to cases with fixed transmit focusing at 120 mm and dynamic receive focusing and with fixed transmit and fixed receive focal depth at 120 mm, respectively. Figs. 1.6(c) and (e) are the filtered images corresponding to Figs. 1.6(b) and (d), respectively. It is shown that detection of the cyst is improved for fixed receive focusing. The cyst detectability for fixed receive focusing with filtering is similar to that for dynamic receive focusing.

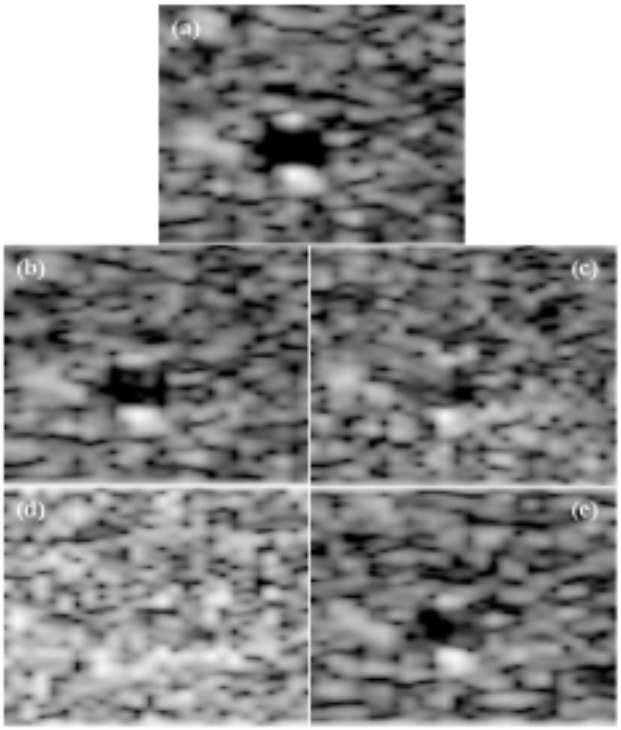

Fig. 1.6. 30 dB images of the anechoic cyst in a tissue mimicking phantom. (a) is dynamic transmit and dynamic receive focusing. (b) is fixed transmit focusing at 120 mm and dynamic receive focusing. (c) is (b) with the retrospective filtering technique. (d) is fixed transmit and fixed receive focusing at 120 mm. (e) is (d) with the retrospective filtering technique.

Figs. 1.5 and 1.6 suggests that the complex dynamic receive focusing circuit can be replaced by a simple 1-D filter bank at the beam former output. Thus, for the filtering technique with fixed receive focusing, hardware complexity is substantially reduced without sacrificing the imaging performance. Note that in the retrospective focusing technique, the out-of-focused beam pattern needs to be known in advance for filter design. However, the out-of-focused beam pattern generally is not well known in clinical situation. Therefore, the effectiveness of the retrospective dynamic transmit focusing technique is limited.

1.2.3 Sound-Velocity Inhomogeneities

Another major source of focusing errors is sound-velocity inhomogeneities [16]–[25]. As mentioned previously, a real-time ultrasonic imaging system usually assumes a constant sound velocity when calculating the time delays required for beam formation. However, the sound velocity in the human tissue varies over a wide range, as listed in Table 1-1. In clinical situation, fat is the major source resulting in the sound-velocity inhomogeneities [16], [17]. Fig. 1.7 illustrates how these sound-velocity inhomogeneities introduce time-delay errors to a phased array ultrasound imaging system. These sound-velocity inhomogeneities cause deviations

between the actual relative receive delays across the array and the applied time delays (e.g., the delay profile illustrated in Fig. 1.1). Therefore, delaying the received signals by the default delay profile is likely to produce time-delay errors in this case. Such time-delay errors, also known as the aberration profile, reduce the coherence of the delayed signals and thus degrade both spatial and contrast resolutions [16], [17]. Such sound-velocity inhomogeneities are also known as phase aberrations. Many methods have been proposed to restore the degraded resolution.

Table 1.1. Velocity of pertinent materials and biological tissues at room temperature (20-25^{o}C)

Medium	Velocity (m/sec)
Water	1484
Air	343
Blood	1550
Myocardium (perpendicular to fiber)	1550
Fat	1450
Liver	1570
Kidney	1560
Skull bone	3360

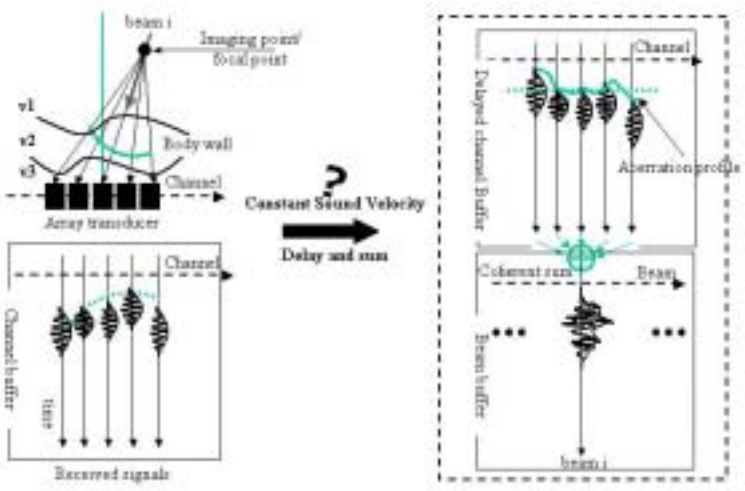

Fig. 1.7. Illustration of how time-delay errors are introduced by sound-velocity inhomogeneities.

1.2.3.1 Correlation-Based Technique

The correlation-based technique has been the most widely explored technique for the correction of phase aberrations. Flax and O'Donnell model the effects of sound-velocity inhomogeneities as a near-field phase screen placed in front of the transducer [18]–[20]. In this model, velocity inhomogeneities simply produce

time-delay errors across the array. Correlation functions of signals from either adjacent channels [18] or between individual channels and the beam sum are used to estimate the time-delay errors (i.e., aberration profile illustrated in Fig. 1.7) [20]. These estimates are then applied to compensate both the transmit and the receive focusing delays. Subsequent work has demonstrated that sound-velocity inhomogeneities introduce time-delay errors as well as wavefront distortion [16], [17]. Thus, sound-velocity inhomogeneities can also be modeled as a displaced phase screen positioned some distance away from the transducer surface [21]. In this model, received waveforms are propagated back to an optimal depth before the correlation function is calculated [21]. The other approach to correcting for distributed phase errors is the phase-conjugation technique [22]. Since the wavefront distortion can be characterized as nonlinear phase shifts in the frequency domain, a phase-conjugate filter dividing the spectrum into subbands can correct the nonlinear phase before the time-delay errors are estimated. Although the specific details are different, all the above methods utilize the correlation function to find time-delay errors. Unfortunately, since tissue inhomogeneities are likely to be three-dimensional, a two-dimensional array is required to avoid integration errors, and it has been the limiting factor of the clinical application of the correlation techniques with 1-D arrays [23]–[25].

1.2.3.2 Adaptive Sidelobe Reduction Technique

Unlike the correlation-based techniques, an alternative adaptive sidelobe-reduction approach has also been developed to minimize focusing errors. These techniques can be applied regardless of the source of the artifacts and the dimensionality of the array [26]–[29]. In other words, such an approach does not directly estimate propagation delay errors. Instead it estimates and reduces the undesired sidelobe contribution (i.e., the contribution of off-axis scatterers to the on-axis signal). One such example is the parallel adaptive receive compensation algorithm (PARCA) technique [26]–[28]. The PARCA approach requires the use of parallel receive beams around a fixed transmit beam (also known as single transmit imaging [30]) to estimate the sidelobe contribution. To estimate the sidelobe contribution, the original version of PARCA also requires the application of the total least-squares (TLS) method for every point in the image [28]; hence it is computationally demanding. To simplify the technique, a modified version called PARCA2 was proposed [29]. Here the formation of parallel beams is approximated by Fourier transforming the channel data, and an iterative scheme is used to replace the TLS method [31].

1.3 Coherence Factor

In the presence of focusing errors, coherence of the received signal is reduced and the sidelobes of the radiation pattern are elevated. A quantitative measure of the signal coherence has been previously described in the literature and is also known as the coherence factor (CF) [32], [33]. It is defined as

$$\mathrm{CF}(t) = \frac{\left|\sum_{i=0}^{N-1} S(i,t)\right|^2}{N\sum_{i=0}^{N-1}\left|S(i,t)\right|^2}, \tag{1.3}$$

where t is the time index, N is the number of array channels used for beam formation, and $S(i,t)$ is the received signal of channel i after proper receive delays have been applied [32]–[35]. The numerator in Eq. (1.3) represents the energy of the coherent sum obtained in a conventional delay-and-sum based beamformer, and the denominator is interpreted as the total incoherent energy which is N times the incoherence sum. According to the definition, the CF is a real, non-negative quantity ranging from 0 to 1. The maximum of CF occurs when the received array signals are identical across the array (i.e., perfectly coherent) [33]. That is, for an on-axis point target and with perfect focusing, the CF will be close to 1.

For diffuse scatterers, the analytic solution of CF can be derived using the van Cittert-Zernike theorem [32], [34]–[35]. Assuming that the signal power received by each channel is statistically identical, i.e.,

$$\sum_{i=0}^{N-1}\left|S(i)\right|^2 = N \cdot P, \tag{1.4}$$

where P is the power for each individual channel, and the cross-power between channels i and j is proportional to their correlation. Note that the time index is omitted here. The correlation can be described by the van Cittert–Zernike theorem:

$$\int S(i)S(j)^* dt = \left[1 - \frac{(i-j)}{N}\right]\int \left|S(i)\right|^2 dt = \left[1 - \frac{(i-j)}{N}\right]P. \tag{1.5}$$

Thus, the CF for a one-dimensional array is

$$\mathrm{CF} = \frac{\left|\sum S(i)\right|^2}{N\sum\left|S(i)\right|^2}$$

$$= \frac{\left(\overbrace{P+P+\cdots+P}^{N \text{ terms}}\right)+\left(\overbrace{\frac{N-1}{N}P+\frac{N-1}{N}P+\cdots+\frac{N-1}{N}P+\frac{N-1}{N}P}^{2(N-1) \text{ terms}}\right)+\cdots+\left(\frac{1}{N}P+\frac{1}{N}P\right)}{N(NP)}$$

$$= \frac{(1+1+\cdots+1)+\left(\frac{N-1}{N}+\frac{N-1}{N}+\cdots+\frac{N-1}{N}+\frac{N-1}{N}\right)+\cdots+\left(\frac{1}{N}+\frac{1}{N}\right)}{N^2}$$

$$= \frac{N+\frac{2}{N}\sum_{k=1}^{N-1}(N-k)^2}{N^2}$$

$$= \frac{2}{3}+\frac{1}{3N^2}. \qquad (1.6)$$

The CF approaches 2/3 for a one-dimensional array when N is sufficiently large. Note that Eq. (1.5) is applicable only when there is no focusing error.

1.4 Dissertation Organization

Focusing imperfections reduce the coherence of the received signal [32]. Low coherence results in high sidelobes in the radiation pattern and degrades the contrast resolution. Since CF describes the coherence of received array signals, the CF can be used as an index for focusing and image quality. In this dissertation, such a notion is adopted and applied to improve the degraded beam quality resulted from sound-velocity inhomogeneities. Specifically, two adaptive sidelobe-reduction techniques – the adaptive weighting technique using the generalized coherence factor (GCF) and the adaptive receive aperture technique – are proposed based on such a notion. With these, this dissertation is organized as follows.

In chapter 2, an adaptive weighting technique using the GCF is proposed to reduce the image quality degradation resulting from the sound-velocity inhomogeneities. The efficacy of the GCF weighting technique is demonstrated using simulations and real ultrasound data. The characteristics of the GCF are discussed. The GCF technique is also compared with the correlation-based technique and the

parallel adaptive receive compensation algorithm. In addition to the adaptive weighting technique proposed in chapter 2, an adaptive receive aperture technique based on the CF thresholding is proposed in chapter 3. Simulations and real ultrasound data are used to evaluate efficacy of the proposed technique on sidelobe reduction. The proposed technique is also compared with the parallel adaptive receive compensation algorithm.

Since the proposed techniques reduce un-wanted sidelobe contributions regardless of the sources of the focusing errors, they can be extended to other imaging problems. Chapter 4 extends the GCF weighting technique proposed in Chapter 2 to reduce the sidelobes of the Fourier transform (FT)-based formation of the parallel receive beams. In chapter 5, the GCF weighting technique developed for array beamforming is extended to improve the synthetic aperture focusing technique (SAFT) using a single crystal transducer. Its applications in high-frequency ultrasonic imaging are also discussed.

In chapter 6, the GCF weighting is compared with the low-pass filtered CF (LPF{CF}) weighting for imaging a speckle-generating target. The feasibility using LPF{CF} weighting to replace GCF weighting is discussed. Results of combination of the adaptive receive aperture technique and the adaptive weighing technique using LPF{CF} are also presented. This dissertation concludes in chapter 7. Future works are also described.

Chapter 2 GCF Weighting Technique

Sound-velocity inhomogeneities degrade both spatial and contrast resolutions. This chapter proposes a new adaptive imaging technique that uses the generalized coherence factor to reduce the focusing errors resulting from the sound-velocity inhomogeneities. The GCF is derived from the spatial spectrum of the received aperture data after proper receive delays have been applied. It is defined as the ratio of the spectral energy within a prespecified low-frequency range to the total energy. It is demonstrated that the low-frequency component of the spectrum corresponds to the coherent portion of the received data, and that the high-frequency component corresponds to the incoherent portion. Hence, the GCF reduces to the coherence factor, as defined in chapter 1, if the prespecified low-frequency range is restricted to dc only. In addition, the GCF is also an index of the focusing quality and can be used as a weighting factor for the reconstructed image. The efficacy of the GCF technique is demonstrated for focusing errors resulting from the sound-velocity inhomogeneities. Simulations and real ultrasound data are used to evaluate the efficacy of the proposed GCF technique. The characteristics of the GCF, including the effects of the signal-to-noise ratio and the number of channels, are also discussed. The GCF technique is also compared with the correlation-based technique and the parallel adaptive receive compensation algorithm: the improvement in image quality obtained with the proposed technique rivals that of the latter technique. In the presence of a displaced phase screen, this proposed technique also outperforms the correlation-based technique. Computational complexity and implementation issues are also addressed.

2.1 Frequency-Domain Interpretation of The Aperture Data

The channel data is the data received by each array channel after the focusing delays are applied prior to the beam sum. At a particular range, the time index is fixed and hence can be omitted. At this range, the data received by each channel i across the array is also called the aperture data, and can be denoted $S(i)$ for $i=0$ to $N-1$, where N is the total number of array channels. The N-point discrete Fourier spectrum of the

aperture data becomes

$$p(k) = \sum_{i=0}^{N-1} S(i) e^{-j2\pi(i-\frac{N}{2})d\frac{k}{Nd}} = e^{j\pi k} \sum_{i=0}^{N-1} S(i) e^{-j2\pi\frac{ik}{N}}, \qquad (2.1)$$

where $k = -N/2$ to $N/2-1$ is the spatial frequency index, and d is the pitch of the array with the array center defined as the zero-phase reference point. As described in [29], the Fourier spectrum across the array can be viewed as the approximation of multiple parallel receive beams centered at the transmit beam direction and equally spaced by $\Delta\sin\theta = \lambda/(Nd)$, where θ is the steering angle in a sector scan and λ is the wavelength. The dc component (i.e., $p(0) = \sum_{i=0}^{N-1} S(i)$) representing the coherent sum after typical delay-and-sum operations corresponds to the received signal from the transmit beam direction and the high-frequency components corresponds to the scattered signals from other angles than the transmit beam direction.

2.1.1 Point Targets

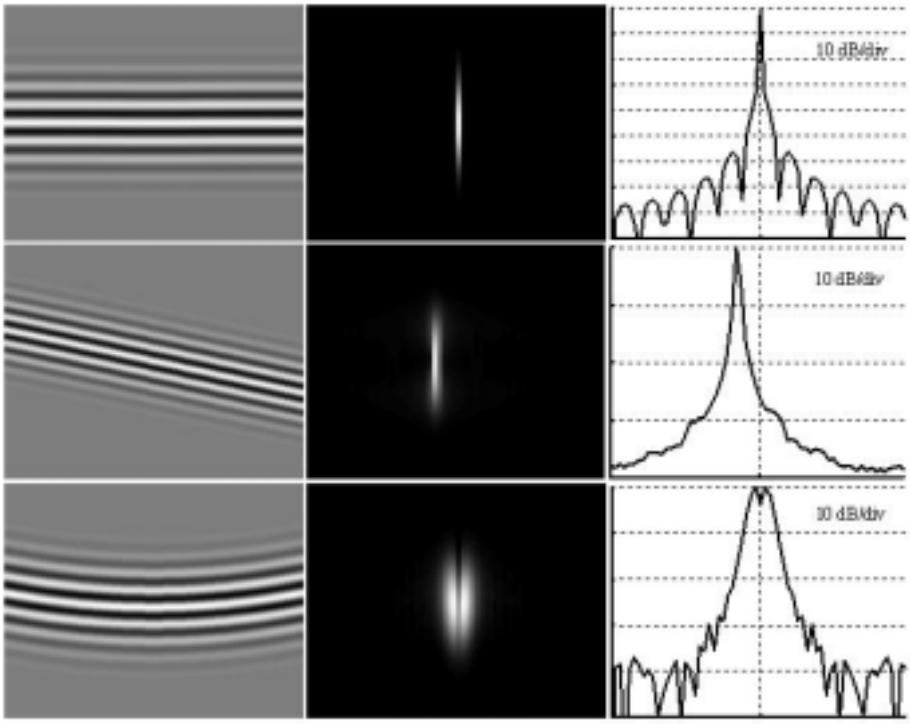

Fig. 2.1. Channel data and the corresponding spectrum over the aperture of a point target. The top panels are with ideal focusing, the middle panels are with a steering error, and the bottom panels are with a range focusing error. In each case, the left panel shows the channel data, with the horizontal axis representing the channel index and the vertical axis denoting the range; the middle panel shows the spectrum at each range; and the right panel is the projection of the data shown in the middle panel.

The top panels of Fig. 2.1 show the channel data and the associated spectra across the receive array for a focused point target located at 60 mm. In this figure and the subsequent simulations, the phased array had 64 elements with a center frequency of 3.5 MHz, and a half-wavelength pitch. The top-left panel in Fig. 2.1 shows the channel data, and the top-middle panel shows the corresponding one-dimensional Fourier transform of the aperture data at each range, with the horizontal axis representing either the spatial frequency index k from $-N/2$ to $N/2-1$ or $\sin(\theta)$ from -1 to $1-2/N$ (from left to right). Note that the channel data is demodulated to baseband and filtered before the Fourier transform is calculated along the array direction. Since all of the array channels receive identical data from a focused point target, the aperture data at a given range are constant. Hence, the spectrum of such aperture data becomes a sinc function. The sinc function is also identical to the continuous-wave radiation pattern of the same aperture, except that the index k is now related to the steering angle rather than the spatial frequency. The top-right panel is the projected spectrum of the middle panel along the range direction, with each vertical division representing 10 dB, and the vertical dashed line indicating dc (i.e., the transmit beam direction). Note that the maximum along the range direction is used for the projection.

The second row of Fig. 2.1 demonstrates the case where the point is moved to 9° from the center line with the other conditions being unchanged. This corresponds to a steering error of the receive array. It can be seen that the received channel data are no longer in phase, with the slope of the channel data corresponding to the direction of the point target. Thus, the aperture data at a particular range is modulated and the corresponding spectrum across the array becomes a shifted sinc function, as shown in the middle and the right panels. It is clearly shown that when a steering error is present, the energy in the coherent sum (i.e., the dc component) is non-negligible, although this energy is primarily concentrated in the object direction. In other words, the dc component (i.e., the beam sum) is the sidelobe contribution from the off-angle target, and this is what needs to be reduced as much as possible.

The bottom panels of Fig. 2.1 show the results where the focal point is moved to 30 mm while the point target is still located at 60 mm (i.e., a range focusing error). There is again a significant portion of the received signal in the non-dc portion of the spectrum (i.e., the angles outside of the transmit beam direction). Fig. 2.1 demonstrates the spectrum of the aperture data can be used to determine the focusing quality. The focusing quality is directly related to the ratio of the energy of the coherent sum to the total energy (i.e., the ratio of the energy of the received signal from the transmit beam direction to the total energy from all directions). Since the total spectral energy is N times the incoherent sum according to the Parseval's relation

for the discrete Fourier transform, which can be expressed as

$$\sum_{k=-N/2}^{N/2-1} \left|p(k)\right|^2 = N \cdot \sum_{i=0}^{N-1} \left|S(i)\right|^2 , \tag{2.2}$$

where $S(i)$ is the signal received by channel i [62], the ratio is the CF defined in chapter 1. Intuitively, if the focusing quality is good, the energy from the transmit beam direction is high (i.e., the energy is more concentrated at the dc). That is, good focusing quality results in a higher CF. In addition, the dc portion is also the coherent sum and the non-dc portion is related to the incoherent sum. Hence, the CF (or similar quantities) can be used as an index of the focusing quality and the basis of the proposed adaptive weighting technique. Also note that the coherent and incoherent sums are related to the main- and sidelobes of the radiation pattern. Thus, the CF also represents the ratio of mainlobe energy to total energy.

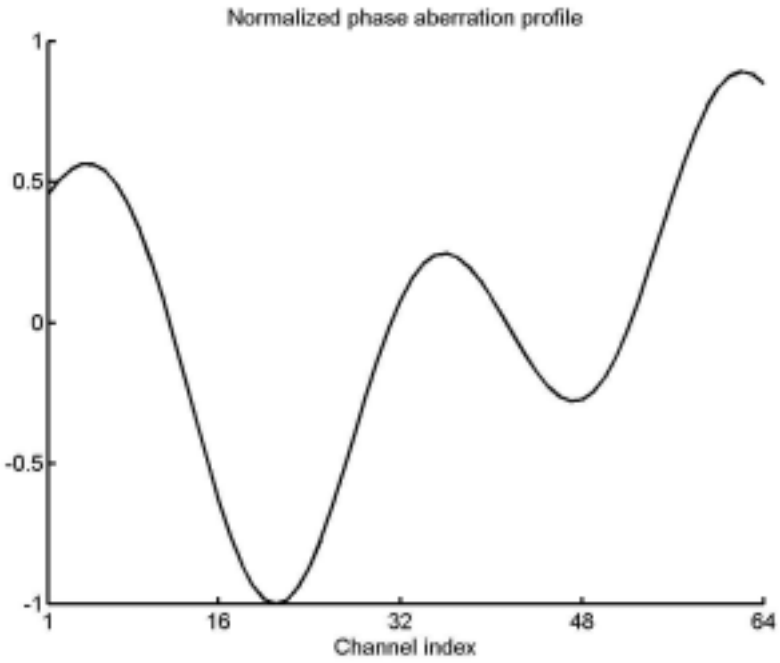

Fig. 2.2. The normalized phase-aberration profile used in the simulations of sound-velocity inhomogeneities. The horizontal axis is the channel index and the vertical axis is the normalized phase error. The correlation length is 5 mm.

Focusing errors due to sound-velocity inhomogeneities are also considered, using the normalized phase-aberration profile shown in Fig. 2.2. The horizontal axis is the channel index and the vertical axis shows the phase error after normalization. The profile has a correlation length of 5 mm, and the maximum phase error varies depending on specific simulation conditions. The results are shown in Fig. 2.3. The top panels of Fig. 2.3 show a maximum phase error of $\pi/4$ at the center frequency of

3.5 MHz, whereas the middle panels show a maximum phase error of π/2 at the center frequency of 3.5 MHz. According to [16], phase errors while imaging breast specimens are about π/2 at the simulated center frequency. Hence, the simulated phase error here is sufficiently large. Both conditions are for the near-field assumption, i.e., the time-delay errors occur at the face of the transducer. In the bottom panels, the same aberration profile used in the middle panels (i.e., π/2 maximum phase error) is moved to 20 mm away from the transducer. This figure shows that the CF decreases as the maximum aberration increases. However, the coherence for the case with a displaced phase screen is not necessarily lower than that for the near-field case. In other words, although the displaced phase screen generally decreases the similarity between signals received by adjacent channels, this does not necessarily result in a reduction in the signal coherence as determined by the spectrum of the aperture data.

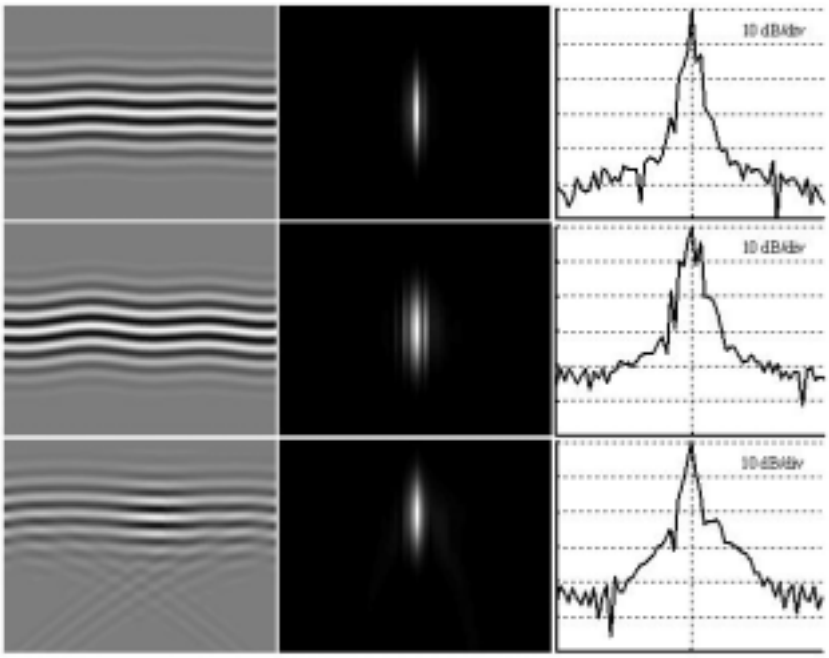

Fig. 2.3. Channel data and the corresponding spectrum over the aperture of a point target. The top panels are for a maximum phase error of π/4, and the middle and bottom panels are for a maximum phase error of π/2. The top and middle panels are for a near-field phase screen, whereas the bottom panels are for a displaced phase screen that is positioned 20 mm from the transducer. In each case, the left panel shows the channel data, with the horizontal axis representing the channel index and the vertical axis denoting the range; the middle panel shows the spectrum at each range; and the right panel is the projection of the data shown in the middle panel.

2.1.2 Speckle-Generating Targets

The results shown in Fig. 2.3 are for point targets; in clinical situations, speckle-generating targets are more likely to occur. Fig. 2.4 shows the results with a

speckle-generating target, where the top panels are for perfect focusing, and the middle and bottom panels are with the same aberration conditions as the ones used in the middle and bottom panels of Fig. 2.3, respectively. Although the general trend is still the same as in Fig. 2.3, in Fig. 2.4 the mainlobe generally becomes wider and the non-dc level also increases for a speckle-generating target. This is because a speckle-generating target inherently contains a certain degree of incoherence. Thus, with diffuse scatterers the definition of the CF needs to be modified to take such inherent incoherence of speckle-generating targets into consideration.

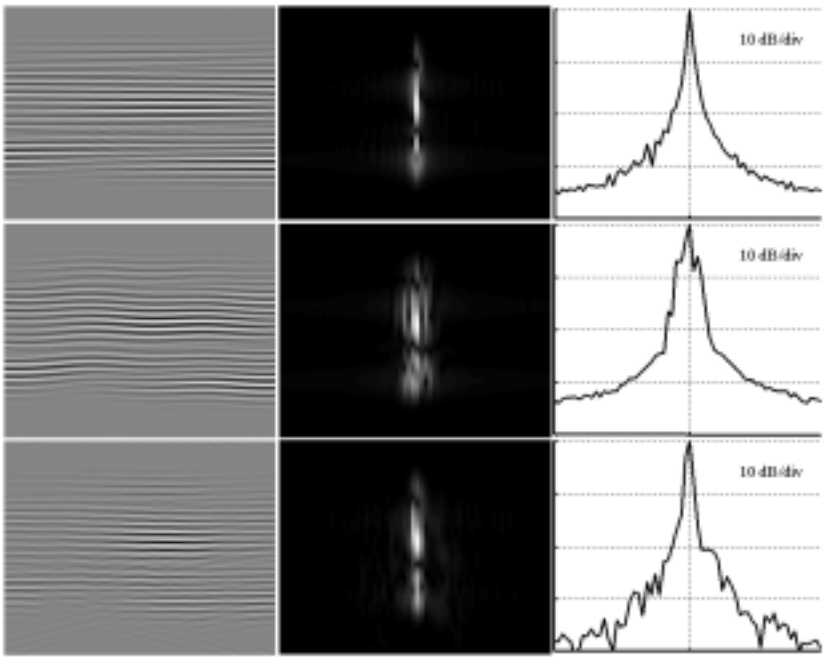

Fig. 2.4. Channel data and the corresponding spectrum over the aperture of diffuse scatterers. The top panels are for no phase error, and the middle and bottom panels are for a maximum phase error of $\pi/2$. The middle panels are for a near-field phase screen, whereas the bottom panels are for a displaced phase screen positioned 20 mm from the transducer. In each case, the left panel shows the channel data, with the horizontal axis representing the channel index and the vertical axis denoting the range; the middle panel shows the spectrum at each range; and the right panel is the projection of the data shown in the middle panel.

2.2 Adaptive Weighting Based on the GCF

Section (2.1) demonstrates that the effects of focusing errors are directly related to the ratio of the energy of the coherent portion of the received data to the total energy, and so an adaptive weighting technique can be developed based on this property. When the ratio is high the focusing quality is good, and thus the weighting is

high so that image intensity is maintained. On the other hand, the focusing quality is low when the ratio is low, and hence the weighting needs to be low to reduce artifacts. Furthermore, since the speckle-generating target inherently contains a certain degree of incoherence, the notion of CF is now generalized and will be referred to as the GCF. The GCF is derived from the spectrum of the aperture data after proper receive delays have been applied. Specifically, the GCF is defined as the ratio of the spectral energy within a prespecified low-frequency region to the total energy (i.e., the ratio of the energy received from the angles around the transmit beam direction to the total energy from all directions). The GCF over the aperture at a given range can be expressed as

$$\text{GCF} = \frac{\text{energy in a low - frequency region}}{\text{total energy}} = \frac{\sum_{k \in \text{low-frequency region}} |p(k)|^2}{\sum_{k=-N/2}^{N/2-1} |p(k)|^2}, \tag{2.3}$$

where $p(k)$ is the spectrum of the received array data, and N is the number of points in the discrete spectrum. The discrete Fourier transform can be efficiently computed using the fast Fourier transform (FFT), and N is equal to the number of channels in this case. The low-frequency region is specified by a cutoff frequency M_0 in the spatial frequency index (i.e., from $-M_0$ to M_0). The low-frequency region can be viewed as the received signal from the angles around the transmit beam direction. Note that an M_0 of zero means that the low-frequency range used to estimate GCF is restricted to dc only. The procedure is illustrated in Fig. 2.5(a).

Note that although derivation of the GCF requires the individual aperture data, the adaptive weighting only needs to be applied at each image point. In other words, the corrected signal $x_{\text{corrected}}$ of x at a given range can be expressed as

$$x_{\text{corrected}} = \text{GCF} \cdot x\,. \tag{2.4}$$

A system block diagram for the proposed GCF technique is shown in Fig. 2.5(b). After the echo signal is received and digitized by the A/D converter, the received RF data are demodulated down to baseband. The baseband beamformer applies proper dynamic receive delays and phase rotations to the baseband data before the data are stored in the channel buffer. The GCF is then estimated using the delayed baseband array data across the aperture at each range, and the GCF should be calculated for all range points. Then, the beam sum data are weighted by GCF. The weighting is done by multiplying the amplitude of the beam sum data by the corresponding GCF. The weighted data are then sent to the beam buffer for further signal processing, scan conversion, and display. Note that GCF can be efficiently computed via the FFT. The

computational complexity is relatively low, and no iteration is needed. In addition, as illustrated in Fig. 2.5(b), the proposed technique can be easily incorporated into a baseband beamformer.

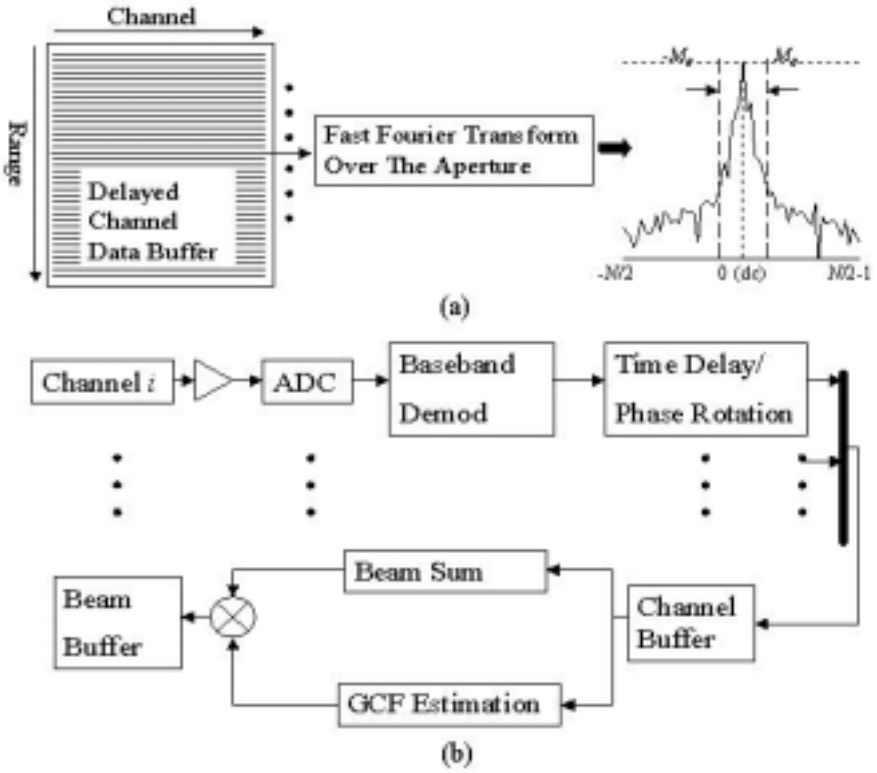

Fig. 2.5. (a) Schematic diagram showing how the generalized coherence factor (GCF) is calculated. (b) System block diagram for the GCF-weighting technique.

2.3 Simulation and Experimental Results

In this section, simulated ultrasound data are used to explore the efficacy of the GCF-weighting technique in compensating for the focusing errors resulting from sound-velocity inhomogeneities. The acoustic field simulation program Field II was employed to simulate the received signal at each array element [37]. The simulated phased array had 64 elements with a center frequency of 3.5 MHz, and a half-wavelength pitch. A sector scan from –30° to 30° was performed and Nyquist beam spacing was used. Two types of image objects – a point target and an anechoic object – were simulated. In addition to simulated data, emulated images using real ultrasound data are also presented.

2.3.1 Point Target Simulations

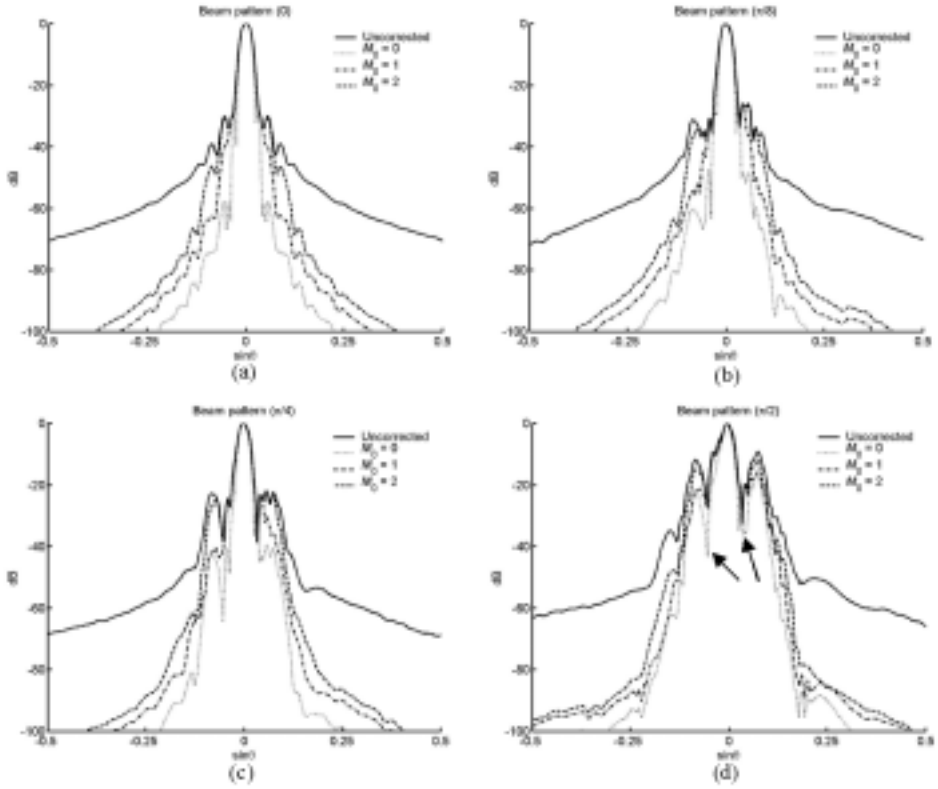

Fig. 2.6. Projected beam patterns for a point target. (a) No aberration. (b)–(d) π/8, π/4, and π/2 maximum phase errors, respectively, at the center frequency of 3.5 MHz. solid lines, uncorrected; dotted lines, GCF corrected with M_0=0; dashed–dotted lines, GCF corrected with M_0=1; dashed lines, GCF corrected with M_0=2.

First, a point target simulation with focusing errors due to sound-velocity inhomogeneities is used to evaluate the GCF technique and effects of the parameter M_0. Only a near-field phase screen was simulated for all aberrated cases. The used normalized aberration profile was the same as that shown in Fig. 2.2. For all aberrated cases, the aberration profile was applied on both transmit and receive. The transmit focal point was 30 mm from the transducer, and dynamic focusing was applied on receive. The point target was located at the depth of 30 mm. Fig. 2.6 shows the projected beam patterns for the point target under different aberration conditions and different values of M_0. Fig. 2.6(a) is the case for no aberration. Fig. 2.6(b) represents the case with a π/8 maximum phase error at the center frequency of 3.5 MHz. Fig. 2.6(c) shows the aberrated case with a π/4 maximum phase error, and Fig. 2.6(d) is the case with a π/2 maximum phase error. It is obvious from Fig. 2.6 that the beam quality is significantly improved after adaptive weighting for each aberration case and M_0 value: the far sidelobes are all significantly suppressed by more than 20 dB. The

suppression of the near sidelobe decreases as the maximum phase error and M_0 increase. Note that GCF weighting also suppresses the sidelobe level even if no aberration is present. This suggests that contrast improvement on unaberrated data can also be obtained due to reduced sidelobes. In general, the best performance of phase-aberration correction for a point target is obtained when M_0 is equal to zero (in terms of sidelobe reduction). However, the GCF- corrected beam profile with $M_0 = 0$ introduces larger variations in the near sidelobe level as indicated by the two arrows shown in Fig. 2.6(d). In this case, the uncorrected beam exhibits beam splitting due to large phase aberration. The corrected beam has lower sidelobes and makes beam splitting more pronounced. Such a situation does not occur for a larger M_0. In other words, a larger M_0, e.g. $M_0 = 1$, should be used to prevent such artifacts.

2.3.2 Anechoic Object Simulations

To further demonstrate the efficacy of the proposed GCF technique for targets with diffuse scatterers and potential improvement on contrast resolution, an anechoic cyst in a speckle-generating background was simulated. The center of the cyst was located at the depth of 30 mm. The image size was 15 mm in the lateral direction and 10 mm in the axial direction. The anechoic object had a diameter of 5 mm. Positions of the scatterers were uniformly distributed, and the scattering amplitudes were Gaussian distributed. Other simulation settings were the same as those in the point target simulations for sound-velocity inhomogeneities.

Fig. 2.7(a) shows the simulated image under a $\pi/4$ maximum phase error without correction. Figs. 2.7(b) and (c) show the corrected images with GCF weighting when M_0 was set to zero and one, respectively. Note that the images are sector-scan images prior to scan conversion, and display over a 50 dB dynamic range. The vertical axis represents range and the horizontal axis is azimuth. Fig. 2.7(a) shows that the $\pi/4$ maximum phase error results in degradation in image quality, as evidenced by the “fill in” in the anechoic cyst region. Figs. 2.7(b) and (c) show that detection of the cyst is improved after GCF correction for both M_0 values used in the simulations. However, the corrected image shown in Fig. 2.7(b) exhibits artificial black holes. The standard deviation of the image intensity was calculated in the background region indicated by the right-hand rectangular white box shown in Fig. 2.7(a). The standard deviation of Fig. 2.7(b) is 3.94 dB higher than that of Fig. 2.7(a), while the standard deviation of Fig. 2.7(c) is only 1.06 dB higher than that of Fig. 2.7(a). In other words, the GCF weighting introduces large intensity variations when M_0 is set to zero. These results suggest that it is inappropriate to set M_0 to zero for diffuse scatterers. In other words, the low-frequency region used to estimate GCF for diffuse scatterers should be wide

enough to include the inherent incoherence from a speckle-generating target. Thus, a larger M_0 is generally more preferable for this type of object.

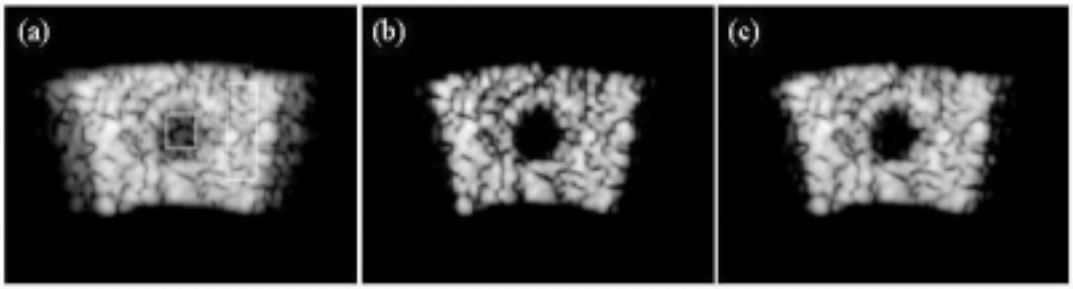

Fig. 2.7. Images of an anechoic cyst over a 50 dB dynamic range. The vertical axis is the range and the horizontal axis represents the azimuth. (a) $\pi/4$ maximum phase error at the imaging frequency of 3.5 MHz. (b) GCF-corrected image with M_0=0. (c) GCF-corrected image with M_0=1.

For the four maximum phase errors – 0 (i.e., no aberration), $\pi/8$, $\pi/4$, and $\pi/2$ – Fig. 8 shows the standard deviation in the background region after GCF correction as a function of M_0. Again, the standard deviation in the background is estimated from the region within the right-hand white box shown in Fig. 2.7(a). Also note that a M_0 value of –1 corresponds to no GCF correction being performed. Fig. 2.8 indicates that the standard deviation decreases as the value of M_0 increases. In addition, for M_0 equal to zero, the corresponding standard deviation after correction is much higher than that without correction. A large standard deviation may indicate the presence of image artifacts.

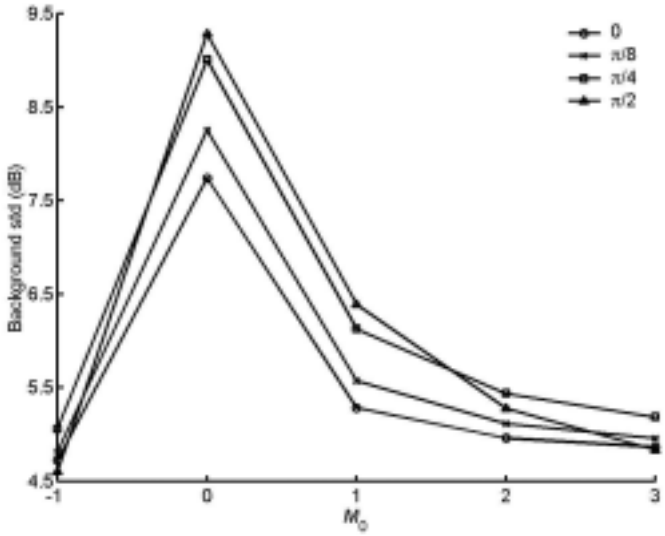

Fig. 2.8. Standard deviation in the background region after correction as a function of M_0. M_0= –1 corresponds to no correction being performed.

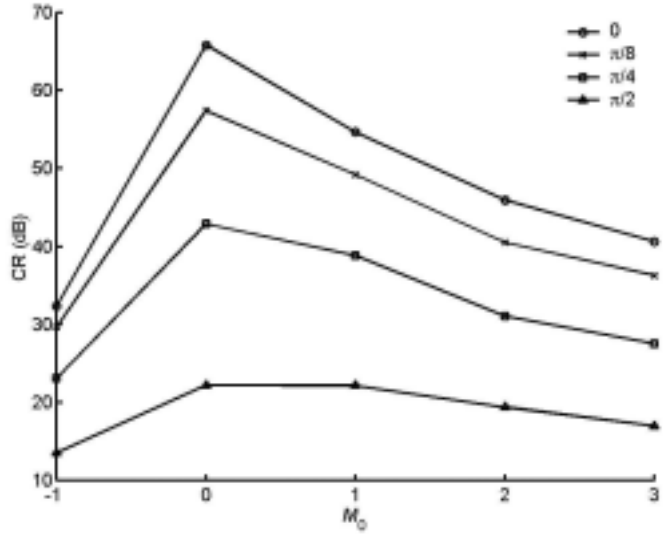

Fig. 2.9. CR after correction as a function of M_0 for different maximum phase errors.

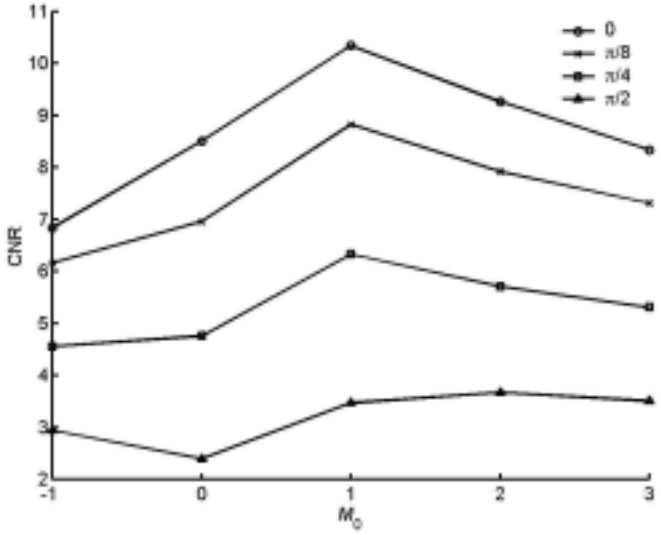

Fig. 2.10. CNR after correction as a function of M_0 for different maximum phase errors.

Two indices related to contrast resolution are employed to evaluate the improvement in image quality: (i) the contrast ratio (CR) is defined as the ratio of the mean value in the background to the mean value in a cyst region [19], and (ii) the contrast-to-noise ratio (CNR) is defined as the CR divided by the standard deviation of image intensity in the background region [20] (note that the background and cyst regions are indicated by the right- and left-hand white boxes shown in Fig. 2.7(a), respectively). Fig. 2.9 shows the CR after correction as a function of M_0 for different maximum phase errors. The figure shows that the CR decreases as M_0 increases. Moreover, the contrast enhancement decreases as the maximum phase error increases.

The CNR after correction as a function of M_0 for the same four maximum phase errors is shown in Fig. 2.10, which indicates that the best improvement of CNR using GCF can generally be achieved when M_0 is equal to one. Again, such a result suggests the inherent incoherence from a speckle-generating target should be taken into consideration to choose a proper M_0. For a given value of M_0, the improvement of CNR decreases as the maximum phase error increases. Furthermore, for M_0 equal to zero, the corresponding CNR after correction generally increases except for the case with a $\pi/2$ maximum phase error. This may be caused by the beam splitting effect with M_0=0 in Fig. 2.6(d). The results shown in Figs. 2.9 and 2.10 indicate that both CR and CNR may need to be considered when evaluating the contrast improvement.

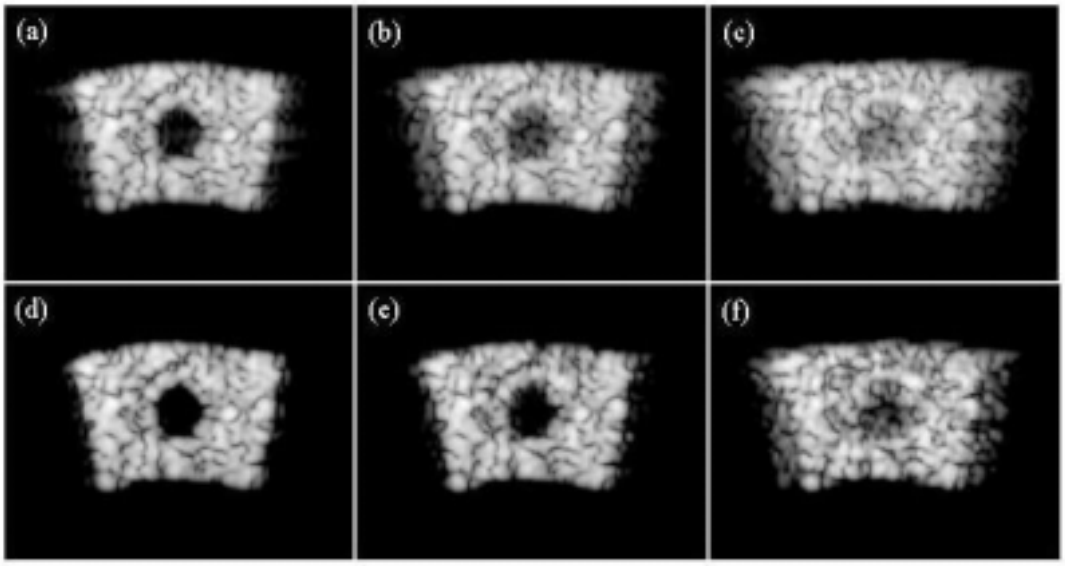

Fig. 2.11. Original and GCF-corrected images of a phantom with an anechoic cyst over a 50 dB dynamic range. The top row shows the uncorrected images; the bottom row shows the corrected images. (a), (d) No aberration. (b), (e) $\pi/4$ maximum phase error at the imaging frequency of 3.5 MHz. (c), (f) $\pi/2$ maximum phase error.

Figs. 2.11(a)–(c) and (d)–(f) show the uncorrected and GCF-corrected images with maximum phase errors of 0, $\pi/4$, and $\pi/2$, respectively. Based on Fig. 2.10, M_0=1 was used for GCF correction. It is obvious that the detection of the cyst is significantly improved, but the adaptive weighting technique is less effective for the case with a $\pi/2$ maximum phase error. The CR and CNR values for the images in Fig. 2.11 are listed in Table 2.1. Using GCF weighting, the corrected images exhibit contrast improvements of 22.35 dB, 15.74 dB, and 8.64 dB for maximum phase errors of 0, $\pi/4$, and $\pi/2$, respectively. A higher CNR is also obtained after adaptive GCF weighting. Note that the CR and CNR of the unaberrated case also increase after the GCF weighting. This is because the sidelobe level of an unaberrated beam is also

suppressed by the GCF weighting, as shown in Fig. 6(a).

Table 2.1. CR and CNR for the simulated images of a phantom with an anechoic cyst. 0 means no aberration. π/4 and π/2 represent maximum phase errors, respectively, at the imaging frequency of 3.5 MHz.

CR (dB)

	0	π/4	π/2
Uncorrected	32.32	23.07	13.54
GCF	54.67	38.81	22.18

CNR

	0	π/4	π/2
Uncorrected	6.84	4.55	2.94
GCF	10.34	6.33	3.47

2.3.3 Experimental Results

Three complete RF data sets with three different levels of distortion were used to test the efficacy of the proposed adaptive weighting method (all the raw data are available from http://bul.eecs.umich.edu). The data sets were the same as those used by O'Donnell and Flax [19]. The first data set was RF data acquired from a tissue-mimicking phantom without distortion. The other two data sets were acquired from the same phantom except that 1× and 2× distortion were introduced, corresponding to maximum phase errors of π and 2π, respectively, at the imaging frequency of 3.33 MHz. The distortion resulted from a room-temperature-vulcanizing (RTV) plate inserted between the array and the tissue-mimicking phantom. They were acquired using a 64-element, 3.33-MHz phased-array transducer with a 17.76-MHz sampling frequency. Dynamic receive focusing with an f/number of 2 was applied, and the transmit focus was at 60 mm. All images are displayed over a 50 dB dynamic range and are shown in a pre-scan conversion format (i.e., the vertical axis represents range and the horizontal axis is azimuth).

Fig. 2.12(a) is the image without distortion, and Figs. 2.12(b) and (c) show images of the phantom with 1× and 2× distortion, respectively. Figs. 2.12(d)–(f) show the corrected images of Figs. 2.12(a)–(c), respectively, using GCF weighting with M_0 set to 2. Note that all the images are normalized by the mean value of the homogeneous region located at the image center. These corrected images show that the image quality is noticeably improved. Table 2.2 lists the CR and CNR values for the images shown in Fig. 2.12. The two parameters are calculated using the

background and cyst region indicated by the black and white boxes shown in Fig. 2.12(a). Using GCF, the corrected images have contrast enhancements of 15.23 dB (no distortion), 11.11 dB (1×), and 7.05dB (2×). Higher CNR values were also obtained after adaptive weighting, and the corrected images with less distortion have both higher CR and higher CNR values.

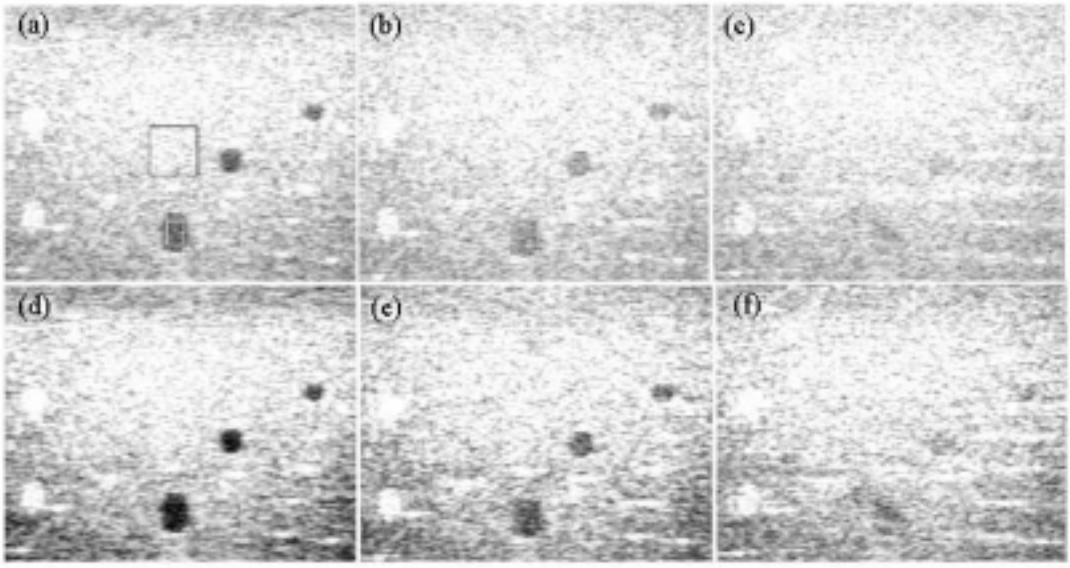

Fig. 2.12. Original and GCF-corrected images of a tissue-mimicking phantom over a 50 dB dynamic range. The top row shows the uncorrected images; the bottom row shows the corrected images. (a), (d) No distortion. (b), (e) 1× distortion. (c), (f) 2× distortion.

Table 2.2. CR and CNR for the images of a tissue-mimicking phantom.

CR (dB)

	No distortion	1× distortion	2× distortion
Uncorrected	25.44	16.86	11.04
GCF	40.67	27.97	18.09

CNR

	No distortion	1× distortion	2× distortion
Uncorrected	4.54	2.95	1.97
GCF	6.41	3.65	2.30

2.4 Discussion

2.4.1 Effect of the Cut-off Frequency M_0

The simulation results show that the cutoff frequency M_0 affects the performance of the GCF technique. Weighting by the coherence factor (i.e., GCF with M_0=0) is only suitable for point targets, but may make the beam-splitting effect more pronounced. Hence, a larger M_0 (i.e., $M_0 \neq 0$) should be used. In addition, for diffuse scatterers, M_0 should also be sufficiently large in order not to introduce image artifacts. On the other hand, the GCF technique becomes less effective when M_0 is too large. Based on the results shown in this paper, the proper value of M_0 for diffuse scatterers is 1–3.

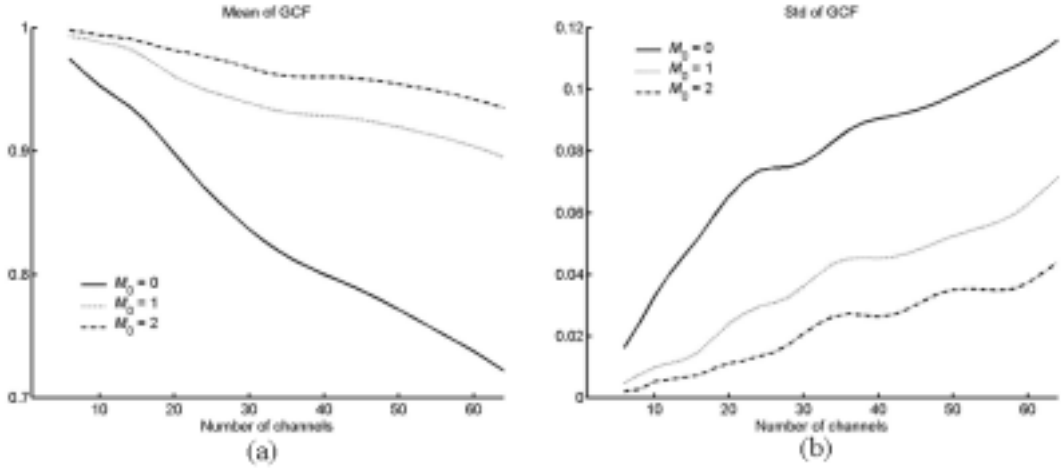

Fig. 2.13. Simulated GCF with ten different realizations of scatterer distributions. The solid line is for M_0=0, the dotted line is for M_0=1, and the dashed–dotted line is for M_0=2. (a) and (b) show the mean and standard deviation values, respectively.

Characteristics of the GCF are further explored by numerical simulations and compared to the original CF. It was previously demonstrated that the CF approaches to 2/3 for one-dimensional arrays when the number of channels is sufficiently large and when there is no focusing error [32], [34]–[35]. For GCF, the coherent sum depends on the specific M_0 used in the calculations, and an analytical solution is not likely to exist. Numerical simulations are therefore used to study the behavior with different cutoff frequencies. For each case, simulations were performed based on ten different realizations of the diffuse-scatterer distributions, and mean values and standard deviations were calculated (shown in Figs. 2.13(a) and (b), respectively). In Fig. 2.13 the solid lines correspond to M_0=0 (i.e., the original CF), the dotted lines are

for M_0=1, and the dashed–dotted lines are for M_0=2. The figure shows that as M_0 increases, the mean increases irrespective of the number of channels. On the other hand, the standard deviation decreases as M_0 increases. In other words, the CF (i.e., GCF with M_0=0) has a larger variation. Such a variation may cause image artifacts after the CF weighting. This agrees with the previous results.

2.4.2 Effect of SNR

The GCF is defined here without taking noise into consideration. In real imaging situations the SNR decreases as the imaging depth increases due to tissue attenuation, so the estimated GCF may be affected by noise. Assume that S_{low} and N_{low} are the spectral energies of the signals and noise within the prespecified low-frequency range, respectively, and that S_{total} and N_{total} are the total spectral energies of the signals and noise. The relationship between GCF without noise (i.e., an infinite SNR) and the estimated GCF with a finite SNR (denoted by GCF') can be obtained as follows:

$$\begin{aligned}\text{GCF}' &= \frac{S_{\text{low}} + N_{\text{low}}}{S_{\text{total}} + N_{\text{total}}} = \frac{N_{\text{total}}\left(\frac{S_{\text{low}}}{N_{\text{total}}} \cdot \frac{S_{\text{total}}}{S_{\text{total}}} + \frac{N_{\text{low}}}{N_{\text{total}}}\right)}{N_{\text{total}}(1+SNR)} = \frac{\left(\frac{S_{\text{low}}}{S_{\text{total}}} \cdot SNR + \frac{N_{\text{low}}}{N_{\text{total}}}\right)}{1+SNR} \\ &= \frac{\left(\text{GCF} \cdot SNR + \frac{N_{\text{low}}}{N_{\text{total}}}\right)}{1+SNR} = \frac{\left(\text{GCF} \cdot SNR + \frac{2M_0+1}{N}\right)}{1+SNR},\end{aligned} \tag{2.5}$$

where $SNR = \frac{S_{\text{total}}}{N_{\text{total}}}$, and N is the number of points used for the FFT. If the SNR is very low, the estimated GCF can be expressed as

$$\text{GCF}' \approx \frac{(2 \cdot M_0 + 1)}{N}. \tag{2.6}$$

For the experimental data used in this paper, M_0 was set to 2 and N was 64. From Eq. (2.6), the estimated GCF should be about 0.078 when the SNR is very low. This value is close to the experimental value of 0.082. On the other hand, the penetration depth can be defined as the depth where the SNR is equal to 1. In this case, the corresponding estimated GCF can be expressed as

$$\text{GCF}' = \frac{\left(\text{GCF} + \frac{2M_0+1}{N}\right)}{2} = \frac{\text{GCF} + 0.078}{2} \approx \frac{\text{GCF}}{2} \left(\text{e.g., } N = 64, M_0 = 2\right). \tag{2.7}$$

Eq. (2.7) shows that the estimated GCF at the penetration depth (defined by SNR=1) is half the ideal GCF. The above results also show that although the estimated GCF is dependent on the SNR, the real GCF that needs to be used for adaptive weighting can still be retrieved if the SNR can be estimated. In addition, GCF' can also be applied directly in order to reduce the effects of a low SNR.

2.4.3 Compared with the Correlation-Based Technique and PARCA2

Finally, performance of the proposed GCF technique with a displaced phase screen is evaluated compared with the correlation-based technique [18][19] and PARCA2 [29]. The simulation method was the same as that used by Ng et al. [22]. The displaced phase-screen profile was the same as the normalized phase-aberration profile shown in Fig. 2.2. A sector scan from –5° to 5° was performed. The maximum phase error was $\pi/2$ at the center frequency of 3.5 MHz. A point source was located at a depth of 80 mm, with the transducer being focused at the same depth; the simulation results are shown in Fig. 2.14. Figs. 2.14(a) and (c) show the simulation results of the normalized receive beam patterns in the presence of a phase screen at 0 mm from the transducer, and Figs. 2.14(b) and (d) show the receive beam patterns with the same phase screen at 40 mm. The lateral axis is azimuth. Since a point target was imaged, M_0 was chosen as 0 for GCF calculations.

Figs. 2.14(a) and (b) compare the GCF and correlation-based techniques. As expected, the latter technique performs very well for the near-field phase screen (Fig. 2.14(a)). The GCF-corrected beam pattern is improved, exhibiting a lower sidelobes and a narrower mainlobe. However, the GCF-corrected beam introduces large variations in sidelobe level. This can be avoided by using a larger M_0 (e.g., M_0=1) with less sidelobe reduction. Fig. 2.14(b) shows that the GCF technique performs well for a displaced phase screen, outperforming the correlation-based technique for the displaced phase screen situation. Figs. 2.14(c) and (d) compare the GCF technique and PARCA2 (three iterations were used for PARCA2). Fig. 2.14(c) shows that for the near-field phase-screen situation, the PARCA2-corrected beam pattern has higher sidelobes than the GCF-weighted beam pattern but with less variations. Fig. 2.14(d) shows that the GCF technique also outperforms PARCA2 for the displaced phase-screen situation.

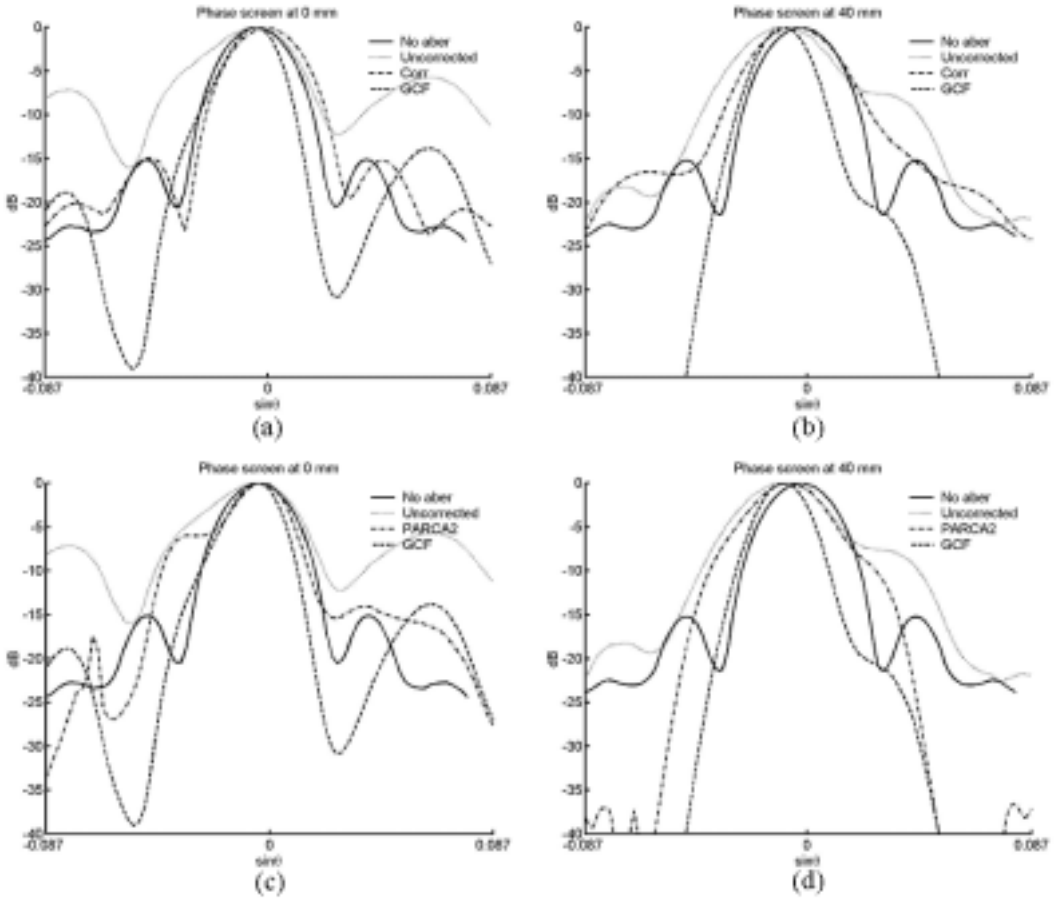

Fig. 2.14. Projected receive beam patterns for a point target with a displaced phase screen. (a), (c) Phase screen at 0 mm. (b), (d) Phase screen at 40 mm. Solid lines, no aberration; dotted lines, uncorrected; dashed lines, corrected by GCF weighting; dashed–dotted lines, corrected by the correlation-based technique in (a) and (b), and corrected by PARCA2 in (c) and (d).

The correlation-based technique using one-dimensional arrays has shown limited success due to inadequate spatial sampling of sound-velocity inhomogeneities in elevation. Two-dimensional arrays have been suggested for obtaining adequate performance in clinical situations [23], [24]. Unlike the correlation-based technique, however, the proposed GCF technique only attempt to improve beam quality regardless of the dimensionality of the array. Therefore, for real-time applications using one-dimensional arrays, the proposed GCF technique is more suitable than the correlation-based technique. Compared to PARCA2, the GCF technique has lower computational complexity and memory requirements, and no iterations are needed.

2.5 Concluding Remarks

This chapter proposes an adaptive weighting technique based on the GCF for reducing focusing errors in acoustic imaging, especially for the focusing error caused by sound-velocity inhomogeneities. The technique is independent of the source of the artifacts and can be implemented efficiently. Thus it can also be applied to reduce the focusing-delay accuracy, extend the transmit focal zone, or minimize the effects of sound-velocity inhomogeneities. Especially for sound-velocity inhomogeneities, the simulation and experimental results demonstrate that the proposed GCF technique corrects for both near-field and displaced-phase errors. Furthermore, it is shown that the SNR and the cutoff frequency M_0 influence the performance of the proposed GCF technique. The proposed GCF technique performs better than PARCA2, while its computational complexity and memory requirements are lower. In addition, no iteration is needed for the GCF technique. The proposed technique also performs better than the correlation-based technique when a displaced phase screen is present. Finally, the proposed GCF technique can be incorporated into current medical ultrasonic imaging systems with only modest modifications.

Chapter 3 Adaptive Receive Aperture Technique

Sidelobe contribution from off-axis targets degrades image quality in a coherent array imaging system. Focusing errors resulting from sound-velocity inhomogeneities in human tissue reduce the coherence of the received signals and elevate the sidelobe level. In this chapter, an adaptive receive aperture technique based on the coherent factor (CF) thresholding is proposed. The CF describes coherence of the received array signals, and can be used as an index of focusing quality. Specifically, in this chapter, the CF is used to distinguish the mainlobe signals from the sidelobes. This chapter demonstrates that thresholding of the CF allows the mainlobe signals to be distinguished from the sidelobe signals. Once distinguished, the receive aperture size at each imaging position can be optimally determined so that the mainlobe signals are enhanced and the sidelobe signals are suppressed. Thus, image quality degradation resulting from sound-velocity inhomogeneities can be reduced. Simulations and real ultrasound data are used to evaluate efficacy of the proposed technique. Effects of the signal-to-noise ratio and the transmit focal depth on the proposed technique are discussed. The proposed technique is also compared with the parallel adaptive receive compensation algorithm: the improvement in image quality obtained with the proposed technique rivals that of the latter technique.

3.1 Coherence Factor Thresholding

In this section, simulations are used to explore characteristics of the CF for signals coming from the mainbloe and the sidelobes. The acoustic field simulation program Field II was employed and modified to simulate the received signal at each array element [36]. The simulated phased array had 64 elements with a center frequency of 3.5 MHz and a half-wavelength pitch. A sector-scan from –30° to 30° was performed and Nyquist beam spacing was used. The transmit focal point was 30 mm from the transducer, and dynamic focusing with an f/number of 2 was applied on receive. Focusing errors due to sound-velocity inhomogeneities were also considered, using the normalized phase-aberration profile shown in Fig. 2.2. Only a near-field phase screen (i.e., the time-delay errors occur at the face of the transducer) was

simulated for all aberration cases. For all aberration cases, the aberration profile was applied on both transmit and receive. Note that all images shown below are all sector-scan images prior to scan conversion (i.e., the vertical axis represents range and the horizontal axis is azimuth.)

3.1.1 Point Targets

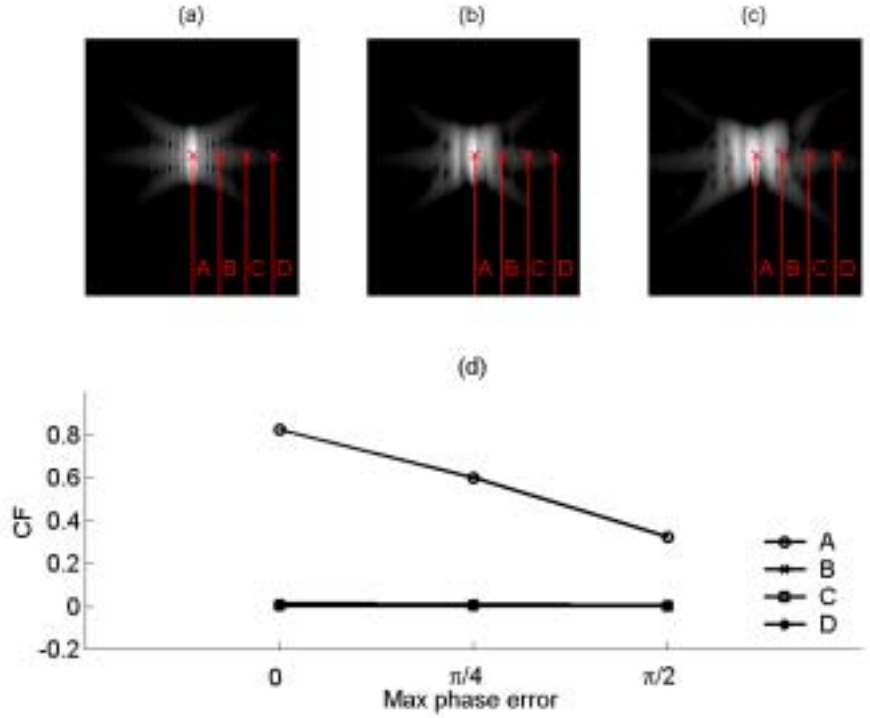

Fig. 3.1. Simulation results for a point target located at the transmit focal depth. (a)–(c) show the simulated point images over a 50 dB dynamic range, with maximum phase errors of 0 (i.e., no aberration), π/4, and π/2 at the imaging frequency of 3.5 MHz, respectively. The vertical axis represents range and the horizontal axis is azimuth. (d) shows the corresponding CFs at the imaging points indicated by the four × markers in (a)–(c) (A, B, C, and D).

First, images of a point target located at the transmit focal depth of 30 mm were simulated. The results are shown in Fig. 3.1. Figs. 3.1(a)–(c) show the simulated images with maximum phase errors of 0 (i.e., no aberration), π/4, and π/2 at the imaging frequency of 3.5 MHz, respectively. The images are displayed over a 50 dB dynamic range. It is evident that the beam quality degrades as the maximum phase error increases. Fig. 3.1(d) shows the CFs at four specific imaging locations. The curves A, B, C and D correspond to the four different image locations indicated by the four × markers in Figs. 3.1(a)–(c). With a larger maximum phase error, the CF decreases when the imaging position is located at the mainlobe (i.e., A). Note that the CFs of the imaging points located at the sidelobes (i.e., B, C, and D) are hardly distinguished from one another. They are much smaller than that at the mainlobe

although they remain relatively constant when the maximum phase error increases. The CFs of the imaging points at the sidelobes are typically smaller than 0.2. Fig. 3.1(d) suggests a way to differentiating between signals from the mainlobe and from the sidelobes by a threshold of CF.

3.1.2 Speckle-Generating Targets

To further investigate if characteristics of CF shown in Fig. 3.1(d) also exist for targets with diffuse scatterers, images with an anechoic cyst in a speckle-generating background were simulated. The cyst was centered at the transmit focal depth of 30 mm. The size of the speckle-generating background was 15 mm in the lateral direction and 10 mm in the axial direction. The anechoic object had a diameter of 5 mm. Positions of the scatterers were uniformly distributed, and the scattering amplitudes were Gaussian distributed. Other simulation settings were the same as those in the previous point target simulations.

Figs. 3.2(a)–(c) are the simulated cyst images over a 50 dB dynamic range, with maximum phase errors of 0, $\pi/4$, and $\pi/2$ at the imaging frequency of 3.5 MHz, respectively. Figs. 3.2(b) and (c) show that the $\pi/4$ and $\pi/2$ maximum phase errors result in degradation in image quality, as evidenced by the “fill in” (i.e., unwanted sidelobe contribution) in the anechoic cyst region. Fig. 3.2(d) also shows the associated CFs at the imaging points indicated by the four $\times$ markers (A, B, C, and D) in Figs. 3.2(a)–(c), and has the same format as Fig. 3.1(d). Imaging point B and D are located in the anechoic region. Imaging point A is located in a bright spot in the speckle region whereas imaging point C is located in a dark spot. The CF of imaging point A in the speckle region is larger than those of the imaging points in the anechoic region (i.e., B and D) although it decreases as the maximum phase error increases. Such a result is similar to that in Fig. 3.1(d). Also, note that the CFs of the imaging points in the anechoic region are smaller than a certain value (e.g., 0.2). However, the CF of the imaging point C also in the speckle region is almost as low as those in the anechoic region because the incoherence of the speckle-generating target introduces the dark spots (e.g., point C) in the speckle region, and thus lowers the CF of the dark spots. Such variations of CF in the speckle region indicate that CF also suffers from speckle noise, as described in section (2.3.2) [33]. Fig. 3.2(d) suggests that given a threshold of CF, signals from the speckle region and from the anechoic cyst (i.e., sidelobes contribution) may be differentiated if the variation of the CF in the speckle region can be reduced.

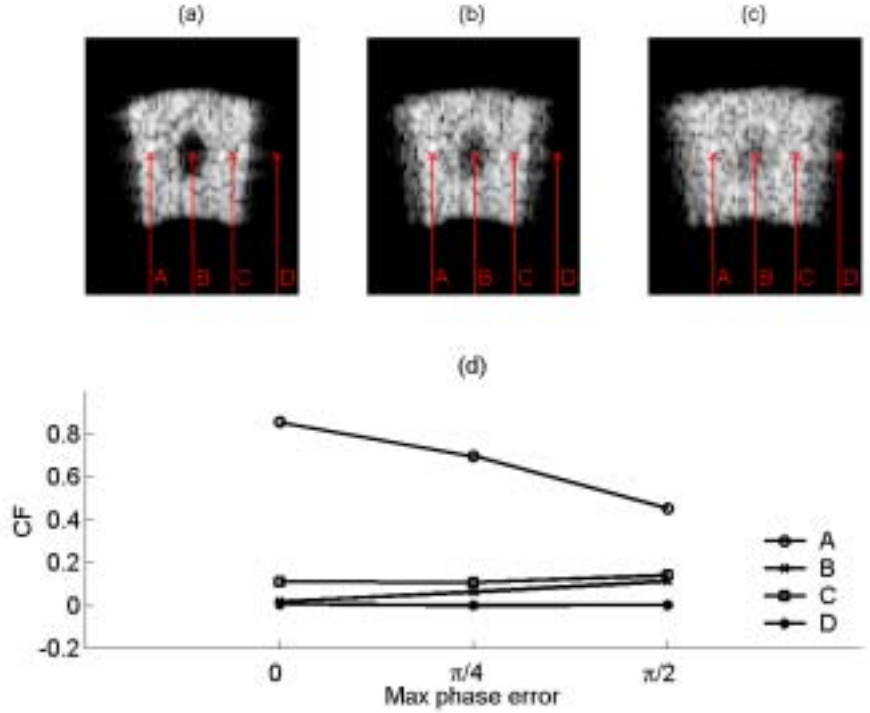

Fig. 3.2. Simulation results for a phantom with an anechoic cyst located at the transmit focal depth. (a)–(c) are the simulated cyst images over a 50 dB dynamic range, with maximum phase errors of 0, $\pi/4$, and $\pi/2$ at the imaging frequency of 3.5 MHz, respectively. The vertical axis represents range and the horizontal axis is azimuth. (d) shows the corresponding CFs at the imaging points indicated by the four × markers in (a)–(c) (A, B, C, and D).

Fig. 3.3(a) shows mean values of CF as a function of the maximum phase error. The solid line with squares is the mean values of the CF in the speckle region in Figs. 3.2(a)–(c), and the dashed line with circles shows the mean values of the CF in the anechoic cyst region in Figs. 3.2(a)–(c). The error bars represent $\pm$ one standard deviation relative to the mean value. It is shown that the mean values of the CF in the speckle region are differentiable from those in the anechoic cyst. However, the standard deviations of CF in the speckle region are quite large. Especially for the case with the $\pi/2$ maximum phase error, such a large standard deviation may lead to a significant error if a threshold of CF is used to distinguish the speckle signals from those from the anechoic cyst.

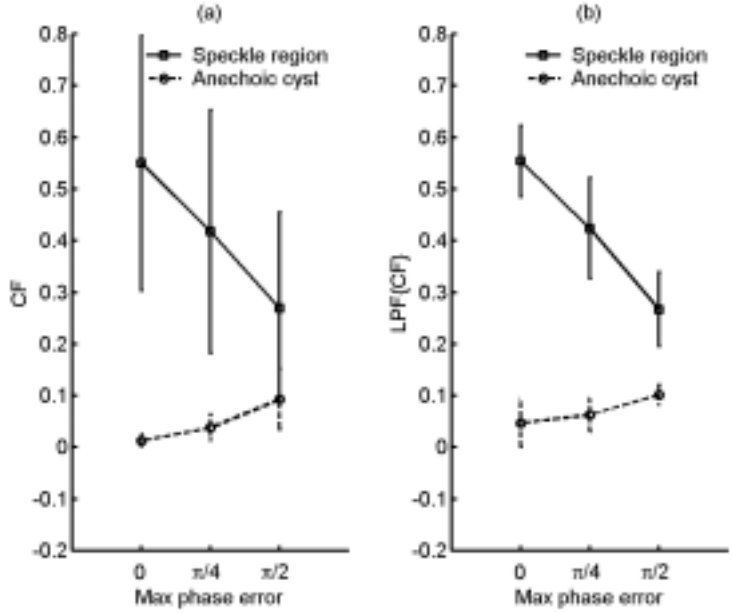

Fig. 3.3. Mean values of original CF and the corresponding low-pass filtered CF as a function of maximum phase error for the simulated cyst images. (a) Original CF. (b) Low-pass filtered CF. The error bars represent ± one standard deviation relative to the mean value.

From the results in Figs. 3.2(d) and 3(a), spatial low-pass filtering the CF may benefit such differentiation. Fig. 3.3(b) shows the corresponding results of the low-pass filtered CF (LPF{CF}) with the same format as that in Fig. 3.3(a). To smooth out the standard deviations of the CF and to retain the mean values of the CF simultaneously, a simple two-dimensional moving-average low-pass filter (LPF) is employed in this chapter [33]. It can be performed only by additions and no multiplications are required. The kernel size of the LPF is chosen as the number of the sample points corresponding to the –20 dB point spread function in azimuth times that in range (e.g., 5×17 for Nyquist beam spacing and 10-MHz sampling frequency in this case). Such a filter size renders the two curves in Fig. 3.3(b) separable even though the $\pi/2$ maximum phase error is introduced. Fig. 3.3(b) shows that given a threshold of CF allows signals from the speckle region and from the anechoic cyst (i.e., sidelobe contribution) to be differentiated through low-pass filtered CF, which is the basis of the proposed adaptive receive aperture technique, and will be referred to as “CF thresholding” in this dissertation.

3.2 Adaptive Receive Aperture Technique

In this section, an adaptive receive aperture technique is introduced. First, beam

sum as a function of active receive aperture size is investigated under different levels of phase aberrations. Fig. 3.4 shows the amplitude of beam sum as a function of the number of the center receive channels used for beam sum under different maximum phase errors. The curves A, B, C and D correspond to the four different image locations indicated by the A, B, C, and D four × markers in Figs. 3.2(a)–(c). Fig. 3.4(a) is the case without aberration. Fig. 3.4(b) is the case with a π/4 maximum phase error. Fig. 3.4(c) shows the aberration case with a π/2 maximum phase error. Note that the amplitude of beam sum is normalized by the maximum amplitude of beam sum in Fig. 3.4(a). It is shown that with the π/2 maximum phase error, the beam sum of a smaller number of receive channels (as indicated by the solid arrow) can be larger than that of a larger number of receive channels when the imaging position is in the bright spot of the speckle region (i.e., A). Also, whether phase aberrations exist or not, the maximum of the beam sum can be obtained with a smaller receive aperture size (as indicated by the dashed arrows) for the imaging point in the dark spot of the speckle region (i.e., C). Such signals of the dark spots should be enhanced to reduce speckle variance. In addition, with a sufficiently large receive aperture size (e.g., the number of the center receive channels is larger than one half of the total receive channels, 32), the beam sum corresponding to the imaging points in the anechoic region (i.e., B and D) is small relative to that in the speckle region.

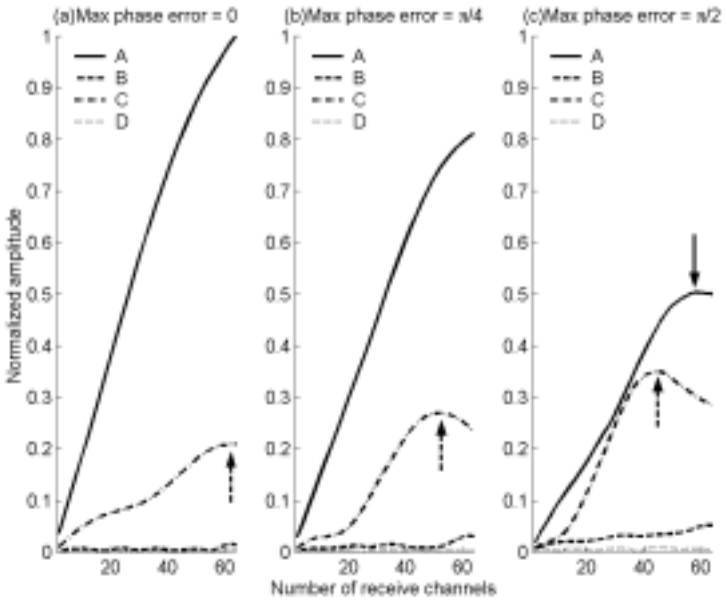

Fig. 3.4. Normalized amplitude of beam sum as a function of the number of the center receive channels used for beam sum under different maximum phase errors. (a) is the case without aberration. (b) is the case with a π/4 maximum phase error. (c) shows the case with a π/2 maximum phase error. The curves A, B, C and D correspond to the four different image locations indicated by the A, B, C, and D in Figs. 3(a)–(c).

Fig. 3.4 shows that when phase aberrations are present or when the imaging point is located in the dark spots, beam formation with a smaller receive aperture can result in a larger beam sum for imaging points in the speckle region. On the other hand, section (3.1) demonstrates CF thresholding can distinguish speckle signals from the incoherent noise (i.e., sidelobe contribution). Based on the two properties, an adaptive receive aperture technique can be developed. Once signals from the sidelobes (or the anechoic region) and the mainlobe (or the speckle region) are identified, the optimum number of receive channels at each imaging point, $N_{\text{optimal}}(t)$, can be adaptively determined as follows,

$$\begin{cases} N_{\text{optimal}}(t) = \{N \mid \max(S(N,t)), N = N_{\min}, N_{\min}+1, ..., N_{\max}\}, \text{if LPF}\{\text{CF}(t)\} \geq \text{CF}_{\text{threshold}} \\ N_{\text{optimal}}(t) = \{N \mid \min(S(N,t)), N = N_{\min}, N_{\min}+1, ..., N_{\max}\}, \text{if LPF}\{\text{CF}(t)\} < \text{CF}_{\text{threshold}} \end{cases},$$

(3.1)

where $N_{\max}$ is the number of total active channels on receive, $N_{\min}$ is the lower bound of N_{optimal} that is used to avoid degradation of spatial resolution and to preserve signal-to-noise ratio, and N is the number of center receive channels used for beam sum $S(N,t)$, ranging from $N_{\min}$ to $N_{\max}$. $\text{CF}_{\text{threshold}}$ is used to determine where the imaging point is. When low-passed CF of the imaging point (LPF{CF(t)}) is smaller than $\text{CF}_{\text{threshold}}$, the imaging point is considered to be at the sidelobes or in the anechoic region; thus $N_{\text{optimal}}(t)$ should minimize the beam sum $S(N,t)$ so that the signals coming from the sidelobes or the anechoic region can be suppressed. Otherwise, $N_{\text{optimal}}(t)$ should maximize the beam sum $S(N,t)$ to enhance the signals from the mainlobe or the speckle region. Therefore, the image quality degradation resulting from sound-velocity inhomogeneities can be reduced.

Note that if the mainlobe signal is misjudged as an incoherent noise, image artifacts (e.g., black holes) will be introduced. On the other hand, image artifacts are generally minor if an incoherent noise is determined as a mainlobe signal because the beam sum in this case is relatively small compared with that in the speckle region, as shown in Fig. 3.4. Hence, lower $\text{CF}_{\text{threshold}}$ and larger $N_{\min}$ are generally more preferable. A system block diagram for the proposed adaptive receive aperture technique is shown in Fig. 3.5. The echo signal is received and digitized by the A/D converter, and then the received RF data are demodulated down to baseband. After the baseband beamformer applies proper dynamic receive delays and phase rotations, the baseband data are sent to the delayed channel buffer. The CF is then estimated and low-pass filtered using the delayed baseband array data across the aperture at each

range (note that the CF should be calculated for all range points). Then, the optimal receive aperture size at each range point is determined according to Eq. (3.1). The corresponding beam sum of the optimal receive aperture size at each range point is then sent to the beam buffer for further signal processing, scan conversion, and display. The computational complexity is relatively low, and no iteration is needed. As illustrated in Fig. 3.5, the proposed technique can be incorporated into a baseband beamformer.

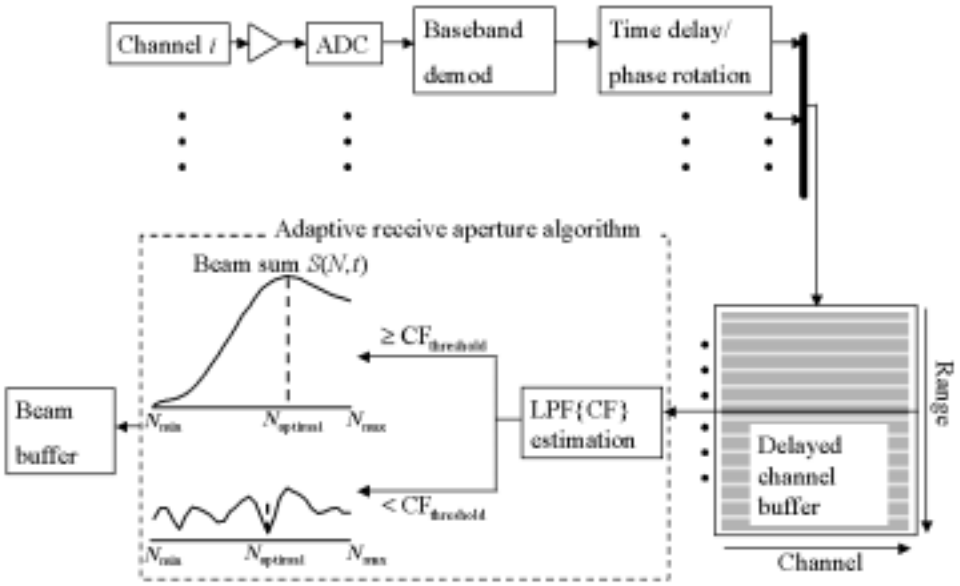

Fig. 3.5. System block diagram for the adaptive receive aperture technique.

3.3 Simulation and Experimental Results

In this section, simulated ultrasound data are used to explore the efficacy of the adaptive receive aperture technique in compensating for the focusing errors. In addition to simulated data, emulated images using real ultrasound data are also presented. Note that N_{max} is restricted by the receive f/number for dynamic receive focusing, and N_{min} is set to $N_{max}/2$ here.

3.3.1 Point Target Simulations

First, point-target simulations with sound-velocity inhomogeneities were used to evaluate the adaptive receive aperture technique. The same simulations as shown in

Fig. 3.1 were used here. Fig. 3.6 shows the projected radiation patterns for the point target under different aberration conditions with and without the adaptive receive aperture technique. Fig. 3.6(a) is the case for no aberration. Fig. 3.6(b) shows the aberrated case with a $\pi/4$ maximum phase error, and Fig. 3.6(c) is the case with a $\pi/2$ maximum phase error. $CF_{threshold}$ was set at 0.12 for all cases according to the results shown in Fig. 3.3. Fig. 3.6 shows that sidelobes of the point images are suppressed using the adaptive receive aperture technique. Fig. 3.6 shows that the far sidelobes are all suppressed by about 5 dB for each case after the adaptive receive aperture technique is applied. The suppression of the near sidelobe decreases as the maximum phase error increases. Note that the adaptive receive aperture technique also suppresses the sidelobe level even though no aberration is present. Finally, the proposed technique slightly increases the mainlobe width due to the fact that the CF map is low-pass filtered.

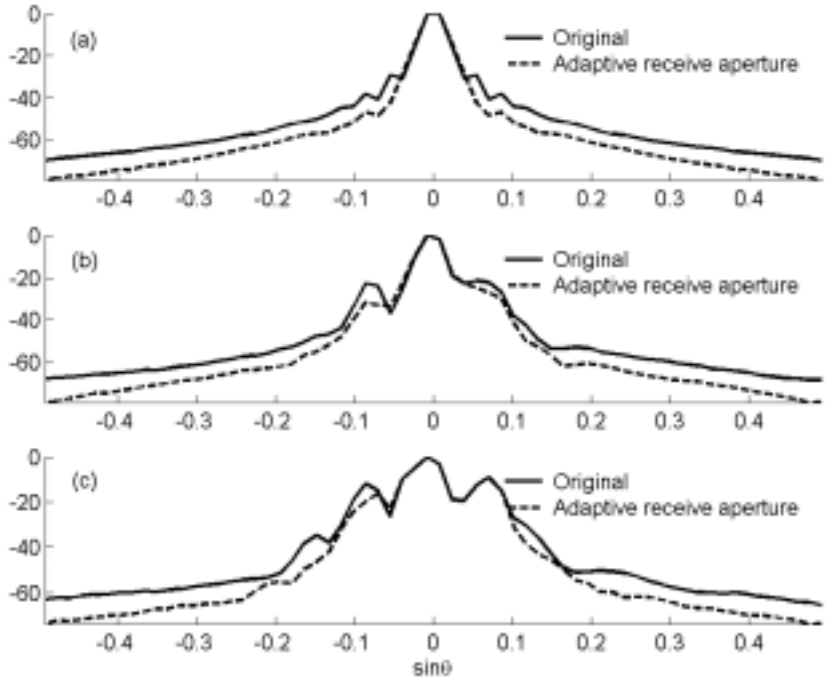

Fig. 3.6. Projected radiation patterns for a point target. (a) No aberration. (b) $\pi/4$ maximum phase error at the imaging frequency of 3.5 MHz. (c) $\pi/2$ maximum phase error. Solid lines, original radiation patterns; dashed lines, radiation patterns with the adaptive receive aperture technique being applied.

3.3.2 Anechoic Object Simulations

To further demonstrate the efficacy of the proposed technique for targets with diffuse scatterers and to evaluate potential improvement on contrast resolution, an anechoic cyst in a speckle-generating background was simulated. The same simulations as shown in Fig. 3.2 was used. Figs. 3.7(a)–(c) show the simulated images

with no distortion, π/4 maximum phase error, and π/2 maximum phase error, respectively. Figs. 3.7 (d)–(f) show the corresponding results of Figs. 3.7(a)–(c), respectively, using the adaptive receive aperture technique. These images are displayed over a 50 dB dynamic range. $CF_{threshold}$ used here was the same as that in point-target simulation (i.e., 0.12). It is shown that the cyst detection is significantly improved after the proposed technique being applied, but the proposed technique is less effective for the case with a π/2 maximum phase error.

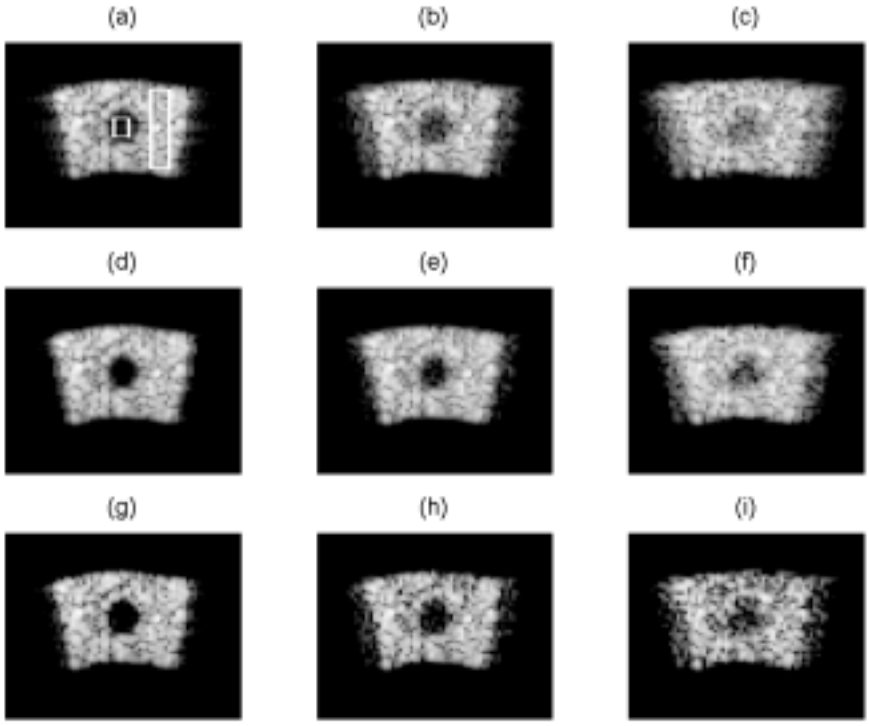

Fig. 3.7. Images of a phantom with an anechoic cyst over a 50 dB dynamic range. The vertical axis represents range and the horizontal axis is azimuth. The top row shows the original images; the middle row shows the images with the adaptive receive aperture technique; the bottom row shows the PARCA2-corrected images. (a), (d), and (g) No aberration. (b), (e), and (h) π/4 maximum phase error at the imaging frequency of 3.5 MHz. (c), (f), and (i) π/2 maximum phase error.

Standard deviation in the speckle background, and two indices related to contrast resolution are employed to evaluate the improvement in image quality: (i) the CR, and (ii) the CNR. Note that the right- and left-hand white boxes shown in Fig. 3.7(a) indicate the background and cyst regions, respectively. Figs. 3.8(a), (b), and (c) shows estimated standard deviation in the speckle background, CR and CNR of the cyst images, respectively. The solid lines with squares are the original values, and the solid lines with circles are the corrected values with the adaptive receive aperture technique. It is shown that the speckle variance in the speckle background is reduced for all cases

after applying the adaptive receive aperture technique. CR and CNR are also significantly improved using the adaptive receive aperture technique.

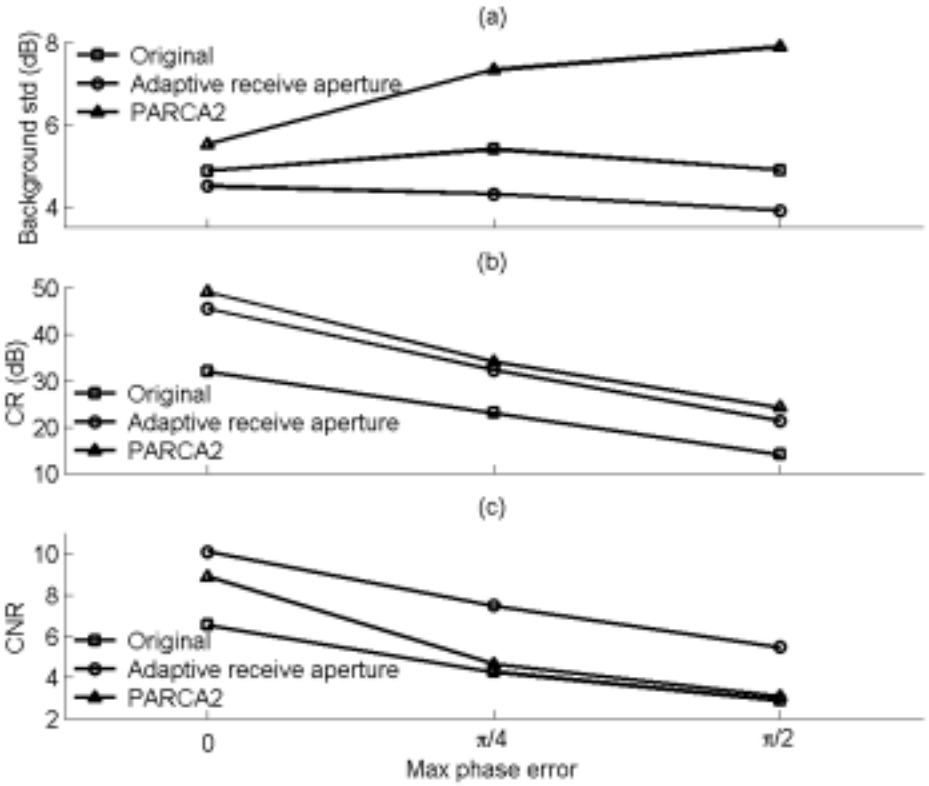

Fig. 3.8. Standard deviation in the speckle background, CR and CNR of the simulated images with an anechoic cyst for different maximum phase errors. 0 means no aberration. π/4 and π/2 represent maximum phase errors at the imaging frequency of 3.5 MHz. (a) Standard deviation in the speckle background. (b) CR. (c) CNR. Solid lines with squares, original; solid lines with circles, corrected with adaptive receive aperture technique; solid lines with triangles, corrected with PARCA2.

3.3.3 Experimental Results

The three complete RF data sets with three different levels of distortion used in section (2.3.3) were also employed to test the efficacy of the proposed adaptive receive aperture technique. Dynamic receive focusing with an f/number of 2 was applied. Note that dynamic focusing with an f/number of 2 was also applied on the transmit in order to test the proposed technique in the absence of influence from the transmit focal depth.

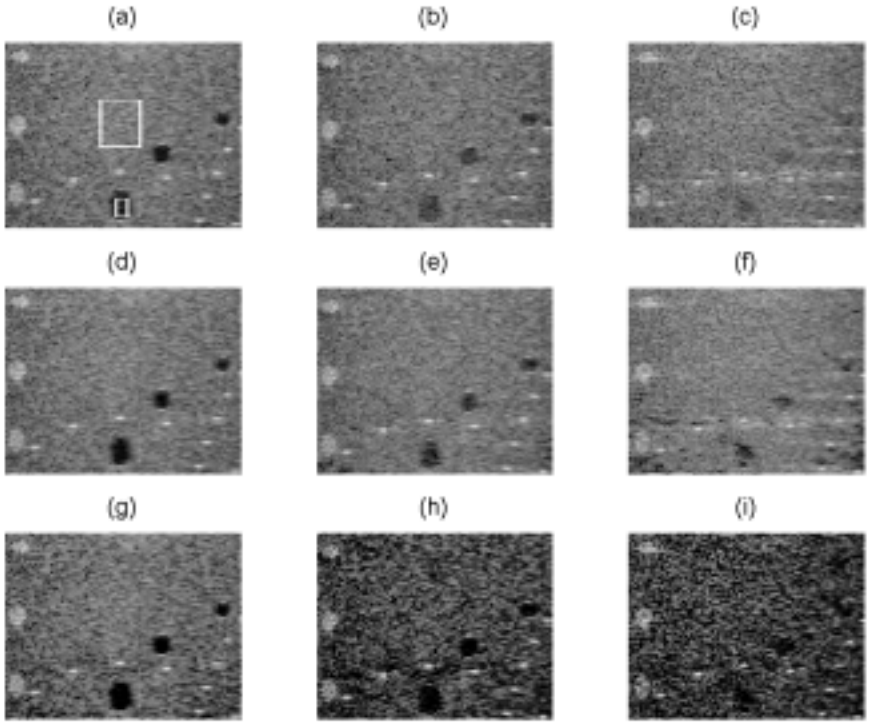

Fig. 3.9. Images of a tissue-mimicking phantom over a 60 dB dynamic range. The vertical axis represents range and the horizontal axis is azimuth. The top row shows the original images; the middle row shows the images with the adaptive receive aperture technique; the bottom row shows the PARCA2-corrected images. (a), (d), and (g) No distortion. (b), (e), and (h) 1× distortion. (c), (f), and (i) 2× distortion.

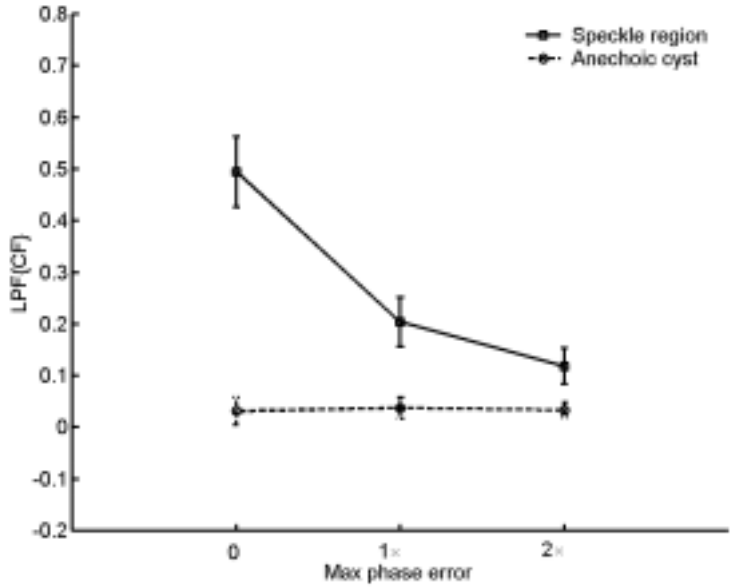

Fig. 3.10. Mean values of low-pass filtered CF as a function of maximum phase error for the experimental data. The error bars represent ± one standard deviation relative to the mean value.

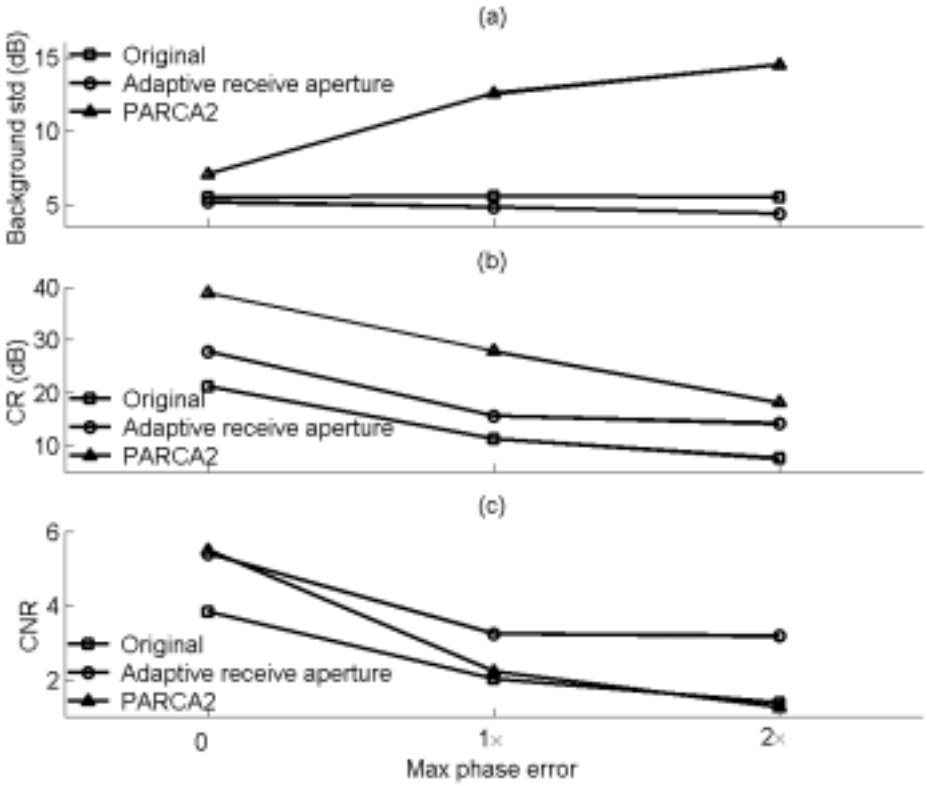

Fig. 3.11. Standard deviation in the speckle background, CR and CNR of the images of a tissue-mimicking phantom for different maximum phase errors. 0× means no aberration. 1× and 2× represent π and 2π maximum phase errors, respectively, at the imaging frequency of 3.33 MHz. (a) Standard deviation in the speckle background. (b) CR. (c) CNR. Solid lines with squares, original; solid lines with circles, corrected with adaptive receive aperture technique; solid lines with triangles, corrected with PARCA2

Fig. 3.9(a) is the image without distortion, and Figs. 3.9(b) and (c) show images of the phantom with 1× and 2× distortion, respectively. Fig. 3.10 shows mean values of the low-pass filtered CF as a function of maximum phase error for the experimental data, with the same format as that of Fig. 3.3. In this case, the kernel size of the LPF is 5×23 for Nyquist beam spacing and 17.76-MHz sampling frequency. The upper and lower white boxes shown in Fig. 3.9(a) indicate the speckle region and the anechoic cyst region used for CF estimation in Fig. 3.10. From Fig. 3.10, experimental signals from the speckle region and from the anechoic cyst also can be differentiated by CF thresholding. In this case, $CF_{threshold}$ is chosen as 0.05 for experimental data. Figs. 3.9(d)–(f) show the corrected images of Figs. 3.9(a)–(c), respectively, using the adaptive receive aperture technique. All images are displayed over a 60 dB dynamic range. The vertical axis (i.e., range) ranges from 28.61 mm to 96.18 mm, and the horizontal axis (i.e., azimuth) ranges from –40 degree to +40 degree. It is shows that the proposed technique noticeably improves the image quality for all cases. Figs. 3.11(a), (b) and (c) shows the estimated standard deviation in the speckle background,

CR and CNR values for the images shown in Fig. 3.9, respectively. The solid lines with squares are the original values, and the solid lines with circles are the corrected values with the adaptive receive aperture technique. Again, the adaptive receive aperture technique reduces the speckle variance in the speckle background for all cases. Higher CR and CNR values are also achieved, and the images with less distortion have both higher CR and higher CNR values after the proposed technique is applied.

3.4 Discussion

3.4.1 Effect of SNR

The CF in chapter 1 is defined without taking noise into consideration. The estimated CF is affected by noise, which in turn affects accuracy of CF thresholding in the adaptive receive aperture technique. This is also demonstrated by the different of CF thresholds used for simulations and experiments. The relationship between CF without noise (i.e., an infinite SNR) and the estimated CF with a finite SNR (denoted by CF') can be expressed as follows (derived from Eq. (2.5) with $M_0 = 0$ for GCF):

$$\mathrm{CF}' = \frac{\mathrm{CF} \cdot \mathrm{SNR} + \frac{1}{N}}{1 + \mathrm{SNR}}. \tag{3.3}$$

Eq. (3.3) shows that although the CF' is dependent on the SNR, the real CF that needs to be used for CF thresholding can still be retrieved once the SNR is estimated.

3.4.2 Effect of the Transmit Focal Depth

The above experiment test the adaptive receive technique with dynamic transmit focusing. To investigate effects of the transmit focal depth on the proposed technique, images of a phantom with an anechoic cyst located in the out-of-focus region were simulated under different levels of phase aberrations. Simulation settings were the same as those used in Fig 3.2 except that the transmit focal point was 60 mm from the transducer while the cyst used was still centered at 30 mm. Fig. 3.12 shows mean values of the low-pass filtered CF as a function of maximum phase error for the phantom with an anechoic cyst located in the out-of-focus region with the same format as that of Fig. 3.3. Results in Fig. 3.12 are different from those in Fig. 3.3. That is, the performance of CF thresholding in the proposed technique depends on the

transmit focal depth. Nonetheless, CF thresholding is still feasible.

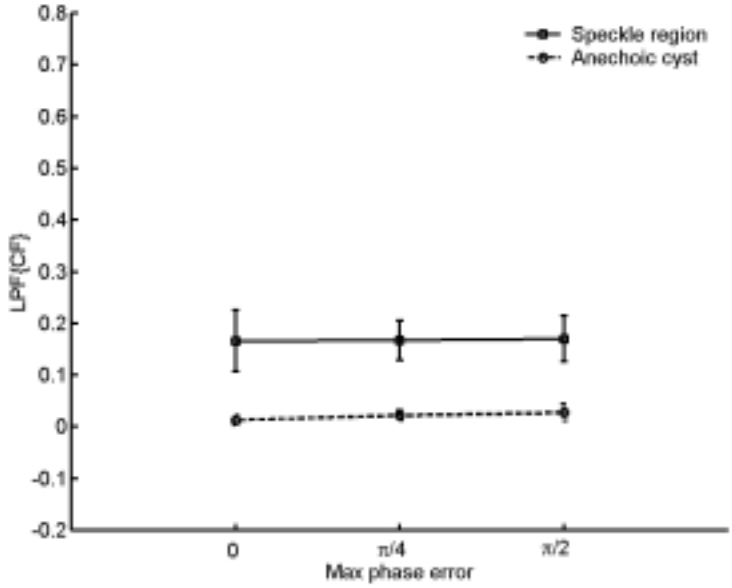

Fig. 3.12. Mean values of low-pass filtered CF as a function of maximum phase error for a phantom with an anechoic cyst located in the out-of-focus region. The error bars represent ± one standard deviation relative to the mean value.

3.4.3 Compared with PARCA2

Performance of the adaptive receive aperture technique on contrast improvement were also evaluated and compared with PARCA2 [29]. The same simulations as shown in Fig. 3.7 and the same experimental data as shown in Fig. 3.9 were used. Three iterations were used for PARCA2. Figs. 3.7 (g)–(i) show the PARCA2-corrected results of the simulated images shown in Figs. 3.7(a)–(c), respectively. Figs. 3.7 (g)–(i) show that detection of the cyst is improved using PARCA2. However, the PARCA2-corrected image shown in Fig. 3.7(i) exhibits increased speckle variance. The standard deviation in the speckle background, CR and CNR values of these PARCA2-corrected images are also calculated and shown in Figs. 3.8(a), (b), and (c), respectively (the solid lines with triangles). From Fig. 3.8, all the CNR's of the corrected images with the adaptive receive aperture technique are higher than those with PARCA2 although the CR's of PARCA2-corrected images are higher. In addition, with PARCA2, the standard deviation in the background region is larger than that without correction, and increases as the maximum phase error increases. Such large standard deviation introduces the image artifacts in Fig. 3.7(i). In addition to simulations, experimental data were also used. Figs. 3.9(g)–(i) show the PARCA2-corrected images of Figs. 3.9(a)–(c), respectively. The corresponding standard deviation in the speckle background, CR and CNR values are shown in Figs.

3.11(a), (b), and (c), respectively (the solid lines with triangles).Again, PARCA2 increases speckle variance as shown in Figs. 3.9(b) and (c). With PARCA2, the standard deviation in the background region is significantly larger than that without correction as the maximum phase error increases. Hence, PARCA2 deteriorates the CNR of the corrected image with 2× distortion as shown in Fig. 3.11(c). Note that the standard deviation in the speckle background is reduced for all cases with the proposed adaptive receive aperture technique. The proposed technique generally can obtain higher CNR than that with PARCA2. In addition, compared to PARCA2, the adaptive receive aperture technique has lower computational complexity and memory requirements, and no iterations are needed.

3.5 Concluding Remarks

This chapter proposes an adaptive receive aperture technique based on the CF thresholding to reduce focusing errors caused by sound-velocity inhomogeneities. Note that this technique is independent of the source of the artifacts and thus can be used to reduce other types of focusing errors. The simulations and experimental results demonstrate the effectiveness of the proposed adaptive receive aperture technique: the elevated sidelobe level was effectively suppressed and contrast resolution was noticeably improved. The speckle variance was also reduced by the proposed technique. Also note that, the proposed technique slightly increases the mainlobe width due to the fact that the CF map is low-pass filtered to reduce the CF variations. The SNR and the transmit focal depth affect the performance of the proposed technique. Performance of the adaptive receive aperture technique can be further enhanced if $CF_{threshold}$ for CF thresholding can be optimized for different levels of phase aberrations. Typically, an alternative mapping of CF may be used to make better differentiation between mainlobe and sidelobe signals. The CF thresholding can also be generalized to GCF thresholding. Nonetheless, CF is used in the adaptive receive aperture technique due to the implementation efficiency. Furthermore, the proposed technique performs better than PARCA2, while its computational complexity and memory requirements are lower and no iteration is needed for the proposed technique. The proposed technique can be incorporated into current medical ultrasonic imaging systems with modest modifications.

Chapter 4 Applications in Parallel Receive Beam Formation

4.1 Introduction

In conventional ultrasonic imaging systems the receive beams are formed sequentially, with one receive beam along the transmit direction being formed after one transmit burst. Therefore, the sound velocity in the tissue fundamentally limits the data acquisition rate of such systems. A higher data acquisition rate makes it is possible to acquire more images (within a given time interval) that can be compounded to reduce speckle noise, or to reduce the average radiation exposure to the patient while maintaining the same display frame rate [37]. Other potential applications requiring high frame rates include cardiac imaging, color flow imaging, and real-time 3D imaging. The data acquisition time particularly limits the frame rate in real-time 3D imaging [38], [39].

To obtain a higher data acquisition rate, several techniques for forming multiple receive beams have been proposed [6], [31], [37], [40]–[41]. These techniques simultaneously produce multiple receive beams along different directions so that the data acquisition rate is increased by a factor equal to the number of reconstructed receive beams per transmit event. Each receive beam has its own reception time delays, and the respective time delays are applied to the same channel data prior to individual beam summation. The pulse-echo beam pattern for each beam produced in this manner is the product of the transmit beam pattern and the corresponding receive beam pattern. Hence, only receive beams close to the center of the transmit beam can be effectively synthesized [37].

Reconstructing multiple receive beams requires parallel processing, which increases the system complexity. Conceptually, a duplicate beam former is needed for each simultaneously received beam. Practically, several methods have been proposed to reduce the system complexity associated with parallel processing. Shattuck et al. used the delay similarity on each channel between adjacent receive beams to propose a parallel processing approach for a phased array sector scanner, named “Explososcan” [37]. In Explososcan, small tapped delay lines added at each receive

channel after the main delay system replaced a completely independent beam former for each additional receive beam. In their study, four simultaneous receive beams were formed for each transmit beam. The transmit beam needs to be sufficiently broad such that all the receive beams acquire data from all directions with sufficient insonification. A time multiplexing scheme has also been proposed for the formation of parallel receive beams [6]. Using two beams as an example, the sampled receive data are time multiplexed, in which the odd-number samples are used to form one beam and the even-number samples are used to form the other beam. Formation of the two receive beams is switched in time. The formation of three or four parallel beams can be implemented in a similar fashion. With time multiplexing, the hardware complexity is reduced but the reduced clock rate produces a lower system bandwidth that may affect the axial resolution.

Alternatively, the parallel processing of received beams can be greatly simplified by ignoring the small time delay difference for neighboring beams on a given channel. Using the parabolic approximation, the time delay for a given array element is the sum of a range focusing term and a steering term. When the range focusing term is ignored, the formation of parallel beams can be approximated by Fourier transforming the baseband aperture data (i.e., the received channel data along the array direction). Based on this property, O'Donnell developed an efficient technique for forming parallel receive beams in phased array imaging [29], [31]. Two receive beams were formed with only a slight increase in hardware complexity. However, ignoring the focusing delay difference among different receive beams degrades the quality of the receive beams.

In this chapter, the GCF weighting technique proposed in chapter 2 is extended to reduce the sidelobes of the FT-derived parallel receive beams. The GCF is derived from the spatial spectrum of the received aperture data after the receive delays have been applied. The spatial spectrum of the baseband aperture data is also used to approximate receive beams in FT-based parallel reconstruction. Hence, the GCF weighting technique can be directly combined with the FT-based technique for forming parallel receive beams with only a slight increase in system complexity. Real ultrasound data are used to demonstrate the efficacy of the proposed technique on both wire targets and speckle-generating objects. The effects on contrast resolution and background noise level are explored. The extension of the proposed GCF technique to 3D ultrasound imaging is also discussed.

4.2 FT-Based Parallel Reconstruction

The channel data are defined as the data received by each array channel after the focusing delays of a particular receive direction are applied prior to beam summation. At a particular range, the data received by each channel i across the array is also called the aperture data, and can be denoted as $S(i)$. The time index is fixed at a particular range and thus is omitted in the above notation. Parallel receive beams can be simultaneously reconstructed using the FT of the baseband aperture data. The discrete Fourier spectrum across the array can be viewed as the approximation of multiple parallel receive beams centered at a prespecified direction (it is typically the transmit direction) and equally spaced by

$$\Delta \sin\theta = \lambda/(Nd), \tag{4.1}$$

where θ is the steering angle in a sector scan, d is the pitch of the array, λ is the wavelength, and N is the number of points in the discrete spectrum [29], [31]. Note that N determines the spacing of the reconstructed beams.

The N-point discrete Fourier spectrum of the aperture data can be expressed as

$$p(k) = \sum_{i=0}^{N-1} S(i) e^{-j2\pi(id)\frac{k}{Nd}} = \sum_{i=0}^{N-1} S(i) e^{-j2\pi\frac{ik}{N}}, \tag{4.2}$$

where $k = -N/2$ to $N/2-1$ is the spatial frequency index, which can also be used as the receive beam index. If the length of $S(i)$ is less than N, $S(i)$ is zero padded to length N. The discrete Fourier transform can be efficiently computed using the fast FT (FFT). Note that the negative and positive parts of k represent equally spaced beam directions on each side of the center of all receive beams (i.e., k=0). In other words, the DC component (i.e., $p(0)$) represents the received signal from the prespecified primary receive direction, and the high-frequency components correspond to the approximated receive beams from other angles.

In practice, only the receive beams near the center of the transmit beam can be effectively synthesized. Hence, the transmit beam should be broadened for the formation of parallel receive beams, and the transmit beam spacing is equal to the one-way Nyquist beam spacing $\lambda/N_t d$, where N_t is the number of transmit channels. Note that the transmit beam width can be adjusted by varying N_t. The geometry of n parallel receive beams using the FT approximation is illustrated in Fig. 4.1 with n = 3 (i.e., three beams). In this case, three beams are received within the transmit beam.

The thick solid arrow represents the center receive beam direction and the two dotted arrows are the additional parallel receive beams. The region within the two dashed lines in Fig. 4.1 is defined as the effective region for the *i*-th transmit beam (Tx_i). The *n* parallel receive beams are evenly spaced by $\lambda/(nN_td)$. Comparing this spacing with that defined in Eq. (4.1), the number of points in the discrete spectrum is equal to *n* times the number of transmit channels, i.e.,

$$N = nN_t . \tag{4.3}$$

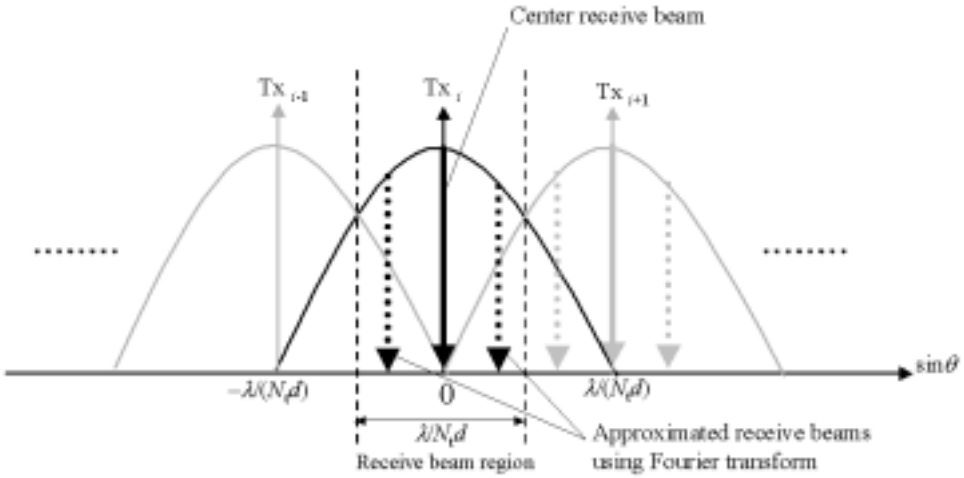

Fig. 4.1. Illustration of the geometry of three parallel receive beams. The thick solid arrow indicates the center receive beam direction, and the two dotted arrows are the parallel receive beams with approximated delays.

In addition, the spacing of the *n* parallel receive beams needs to satisfy the two-way Nyquist criterion, with the two-way effective aperture size being $(N_t+N_r)d$. In other words, N_t and N_r must be chosen such that $\lambda/(nN_td) \le \lambda/[(N_t+N_r)d]$ [42]. Thus, the number of transmit channels used in FT-based parallel reconstruction can be expressed as

$$N_t = \left\lceil \frac{N_r}{n-1} \right\rceil, \tag{4.4}$$

where $\lceil \cdot \rceil$ is the ceiling function (i.e., the smallest integer that is larger than the value of the input parameter). Given the number of receive channels and the number of parallel receive beams for each transmit event, the number of transmit channels is first calculated using Eq. (4.4). Then, the number of points used in the FFT can be determined based on the receive beam spacing and Eqs. (4.3) and (4.4) to satisfy the two-way Nyquist beam sampling criterion. Although the FT-based technique for forming parallel receive beams can efficiently reconstruct parallel receive beams,

focusing errors are introduced since the focusing delay differences are ignored. Such focusing errors as well as the need for a wider transmit beam limit the performance of the FT-based technique for forming parallel receive beams, and need to be corrected.

4.3 The Adaptive Weighting Technique

In this section, the GCF weighting technique proposed for phase aberration correction in chapter 2 is extended and combined with the FT-based technique for forming parallel receive beams. The weighting factor (i.e., the GCF) is derived from the spectrum of the aperture data after appropriate receive delays have been applied prior to beam summation and after baseband demodulation. The GCF is an index of the focusing quality, where a high GCF corresponds to good focusing quality and thus the image intensity is maintained. A low GCF, on the other hand, should be used to reduce the image intensity since significant focusing errors are present. Ignoring the range focusing delay differences in FT-based parallel reconstruction makes the focusing imperfect – GCF adaptive weighting can be employed to reduce such imperfection and to further lower the sidelobes of the FT-derived parallel receive beams. In addition, since the spatial spectrum of the aperture data used to derive the GCF is readily available for FT-based formation of parallel receive beams, the GCF weighting technique can be directly combined with FT-based parallel reconstruction with only a small increase in system complexity.

For the formation of parallel receive beams, the GCF is defined as the ratio of the energy received from angles near the reconstructed receive beam direction to the total energy from all directions. Based on the relationship between parallel receive beams and the Fourier spectrum over the aperture data, as described in section (4.2), the GCF can also be viewed as the ratio of the spectral energy within a prespecified frequency range centered at the spatial frequency representing the reconstructed receive beam direction to the total energy. Hence, for FT-based parallel reconstruction, the GCF for one reconstructed receive beam l at a given range can be expressed as

$$\mathrm{GCF}_l = \frac{\sum_{k=-M_0+l}^{M_0+l} \left|p(k)\right|^2}{\sum_{k=N/2}^{N/2-1} \left|p(k)\right|^2}, \tag{4.5}$$

where M_0 is a cutoff frequency specifying the frequency range in the spatial frequency

index (i.e., from $-M_0$ to M_0). For three receive beams, the reconstructed receive beam index l ranges from –1 to 1: $l = 0$ represents the center receive beam, and $l = -1$ and 1 indicate respectively the left and right approximated receive beams as indicated by the two dotted arrows in Fig. 4.1. The procedure for calculating the GCF for three beams is illustrated in Fig. 4.2. Note that while imaging a speckle-generating target, the cutoff frequency M_0 cannot be restricted to zero since it needs to be large enough to include the inherent incoherence of such a target.

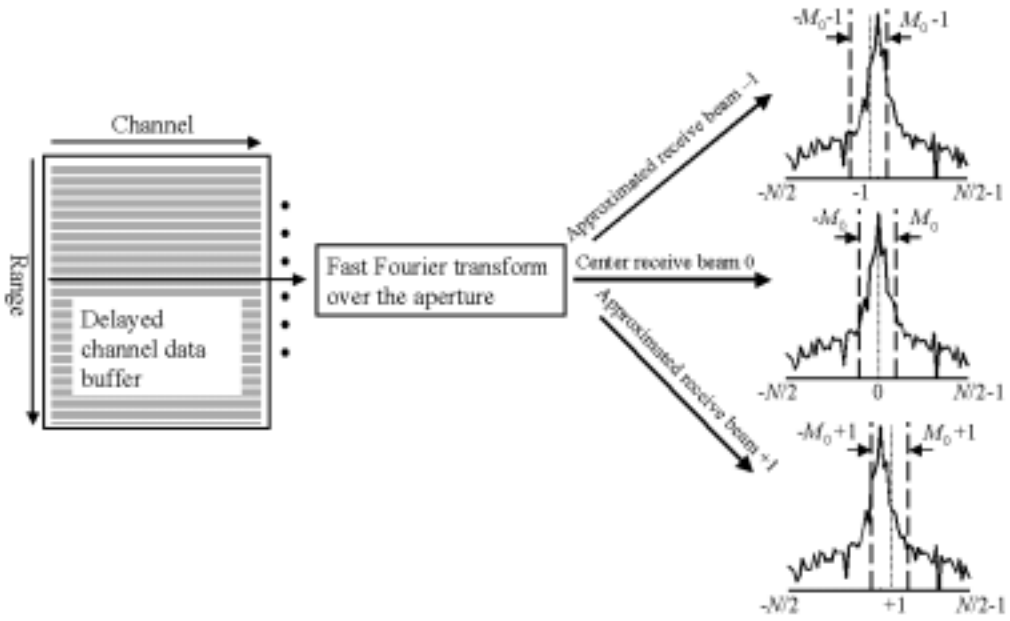

Fig. 4.2. Schematic diagram showing how the GCF for three beams is calculated.

As described above, the image quality of FT-based parallel reconstruction can be improved via GCF weighting. The GCF-weighted signal $x_{l\text{-weighted}}$ of x_l for the receive beam l at a given range can be expressed as

$$x_{l\text{-weighted}} = \mathrm{GCF}_l \cdot x_l \,. \tag{4.6}$$

Note that for each receive beam, the weighting needs to be calculated and applied at each imaging depth. Fig. 4.3 shows the system block diagram of the GCF technique for three beams. The echo signal for one transmit event is received and digitized by an analog-to-digital converter, and then the received RF data are demodulated down to baseband. The baseband beam former applies the correct

dynamic receive delays and phase rotations along the center receive direction (as indicated by the solid arrow in Fig. 4.1) before the data are sent to the channel buffer. The parallel receive beams and their corresponding GCFs are then estimated using the FFT of the delayed baseband array data (note that the GCFs need to be calculated at all range points). The spectral components at frequency indices of –1, 0, and 1 (i.e., the three beams illustrated in Fig. 4.1) are then weighted by the corresponding GCFs based on Eq. (4.6) on a point-by-point basis. The weighted data are then sent to the beam buffer for further signal processing, scan conversion, and display. Note that the reconstructed receive beams and their corresponding GCFs can be efficiently computed via the FFT at the same time. As illustrated in Fig. 4.3, the proposed GCF technique can be easily incorporated into the FT-based technique for forming parallel receive beams.

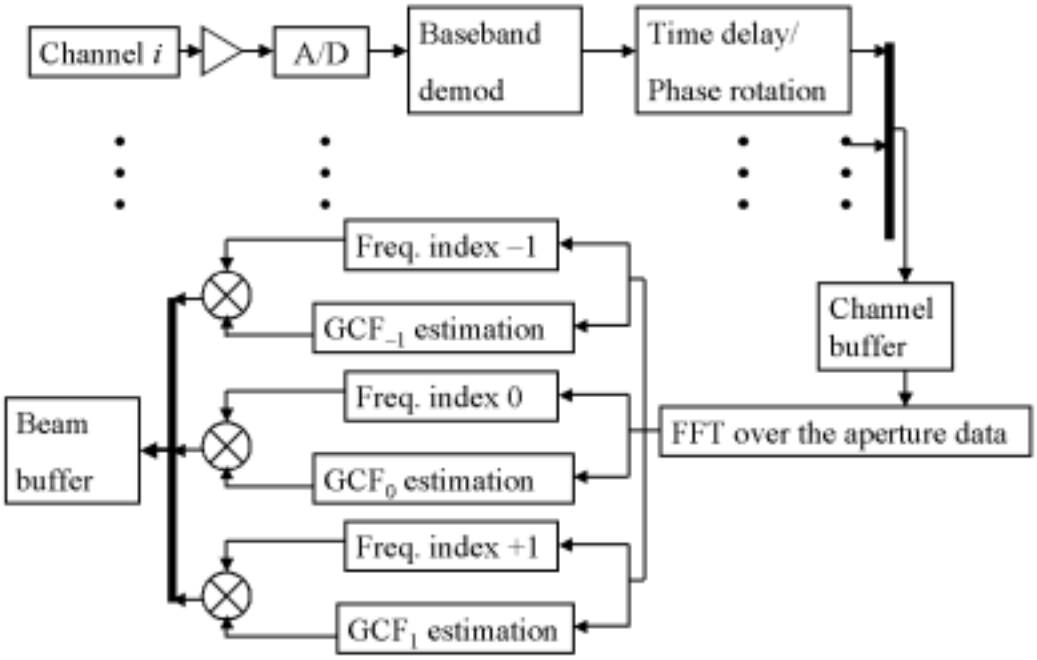

Fig. 4.3. System block diagram of the adaptive weighting technique for three beams.

4.4 Experimental Results

In this section, emulated images using real ultrasound data are presented to evaluate the efficacy of the proposed technique. All the raw data files are available from http://bul.eecs.umich.edu. They were acquired using a 128-element, 3.5-MHz

phased-array transducer (Acuson V328, Mountain View, California, USA) at a 13.8889-MHz sampling rate. Data from a wire phantom and a tissue-mimicking phantom were used. The wire phantom consisted of six nylon wires in water, arranged at ranges of 34, 48, 65, 83, 101, and 121 mm. For all images, the transmit focus was 60 mm from the transducer, and dynamic receive focusing with an f-number of 1.5 was applied. Here three receive beams were reconstructed. Since the entire array transducer (i.e., 128 channels) was used on receive, according to Eqs. (4.3) and (4.4), the middle 64 channels were used on transmit, and a 192-point FFT was applied for parallel reconstruction. Cutoff frequencies of M_0=2 and M_0=8 were used for the wire phantom and the tissue-mimicking phantom, respectively. In addition, since the receive beams are along different directions relative to the center of the transmit beam, the resulting variations among the parallel receive beams result in asymmetry in the two-way beam pattern. For the formation of n parallel receive beams, this causes periodic variations of the image intensity (with a period equal to n). The variations are more pronounced when the steering angle is larger. Hence, an n-tap moving-average filter (i.e., with filter coefficients of [1/n 1/n … 1/n]) needs to be applied laterally to smooth out these artifacts. All images are shown here in the format after scan conversion (i.e., the horizontal axis is the lateral distance in millimeters, and the vertical axis is the depth away from the transducer in millimeters).

4.4.1 Wire Phantom

Fig. 4.4 shows the images for the wire phantom, displayed with an 80-dB dynamic range. Fig. 4.4(a) is the image with standard scanning (i.e., one receive beam along the transmit direction for each transmit event). Fig. 4.4(b) is the three-beam image assuming duplicate beam formers (i.e., three receive beams are reconstructed simultaneously by applying their corresponding time delays to the same channel data). Figs. 4.4(c) and (d) are the three-beam images using FT-based parallel reconstruction before and after GCF weighting, respectively. The channel counts on transmit and receive for the four cases are the same. The width of the four images is 110 mm, and the depth ranges from 21.79 mm to 131.79 mm. Note that the two parallel-reconstructed images (Figs. 4.4(b) and (c)) look similar, but the signal-to-noise ratio (SNR) is lower than in the image with standard scanning (Fig. 4.4(a)). Comparison of Figs. 4.4(c) and (d) reveals that both the sidelobe level and image background noise are noticeably suppressed by the adaptive weighting technique.

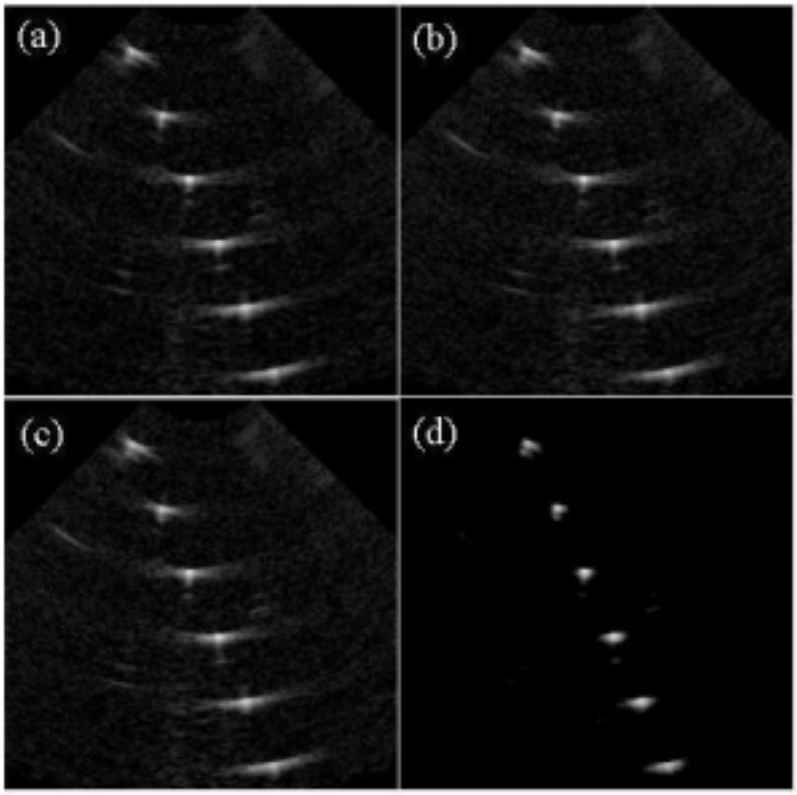

Fig. 4.4. Images of a six-wire phantom, displayed with an 80-dB dynamic range. The vertical axis is the depth and the horizontal axis is the lateral distance. (a) is the image with standard scanning. (b) is the three-beam image assuming duplicate beam formers. (c) and (d) are the three-beam images of FT-based parallel reconstruction without and with GCF weighting, respectively.

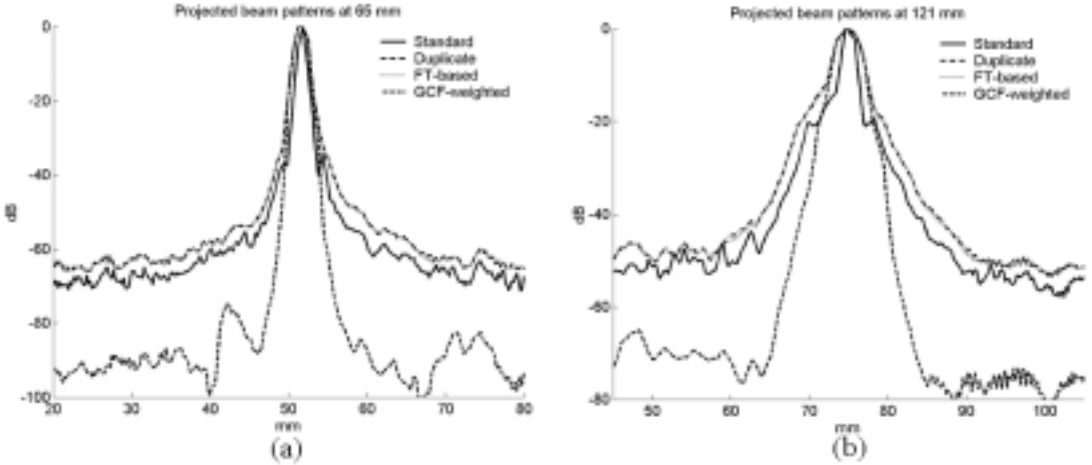

Fig. 4.5. Projected radiation patterns of the two wires at 65 mm (a) and 121 mm (b) in Fig. 4.4. The solid lines are the case with standard scanning. The dotted–dashed line is the three-beam case assuming duplicate beam formers. The dotted and dashed lines are the three-beam cases using FT-based parallel reconstruction before and after adaptive weighting, respectively.

Figs. 4.5(a) and (b) show the projected beam patterns of the wires at 65 and 121 mm, respectively, of the images in Fig. 4.4. For both wires, note that the beam

patterns of both parallel-reconstructed images have wider mainlobes than those with standard scanning. The moving-average filter widens the mainlobe and hence degrades the lateral resolution, although this also can reduce the image-intensity variations resulting from the transmit beam asymmetry. The beam pattern of FT-based parallel reconstruction has higher sidelobes and noise level than that with standard scanning. The sidelobe level of the FT-based parallel-reconstructed image is suppressed by about 10 dB after weighting. In addition, the noise floor of the weighted image is about 20 dB lower than that of the unweighted image when using FT-based parallel reconstruction.

4.4.2 Tissue-Mimicking Phantom

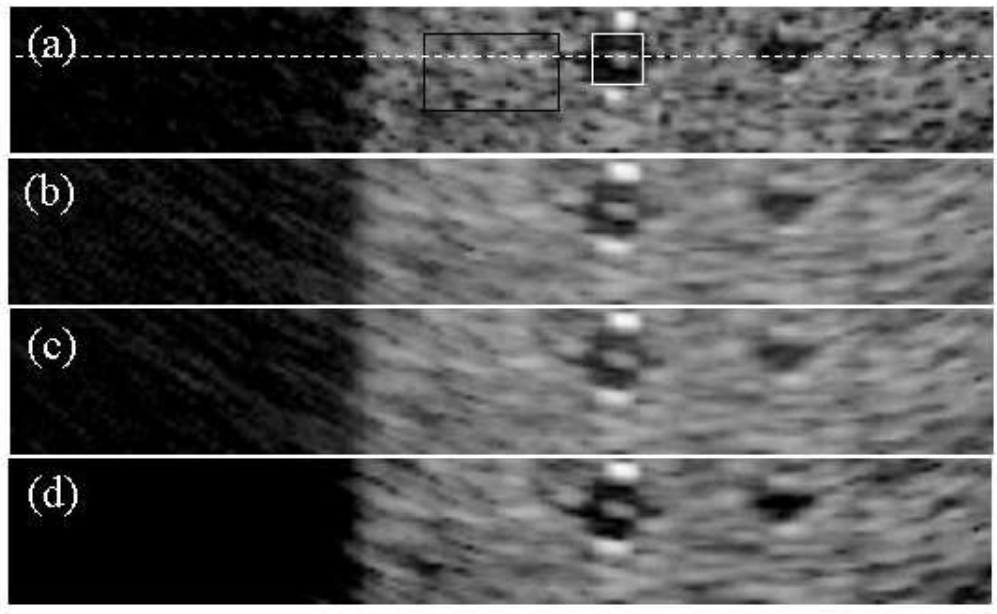

Fig. 4.6. Images of a tissue-mimicking phantom with anechoic cysts, displayed with a 40-dB dynamic range. The vertical axis is the depth and the horizontal axis is the lateral distance. (a) is the image with standard scanning. (b) is the three-beam image assuming duplicate beam formers. (c) and (d) are the three-beam images of FT-based parallel reconstruction without and with GCF weighting, respectively. The black and white boxes indicate the background and cyst regions used for CNR calculations, respectively.

Data from a tissue-mimicking phantom (RMI-412R, Gammex RMI, Middleton, Wisconsin, USA) with anechoic cysts were also used to evaluate the efficacy of the adaptive weighting technique in improving contrast resolution. Images (with a 40-dB dynamic range) in the vicinity of a cyst at 72 mm are shown in Fig. 4.6 Figs. 4.6(a)–(d) are the images with standard scanning, duplicate beam formers, FT-based parallel reconstruction, and GCF weighting, respectively. The width of the four images is 75.20 mm; the depth ranges from 68.42 mm to 79.16 mm. Fig. 4.6 shows that GCF

weighting improves the image quality of FT-based parallel reconstruction. The cyst detection is noticeably improved after adaptive weighting in that the weighted image is less “filled in” in the cyst region than the image using FT-based parallel reconstruction without weighting. The weighted image also exhibits superior edge definition and sharper contrast. Again, the image background noise is suppressed by adaptive weighting. Fig. 4.7 shows the image intensity along the horizontal white dashed line shown in Fig. 4.6(a). In addition to sidelobe reduction, GCF weighting reduces the noise floor in the left portion of the image by about 20 dB.

The CNR is employed to quantitatively evaluate the improvement in contrast resolution. The black and white boxes in Fig. 4.6(a) indicate the background and cyst regions used for CNR calculation, respectively. The CNRs are 1.98 for the standard-scan image, 2.29 for the parallel-reconstructed image with duplicate beam formers, 2.33 for the FT-based parallel-reconstructed image, and 2.64 for the GCF-weighted image. Because the moving-average filter reduces speckle noise, the CNR in the two parallel-reconstructed images (Figs. 4.6(b) and (c)) is higher than that with normal scanning. Nonetheless, the CNR is further increased after weighting. It is demonstrated that adaptive weighting can effectively improve the image quality of FT-based parallel reconstruction by reducing the sidelobes.

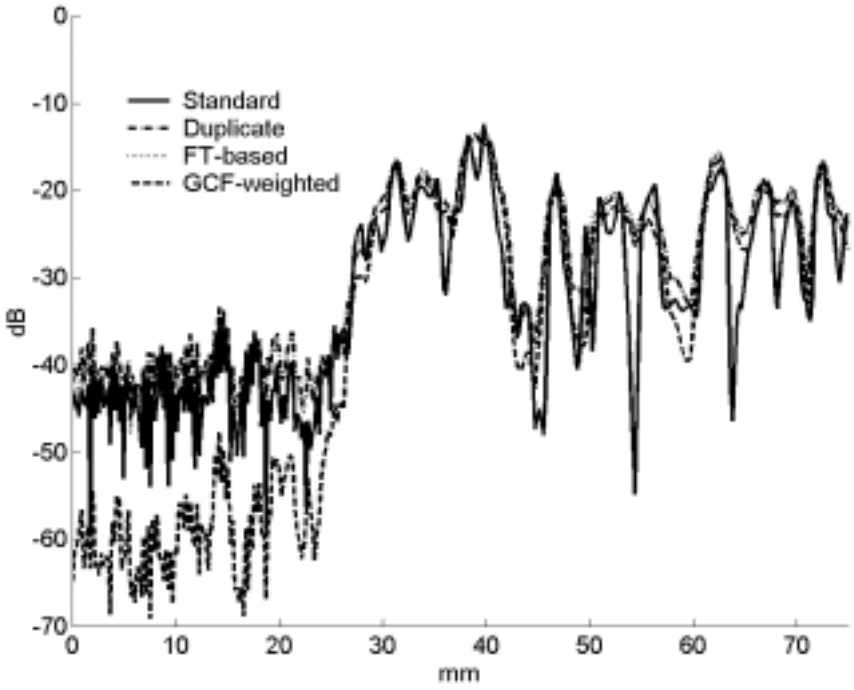

Fig. 4.7. The image intensity of the four images in Fig 4.6 along the horizontal white dashed line shown in Fig. 4.6(a).

4.5 Concluding Remarks

In this chapter, this adaptive weighting technique using the GCF has been extended to improve the degraded beam quality of the FT-based technique for forming parallel receive beams. Experimental results from a wire phantom and a tissue-mimicking phantom demonstrate the effectiveness of the adaptive weighting technique: the sidelobe level was effectively suppressed and contrast resolution was noticeably improved. The image background noise was also lower after applying the weighting. Due to the relationship between parallel receive beams and the Fourier spectrum over the aperture data, this weighting technique can be implemented efficiently. The proposed GCF technique can be incorporated into FT-based parallel reception systems with only minor modifications.

The GCF in Eq. (4.5) is defined without taking noise into consideration. The relationship between GCF without noise (i.e., an infinite SNR) and the estimated GCF with a finite SNR (denoted by GCF') has been described in Eq. (2.6). If the SNR is much less than unity, the estimated GCF can be expressed as

$$\mathrm{GCF}' \approx \frac{(2 \cdot M_0 + 1)}{N}. \tag{4.7}$$

In our case, given M_0 = 8 and N = 192, the estimated GCF is about 0.09. Since the SNR in the image background (i.e., the anechoic region) is very low, applying such weighting reduces the image intensity. Thus, as shown in section (4.4), the adaptive weighting technique effectively suppresses the noise floor in the image background. In addition, a simple moving-average low-pass filter is used to smooth out the image-intensity variations resulting from beam asymmetry in this chapter. However, such a simple filter reduces the spatial resolution in all types of parallel beam forming techniques.

The proposed GCF weighting technique can be directly extended to improving the quality of real-time 3D imaging using 2D arrays. For 3D imaging using 2D arrays, the GCF of one reconstructed receive beam (l,m) can be defined as follows:

$$\mathrm{GCF}_{l,m} = \frac{\sum_{k_x=-M_{x0}+l}^{M_{x0}+l} \sum_{k_y=-M_{y0}+m}^{M_{y0}+m} \left| p(k_x, k_y) \right|^2}{\sum_{k_x=N_x/2}^{N_x/2-1} \sum_{k_y=N_y/2}^{N_y/2-1} \left| p(k_x, k_y) \right|^2}, \tag{4.8}$$

where $p(k_x,k_y)$ is the 2D Fourier spectrum over the 2D aperture data with N_x points in the lateral direction and N_y points in the elevational direction, k_x and k_y are the 2D spatial indices along the lateral and elevational directions of the 2D array, respectively, and M_{x0} and M_{y0} are the cutoff frequencies specifying the frequency range in the spatial frequency domain (i.e., from $-M_{x0}$ to M_{x0} and from $-M_{y0}$ to M_{y0}). Although the results demonstrated here are only for 2D imaging using 1D arrays, it is expected that the proposed weighting technique can produce similar improvements to 3D imaging with the FT-based technique for forming parallel receive beams using 2D arrays.

Chapter 5 Applications in High-Frequency Ultrasound Imaging

5.1 Introduction

Ultrasonic imaging in the 2–15 MHz range is used routinely in clinical settings. However, the spatial resolution of conventional ultrasonic imaging systems is inadequate in certain applications. Since resolution improves with the increasing center frequency and the increasing bandwidth, specialized high-frequency ultrasonic imaging systems have been recently developed for the imaging of small-scale superficial structures such as the skin, the anterior chamber of the eye, and mouse embryos [43]–[49].

High-frequency ultrasound has shown promise for clinical use, but several limitations exist. The major problem in high-frequency imaging is tissue attenuation limiting the penetration and reducing the signal-to-noise ratio (SNR). In addition, high-frequency array transducers are still under development, and hence a mechanically scanned, single-crystal transducer with a fixed focus is typically used. Consequently, the image quality is significantly deteriorated in the out-of-focus region [50]–[53].

To improve the image quality of a fixed-focus imaging system, Passman and Ermert proposed a synthetic aperture focusing technique (SAFT) with a virtual source element [50], [51]. The technique increases the penetration and extends the limited depth of focus of a strongly focused transducer; in their case a depth-independent resolution was achieved. Synthetic aperture processing treats the transducer's geometric focus as a virtual source which is assumed to produce an approximately spherical wavefront over a limited angular extent. The fixed-focus single-crystal transducer is mechanically scanned to acquire a line of data at each scan position. Then, the SAFT is performed by appropriately delaying and summing the scan lines using the virtual-source concept. Frazier and O'Brien examined the tradeoffs between system complexity, grating lobes, and the SNR of the synthesized image in SAFT [52]. Since the sidelobe level of SAFT is high, apodization was applied to reduce sidelobes and to improve contrast resolution [52], [53]. The tradeoff between lateral resolution

and sidelobe level with apodization was also studied.

In this chapter, the GCF weighting technique developed for array beamforming is extended to SAFT. The adaptive weighting is also based on a focusing-quality index, similar to the GCF described in chapter 2; here it is employed to reduce the sidelobes of SAFT. The focusing-quality index of SAFT is derived from the spatial spectrum of the scan-line data along the mechanical scan direction (i.e., the synthetic aperture direction) after appropriate focusing delays relative to the virtual source have been applied. The proposed technique is of particular value in high-frequency ultrasound where dynamic focusing using array transducers is not yet possible. Experimental ultrasound data from a 50-MHz imaging system with a single-crystal transducer (f-number=2) are used to demonstrate the efficacy of the proposed technique on both wire targets and speckle-generating objects. An *in vivo* experiment is also performed on a mouse to further demonstrate the effectiveness. Both 50-MHz fundamental imaging and 50-MHz tissue harmonic imaging are tested. The results clearly demonstrate the effectiveness in sidelobe reduction and background-noise suppression for both imaging modes. The principles, experimental results, and implementation issues of the new technique are also described in this chapter.

5.2 SAFT with a Virtual Source

The SAFT used in this chapter treats the transducer's focal point as a virtual source, as shown in Fig. 5.1(a). The virtual source is assumed to produce a wave propagating both forward and backward with respect to itself that is spherical within a certain angular extent. If a linear scan is performed with the transducer, the sound field generated by the virtual source at the current position will overlap with the sound fields produced at adjacent positions. Hence, synthetic aperture focusing can be performed in the overlapping region before and after the virtual source. As an example, the points p_1 and p_2 in Fig. 5.1(a) are in the overlapping region after and before the virtual source, and can be synthetically focused using the received scan lines at which the points p_1 and p_2 are illuminated by the sound field [52], [54].

Fig. 5.1(b) further illustrates the virtual-source concept. The scan line i is a distance x_i away from the axis of the synthesized beam. The sound field of scan line i propagates through the desired focal point p. Hence, the echo signal from scan line i can be added to the beam constructively by applying an appropriate time delay. Based on the virtual-source concept, the time delay applied to the received signal of scan line

i is expressed as

$$\Delta t_i = 2 \cdot \mathrm{sgn}(z - z_\mathrm{f}) \cdot \frac{(r' - r)}{c}, \tag{5.1}$$

where z is the depth of the synthetic focal point p, z_f is the transducer's focal depth, r=abs(z–z_f) is the axial distance from the transducer's focal depth to the synthetic focal depth, $r'=\sqrt{r^2 + x_i^2}$ is the distance from the virtual source f_i to the synthetic focal point, c is the speed of sound, and sgn(·) is the signum function. Note that if the synthetic focal point is located in front of the transducer's focal point, the time delay is negative. After appropriate delays relative to the virtual source are applied to all corresponding scan lines according to Eq. (5.1), SAFT is implemented as the following sum:

$$S_\mathrm{SAFT}(t) = \sum_{i=0}^{N-1} S(i, t - \Delta t_i), \tag{5.2}$$

where $S(i,t)$ is the received signal at the scan line i. The maximum number of scan lines included in the sum of Eq. (5.2) is denoted by N and is determined by the angular extent of the virtual-source sound field [50]–[52], where a wider angular extent allows more scan lines to contribute to the sum. Hence, a more tightly focused beam can be synthesized after SAFT is applied since the effective aperture size is increased. Note that around the focal point of the transducer, the number of scan lines that can contribute to focusing is limited. Such a drastic change in the number of available scan lines causes discontinuity in the SAFT image, which can be reduced by applying appropriate gain compensation [54].

The procedures of the SAFT are further illustrated in Fig. 5.1(c), in which the horizontal axis of each panel is the scan-line index and the vertical axis represents the depth. The top panel shows all the simulated radio frequency (RF) scan lines for a point beyond the focal depth with the transducer being linearly scanned. Each line represents the RF A-scan data at that position, and the entire panel represents the unfocused beam profile. As an example, the scan lines in the black rectangular box are used to synthesize the beam with a direction denoted by the arrow (the scan lines in this region are magnified in the middle panel). The number of scan lines in the black box is determined by the angular extent of the virtual-source sound field [52]. The bottom panel presents the delayed version of data shown in the middle panel, demonstrating that all the scan lines are aligned after the delays are applied. Summing the delayed scan lines along the horizontal axis produces a beam with a synthetic

focus. Note that the delayed scan lines are not identical, with the amplitude variations corresponding to the unfocused beam profile at that depth. This is different from received array channel data, where the radiation pattern of each individual channel is more uniform. In addition, a baseband SAFT is implemented in this chapter to reduce the data sampling requirements associated with a high-frequency system [55].

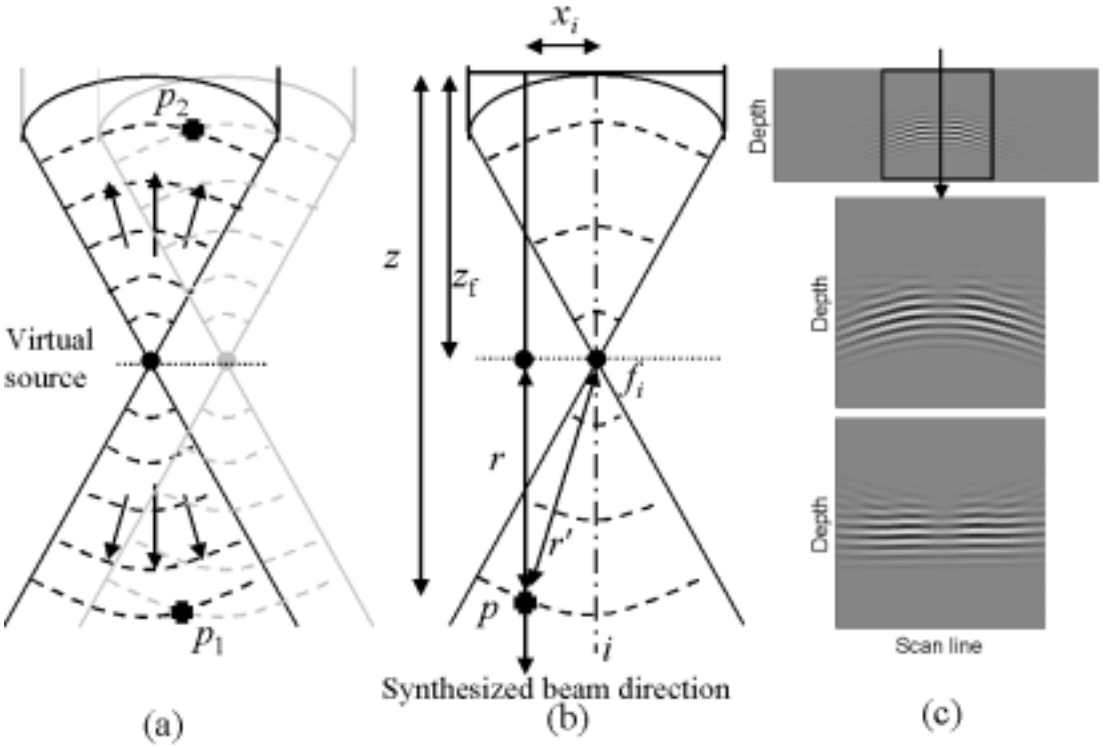

Fig. 5.1. (a) Schematic diagram of the virtual-source concept. (b) Focusing geometry for the SAFT with a virtual source, where z is the depth of the synthetic focal point p, z_f is the transducer's focal depth, r is the axial distance from the transducer's focal depth to the synthetic focal depth, r' is the distance from the virtual source f_i to the synthetic focal point p. (c) Illustration of the SAFT procedure; in each panel the lateral axis is the scan-line index and the vertical axis represents the depth. The top panel shows all the simulated RF scan lines for a point beyond the focal depth. The middle panel is the magnified version of the scan-line data in the black rectangular box shown in the top panel. The bottom panel shows the delayed version of the middle panel.

5.3 The Adaptive Weighting Technique

In this section, the GCF weighting technique proposed for array beam formation is extended to SAFT. For SAFT with a virtual source, the weighting factor is derived from the spatial spectrum of the delayed scan-line data, which is the data received by the single-element transducer at each scan position after the focusing delays of the corresponding virtual source are applied prior to beam summation. The N-point

discrete Fourier spectrum of the delayed scan-line data along the primary scan direction can be expressed as

$$p(k,t) = \sum_{i=0}^{N-1} S_{\text{delayed}}(i,t) e^{-j2\pi \frac{ik}{N}}, k = -N/2, -N/2+1, ..., N/2-1, \quad (5.3)$$

where $S_{\text{delayed}}(i,t)$ is the delayed signal of scan line i, N is the total number of scan lines included in the sum of Eq. (5.2), and k is the spatial frequency index. Note that if baseband scan-line data is used, the Fourier spectrum along the scan direction can be viewed as the approximation of the two-way radiation pattern (i.e., transmit and receive) centered on the direction of the synthesized beam [29], [31]. The dc component (i.e., $p(0,t) = \sum_{i=0}^{N-1} S_{\text{delayed}}(i,t)$) represents the beam sum of the delayed scan-line data, and it corresponds to the signal from the direction of the synthesized beam direction, i.e. the main lobe. The high-frequency components correspond to the scattered signals from other angles, i.e. the sidelobes, when baseband scan-line data is used.

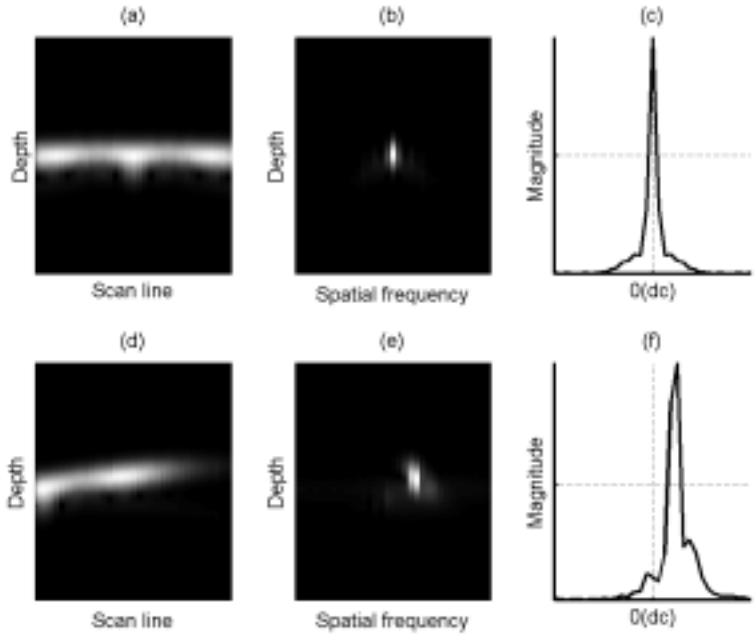

Fig. 5.2. Delayed baseband scan-line data and the associated spectra along the scan direction for a point target. The top panels are for the case where a wire is in the direction of the synthesized beam, located 1.2 mm in front of the focal point. The bottom panels show the case where the wire is off the synthesized beam axis. In each case, the left column ((a) and (d)) shows the amplitude of the delayed baseband scan-line data, with the horizontal axis representing the scan-line index and the vertical axis denoting the depth; the middle column ((b) and (e)) shows the spectrum at each depth; and the right column ((c) and (f)) is the projection of the data shown in the middle column.

Fig. 5.2 shows simulated baseband scan-line data and the associated spectra along the scan direction. A single-crystal transducer with a diameter of 6 mm and a geometric focus at 12 mm was simulated. The simulated transducer's center frequency was 50 MHz of 55% –6 dB fractional bandwidth. The transmit signal was a Gaussian pulse with a center frequency of 50 MHz. The spacing between two adjacent scan lines was 10 μm. The top panels in Fig. 5.2 present the case where a point target was in the direction of the synthesized beam, located 1.2 mm in front of the focal point. Fig. 5.2(a) shows the amplitude of the delayed baseband scan lines, where the vertical axis is the depth and the horizontal axis is the scan direction. It can be seen that the scan lines are generally in phase (i.e., horizontal wavefront), but the amplitude variations are large since the point target was illuminated by an unfocused beam. Fig. 5.2(b) shows the corresponding one-dimensional Fourier transform of the delayed scan lines along the scan direction at each range, with the horizontal axis representing the spatial frequency index k from $-N/2$ to $N/2-1$. Fig. 5.2(c) is the projected spectrum of Fig. 5.2(b), and the vertical dotted line indicates dc (i.e., the direction of the synthesized beam). The maximum along the depth direction is used for the projection. Though the data along the scan direction exhibit amplitude variations, the spectrum energy is primarily concentrated in the low-frequency region near dc (i.e., the direction of the synthesized beam).

The bottom panels of Fig. 5.2 show the case where the point target was off the synthesized beam axis, with the other conditions unchanged. In other words, this corresponds to a steering error of SAFT. Fig. 5.2(d) shows that the delayed data are no longer in phase, with the slope of the (tilted) wavefront corresponding to the direction of the point target. In other words, the scan-line data at each range are modulated. Hence, the corresponding spectrum energy along the scan direction is generally concentrated in the object direction instead of in the direction of the synthesized beam, as shown in Figs. 5.2(e) and (f). A significant portion of the spectrum energy is distributed in the higher frequency region of the spectrum (i.e., away from the direction of the synthesized beam). In this case, the contribution of the off-axis target to the primary beam direction needs to be minimized.

The simulated data in Fig. 5.2 shows that the spectrum of the scan-line data can be used to approximate the radiation pattern and to determine the focusing quality of SAFT. The focusing quality of SAFT is directly related to the ratio of the energy in the low-frequency region (around dc) to the total energy (i.e., the ratio of the energy received from angles near the direction of the synthesized beam to the total energy from all directions if baseband scan-line data is used). Hence, such an energy ratio (ER) can be used as a focusing-quality index for SAFT, and it is similar to the

generalized coherence factor as described in chapter 2. According to the parameters defined in Eq. (5.3), the ER at a given depth can be expressed as

$$\mathrm{ER}(t) = \frac{\text{energy in the low - frequency region}}{\text{total energy}} = \frac{\sum_{k=-M_0}^{M_0} \left| p(k,t) \right|^2}{\sum_{k=-N/2}^{N/2-1} \left| p(k,t) \right|^2}. \qquad (5.4)$$

The discrete Fourier transform can be efficiently computed using the fast Fourier transform (FFT). The low-frequency region is specified by a cutoff frequency M_0 in the spatial frequency index. The procedure of ER calculation is illustrated in Fig. 5.3(a). Note that an M_0 of zero means that the low-frequency range used to estimate ER is restricted to dc only. However, since a speckle-generating target inherently contains a certain degree of incoherence, with diffuse scatterers the cutoff frequency M_0 should be large enough to allow for this.

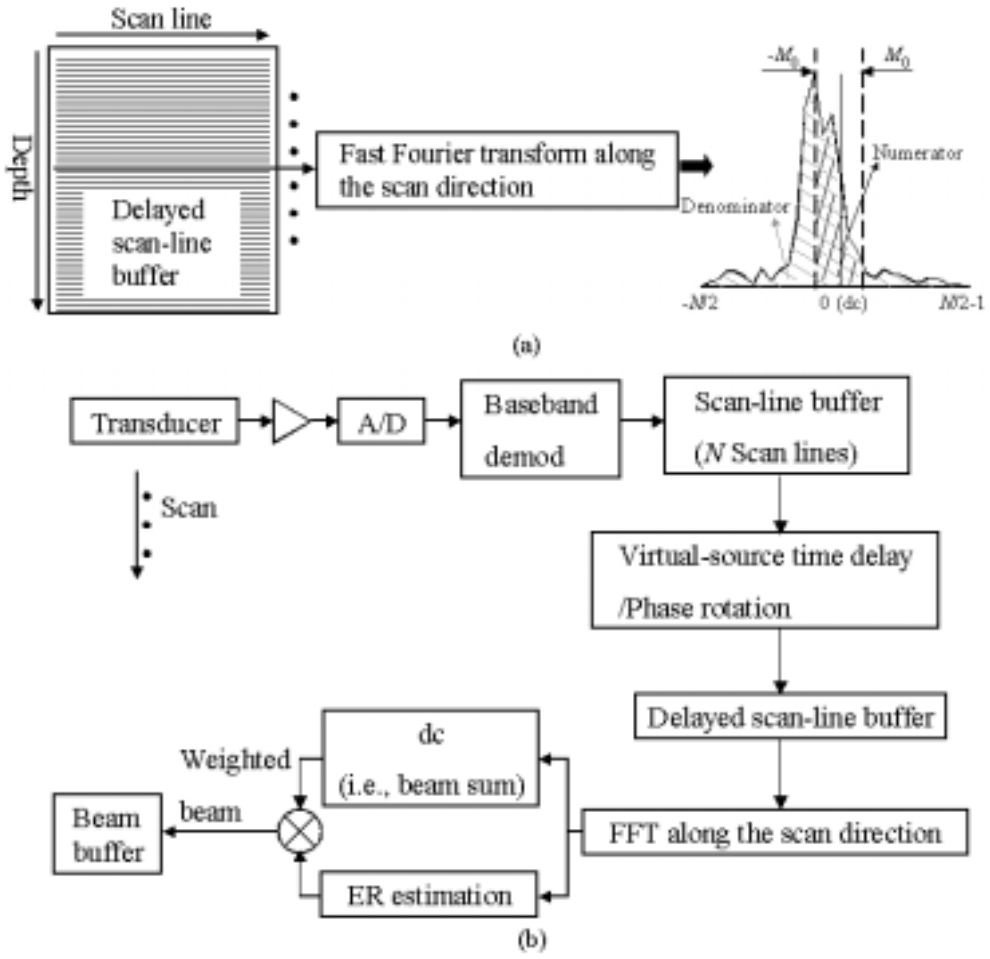

Fig. 5.3. (a) Schematic diagram showing how the ER is calculated. (b) System block diagram of the adaptive weighting technique for SAFT.

A high ER indicates that the image object is in the direction of the synthesized beam, and thus the image intensity should be maintained. A low ER, on the other hand, should be used to reduce the contribution of sidelobes from the outside objects to the image intensity. Hence, SAFT image quality can be improved by developing an adaptive weighting technique based on this property. The ER-weighted signal $S_{\text{weighted}}(t)$ of the SAFT signal $S_{\text{SAFT}}(t)$ at a given range can be expressed as

$$S_{\text{weighted}}(t) = \text{ER}(t) \cdot S_{\text{SAFT}}(t). \tag{5.5}$$

Note that for each beam, the weighting needs to be calculated and applied at each imaging depth. The weighting is calculated for each individual SAFT image. A system block diagram of the adaptive weighting technique for SAFT is shown in Fig. 5.3(b). As described previously, one reason for implementing the SAFT in baseband is to reduce the large data sampling rate associated with a high-frequency system. The transducer is linearly translated along the scan direction during data acquisition. The echo signal at each scan position is received and digitized by an analog-to-digital converter, and then the received RF data are demodulated down to baseband and stored in the scan-line buffer. After N scan lines are collected, appropriate virtual-source time delays and phase rotations are applied before the data are sent to the delayed scan-line buffer. The ER is then estimated using the FFT of the delayed baseband scan-line data (note that ER should be calculated at all depth points). The dc component of the spectrum (i.e., the beam sum) is then weighted by the ER, by multiplying the amplitude of the beam sum data by the corresponding ER on a point-by-point basis. The weighted data are then sent to the beam buffer for further signal processing and display.

5.4 Experimental Results

Experiments were conducted to investigate the efficacy of the adaptive weighting technique on sidelobe reduction in SAFT imaging. A lithium-niobate focused transducer (NIH Resource Center for Medical Ultrasonic Transducer Technology, Penn State University, University Park, PA) was used. The transducer's center frequency is 45 MHz of 55% –6 dB fractional bandwidth. The transducer has a diameter of 6 mm and is geometrically focused at 12 mm. A schematic diagram of the experimental setup is shown in Fig. 5.4. An arbitrary-function generator (Signatec DAC200, Corona, CA) was used to generate the desired transmit waveform, which

was then sent to a power amplifier (Amplifier Research 25A250A, Souderton, PA) to drive the lithium-niobate focused transducer. A three-axis motor system (CSIM, Taipei, Taiwan) was used to control the relative position between the target and the transducer. The transducer was stepped laterally, and the scan-line data acquired at each position were sent to an ultrasonic receiver (Panametrics 5900, Waltham, MA). Finally, the signal was sampled with an analog-to-digital converter operating at 500 Msamples/s and 8-bit resolution (Signatec PDA500).

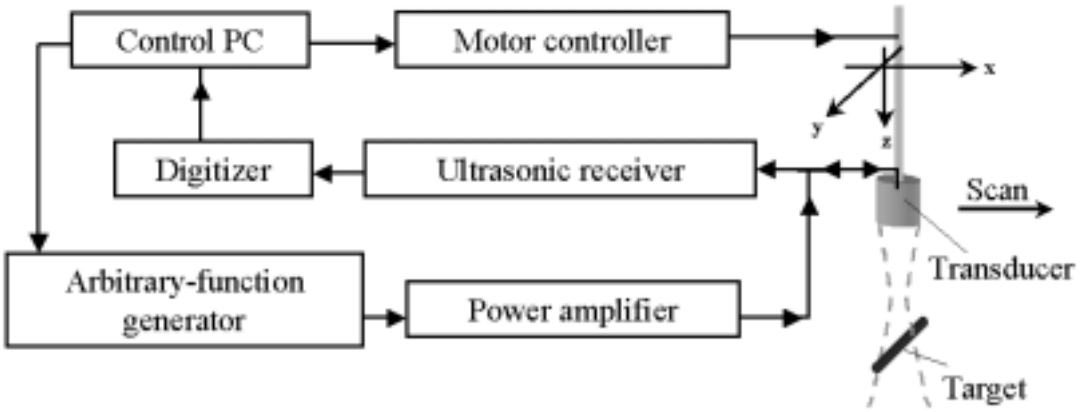

Fig. 5.4. Schematic diagram of the experimental setup.

The spacing between two adjacent scan lines was 10 μm for phantom imaging, which was smaller than half wavelength at the imaging frequency to reduce the grating lobe [52]. The maximum number of scan lines for beam synthesis was limited to 32 for all the following cases, although the actual number of available scan lines may have been larger. This limitation reduced the implementation complexity of SAFT, and sped up the ER calculation. The sound velocity was assumed to be 1.48 mm/μs. The depths of the imaged targets were estimated using the assumed sound velocity. In addition, M_0=1 and M_0=3 were used to calculate the ER for wire targets and speckle-generating targets, respectively. All images were displayed with a 55-dB dynamic range.

5.4.1 Wire Target

The wire target comprised a nylon wire with a diameter of 52 μm. For 50-MHz fundamental imaging, a Gaussian pulse with a center frequency of 50 MHz was transmitted. Fig. 5.5 shows the results when the wire target was located at a depth of 12.6 mm, which was 0.6 mm beyond the focal depth. Figs. 5.5(a), (b), and (c) show the 50-MHz original, SAFT, and SAFT-plus-weighting images, respectively, where the vertical axis is the depth and the horizontal axis is the lateral position, both in

millimeters. Although SAFT improves the image quality over the original image, the sidelobe level of the SAFT image is still high. This high sidelobe level is noticeably suppressed by the adaptive weighting technique, as shown in Fig. 5.5(c). Note that the image background noise is also reduced after adaptive weighting. Figs. 5.5(d) and (e) show the axial and lateral projections of the images shown in Figs. 5.5(a), (b), and (c). The sidelobe level of the SAFT image is suppressed more than 10 dB after weighting. The axial projection shows that the noise floor of the weighted image is about 8 dB lower than that of the SAFT image. Fig. 5.6 shows the results where the wire target was located at a depth of 10.76 mm, which was 1.24 mm in front of the focal depth. As in Fig. 5.5, significant image quality improvement is achieved with adaptive weighting.

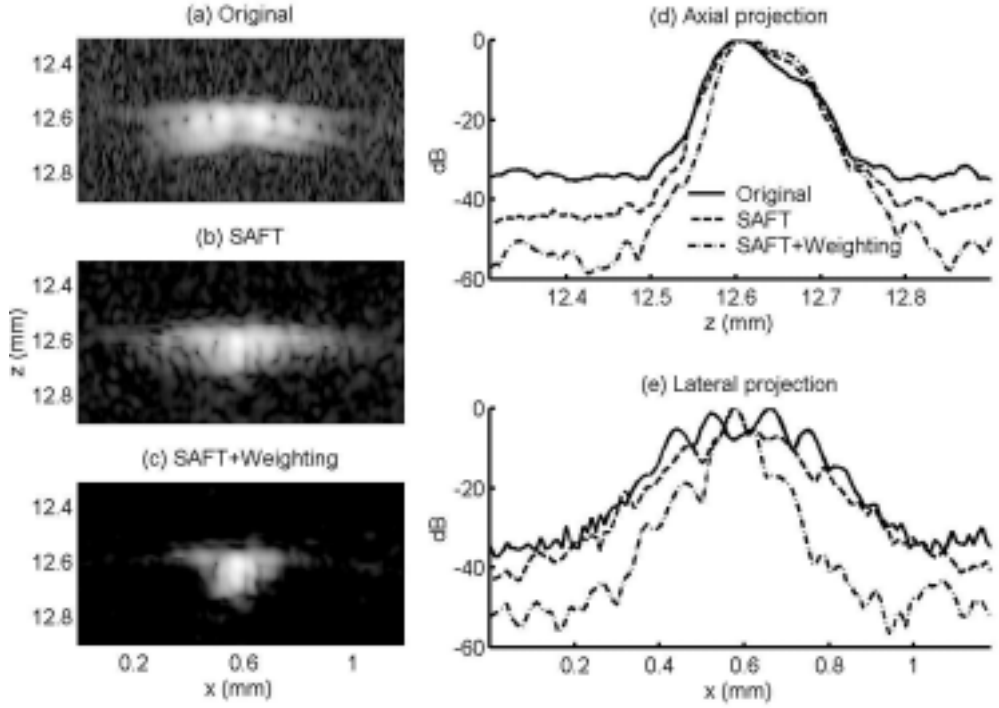

Fig. 5.5. Experimental results for a wire target located at a depth of about 12.6 mm. (a), (b), and (c) show the 50-MHz original, SAFT, and SAFT-plus-weighting images, respectively, where the vertical axis is the depth and the horizontal axis is the lateral position, both in millimeters. (d) and (e) show the axial and lateral projections of the images shown in (a), (b), and (c). The solid lines are the original case, the dashed lines are the SAFT case, and the dash–dotted lines are the case after adaptive weighting. The images shown here and in subsequent figures are displayed with a 55-dB dynamic range.

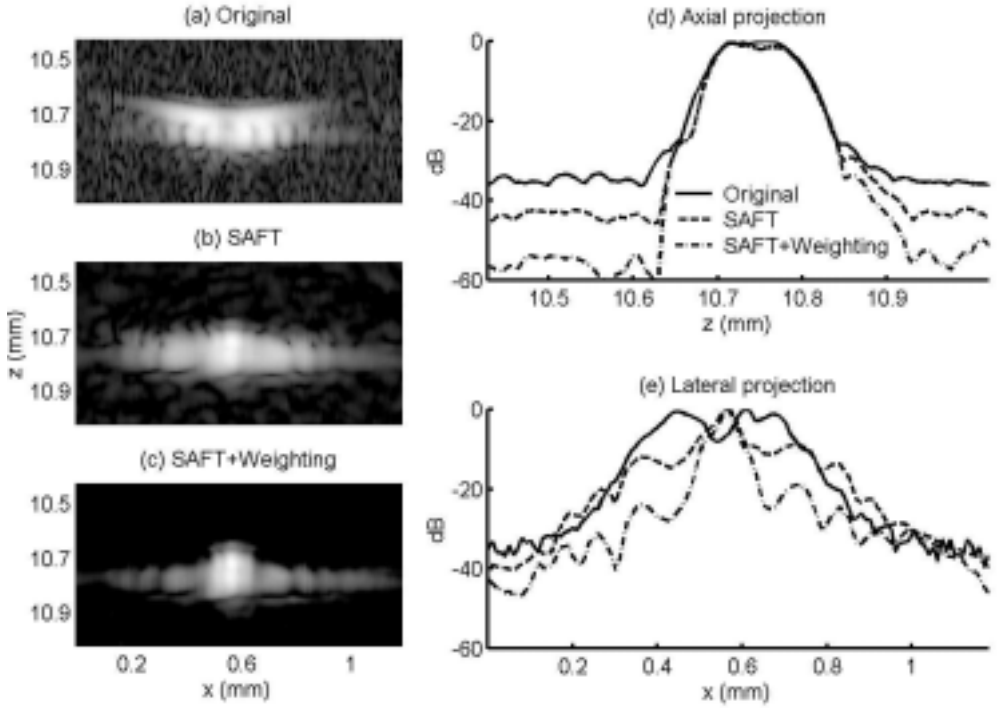

Fig. 5.6. Experimental results for a wire target located at the depth of 10.76 mm. (a), (b), (c) show the 50-MHz original, SAFT, and SAFT-plus-weighting images, respectively, where the vertical axis is the depth and the horizontal axis is the lateral position, both in millimeters. (d) and (e) show the axial and lateral projections of the images shown in (a), (b), and (c). The solid lines are the original case, the dashed lines are the SAFT case, and the dash–dotted lines are the case after adaptive weighting.

5.4.2 Anechoic Cyst

A gelatin-based phantom was also constructed and imaged to demonstrate the efficacy of the adaptive weighting technique on improving contrast resolution. The gelatin-based phantom had a 500 μm anechoic region (a cyst) at its center and graphite powder (1–2 μm, Aldrich Chemical, Milwaukee, WI) distributed uniformly in the background. Figs. 5.7(a), (b), and (c) show the original, SAFT, and SAFT-plus-weighting images, respectively. The center of the cyst was located at a depth of 13.15 mm, which was 1.15 mm beyond the focal depth. The vertical axis is the depth and the horizontal axis is the lateral distance, both in millimeters. Fig. 5.7 shows that detection of the cyst is noticeably improved after the adaptive weighting technique: the weighted image is less “filled in” in the cyst region than the SAFT image.

The CNR is employed to quantitatively evaluate the improvement in contrast resolution. Note that the background and cyst regions used for CNR calculation are indicated by the left- and right-hand white boxes in Fig. 5.7(c), respectively. The CNRs are 1.20 for the original image, 2.02 for the SAFT image, and 2.67 for the

SAFT-plus-weighting image, which demonstrates that adaptive weighting results in a higher CNR.

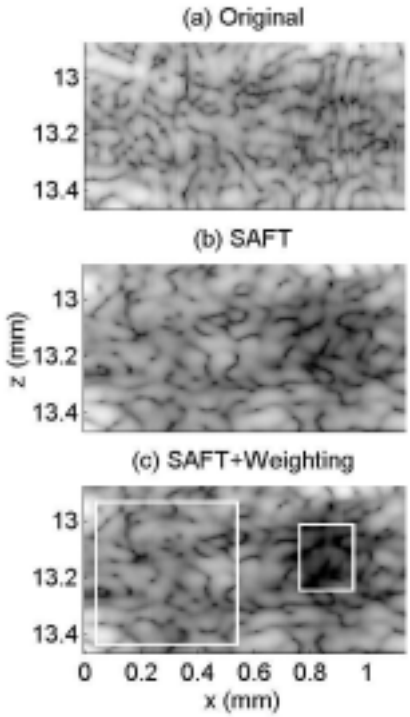

Fig. 5.7. Images of an anechoic cyst. The vertical axis is the depth and the horizontal axis represents the lateral position, both in millimeters. (a), (b), (c) show the 50-MHz original, SAFT, and SAFT-plus-weighting images, respectively. The two white boxes indicate the cyst and the background regions used for CNR calculations.

5.4.3 50-MHz Second Harmonic Imaging

The effectiveness of the adaptive weighting technique on tissue second harmonic imaging was also tested. For 50-MHz second harmonic imaging, a Gaussian pulse at 25 MHz was used on transmit such that the second harmonic signal at 50 MHz can obtain at an adequate SNR in our high frequency imaging system. In this case, the received second-harmonic signal at 50 MHz was extracted by the pulse-inversion technique which can reduce harmonic leakage resulting from the transmit waveform and the system nonlinearities [56]–[60]. According to [61], the focal depth of the second-harmonic signal at such high frequencies is close to that of the fundamental signal at the same frequency. Hence, positions of the virtual sources for 50-MHz second-harmonic imaging are assumed to be the same as those for 50-MHz fundamental imaging. The same experimental setup as used for the previous fundamental-frequency experiments was employed, along with the same wire target. Fig. 5.8 shows the harmonic images where the wire target was located 0.69 mm beyond the focal depth. This figure has the same format and was obtained under the

same experimental conditions as Fig. 5.5. It is clearly shown that the adaptive weighting technique is also effective for tissue harmonic SAFT imaging, with the image background noise being also significantly reduced.

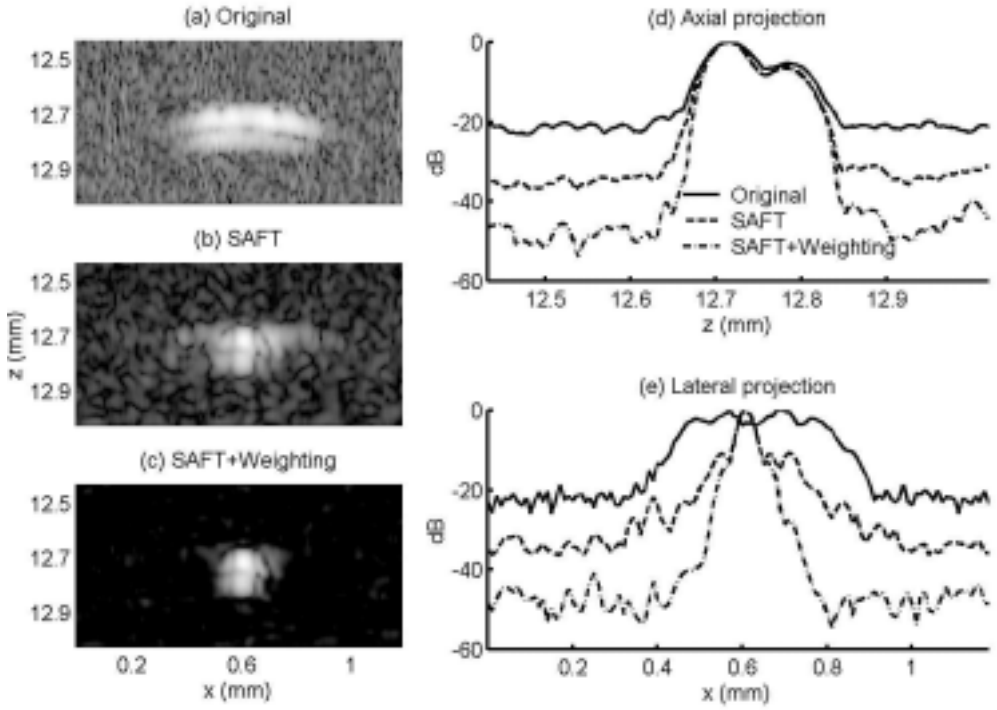

Fig. 5.8. 50-MHz second-harmonic experimental results for a wire target located 0.69 mm beyond the focal depth. (a), (b), (c) show the original, SAFT, and SAFT-plus-weighting images, respectively, where the vertical axis is the depth and the horizontal axis is the lateral position, both in millimeters. (d) and (e) show the axial and lateral projections of the images shown in (a), (b) and (c). The solid lines are the original case, the dashed lines are the SAFT case, and the dash–dotted lines are the SAFT-plus-weighting case.

5.4.4 *In-vivo* Imaging of a Mouse

An *in vivo* experiment on a mouse (C57BL/6) was also performed. The mouse was purchased from the National Animal Center, Taipei, Taiwan, R.O.C. and was housed in an animal room with good environmental control. Food and water were available *ad lib*. The use and care of animals were in accordance with the principles of the National Animal Center of R.O.C. The mouse was anesthetized with ether during imaging. The lower abdomen and back regions of the anesthetized mouse were wet shaved to provide a clear window to imaging. For *in vivo* mouse imaging, two Gaussian pulses at 25 MHz and 40 MHz were used here, and the spacing between two adjacent scan lines was 20 μm. Figs. 5.9(a), (b), and (c) show the corresponding 25-MHz original, SAFT, and SAFT-plus-weighting kidney images, respectively. Figs. 5.10(a), (b), and (c) show the 40-MHz original, SAFT, and

SAFT-plus-weighting embryo images, respectively. The transducer's geometric focal point was at 12 mm. The weighted images in Fig. 5.9(c) and Fig. 5.10(c) exhibit superior edge definition and sharper contrast than the SAFT images in Fig. 5.9(b) and Fig. 5.10(b), respectively, over the entire depth of imaging field. Again, the image background noise is also suppressed by adaptive weighting. Fig. 5.9(d) shows the scan-line data along the white dotted lines shown in Figs. 5.9(a), (b), and (c). In addition to sidelobe reduction, the noise floor in the anechoic region is about 10 dB lower than that without weighting.

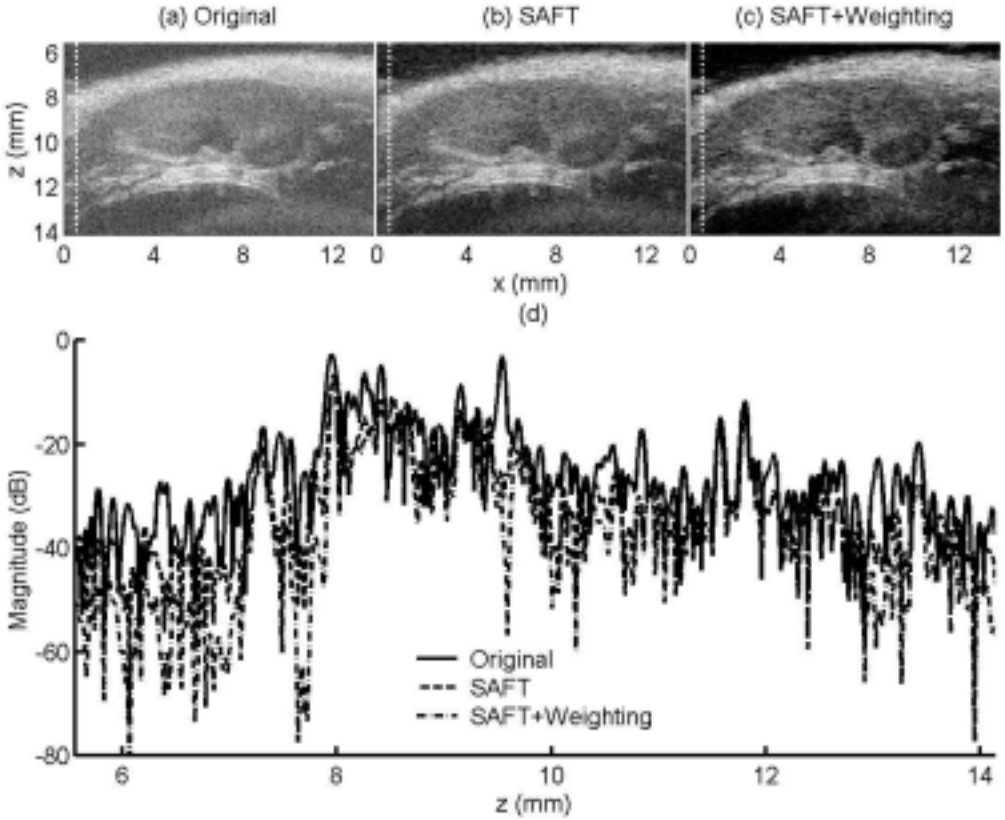

Fig. 5.9. 25-MHz *in vivo* imaging of a mouse kidney. (a), (b), and (c) show the 25-MHz original, SAFT, and SAFT-plus-weighting images, respectively, where the vertical axis is the depth and the horizontal axis is the lateral position, both in millimeters. (d) shows the scan-line data along the white dotted lines shown in (a), (b), and (c). The solid line is the original case, the dashed line is the SAFT case, and the dash–dotted line is the case after adaptive weighting.

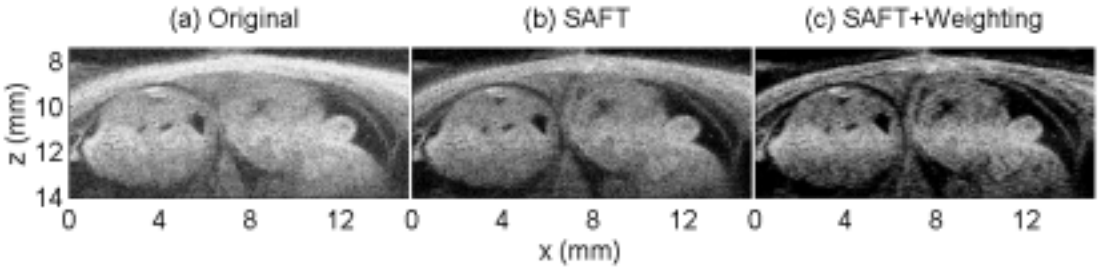

Fig. 5.10. 40-MHz *in vivo* imaging of mouse embryos. (a), (b), and (c) show the original, SAFT, and SAFT-plus-weighting images, respectively, where the vertical axis is the depth and the horizontal axis is the lateral position, both in millimeters.

5.5 Concluding Remarks

The ER in Eq. (5.4) is defined without taking noise into consideration. The relationship between ER without noise (i.e., an infinite SNR) and the estimated ER with a finite SNR (denoted by ER') can be expressed as (similar to Eq. (2.5))

$$\mathrm{ER}' = \frac{(\mathrm{ER}\cdot\mathrm{SNR} + \frac{2M_0 + 1}{N})}{1 + \mathrm{SNR}}, \tag{5.6}$$

where N is the number of points used for the FFT. If the SNR is much less than one, the ER' can be expressed as

$$\mathrm{ER}' \approx \frac{(2\cdot M_0 + 1)}{N}. \tag{5.7}$$

In this case the ER' is about 0.09 (i.e., for M_0 = 1 and N=32). Since the SNR in the image background (i.e., the anechoic region) is very low, the image intensity is reduced by applying weighting. Thus, as shown in the experimental results, the adaptive weighting technique effectively suppresses the noise floor in the image background. In addition, as defined in Eq. (5.4), ER fluctuates in a uniform speckle region. When SNR is taken into account, according to Eq. (5.6), fluctuation of ER' will be more serious since SNR varies in a uniform speckle region. Thus, speckle variance in a uniform speckle region may be increased after applying the adaptive weighting technique. To address this problem, the standard deviation of the image intensity is calculated in the background region of the anechoic cyst phantom in Section IV for the three cases: SAFT, SAFT-plus-weighting with M_0 = 1, and

SAFT-plus-weighting with M_0 = 3. The standard deviation of the ER-weighted image with M_0 = 1 is 3.5 dB higher than that of the SAFT image, while the standard deviation of the ER-weighted image with M_0 = 3 is only 0.54 dB higher than that of the SAFT image. That is, the effect of introducing higher speckle variance after weighting is more pronounced when a smaller M_0 is used, but it can be reduced with a larger M_0. Thus, a larger M_0 is generally more preferable for a speckle-generating target.

The adaptive weighting technique using the GCF in chapter 2 was developed for array beam formation to reduce the focusing errors resulting from sound-velocity inhomogeneities. In this chapter, the adaptive weighting technique was extended to reduce the sidelobes of the SAFT radiation pattern, and was applied successfully to high-frequency ultrasound where dynamic focusing using arrays is not yet feasible. Experimental results from a 50-MHz imaging system demonstrate the effectiveness of the adaptive weighting technique in both fundamental and tissue harmonic imaging. The sidelobe level was effectively suppressed and contrast resolution was significantly improved. In addition, the image background noise was lower after the weighting. Although the results are demonstrated only at certain imaging depths, it is expected that the proposed technique can be effectively applied wherever the SAFT is applicable. Finally, it is preferable for the proposed technique to be implemented with a baseband SAFT in order to reduce the requirement for high sampling rates associated with high-frequency systems.

Chapter 6 Discussion

6.1 GCF Weighting vs. Low-Pass Filtered CF Weighting

Due to the inherent incoherence of speckle-generating targets, variations of the CF map are large (i.e., speckle appearance, like B-mode images), as described in sections (2.4.1) and (3.1.2). Hence, with CF weighting, such a variation significantly increases the image speckle variance, and may cause image artifacts. In chapter 2, the notion of CF is generalized to cover objects with diffuse scatterers, and is referred to as GCF. The GCF has a smaller variation than the CF. Hence the GCF weighting is more suitable particularly for imaging a speckle-generating target. In this chapter, an alternative approach is used to smooth out the large variation of CF by spatial low-pass filtering CF map in azimuth. Note that the LPF{CF} weighting has lower computational complexity than the GCF weighting since the Fourier-transform operation is replaced by low-pass filtering. The simulated data of anechoic cyst in sections (2.3.2) and (3.3.2) are used to compare the various weighting functions (LPF{CF} and GCF) in terms of the effectiveness of the adaptive weighting on contrast improvement.

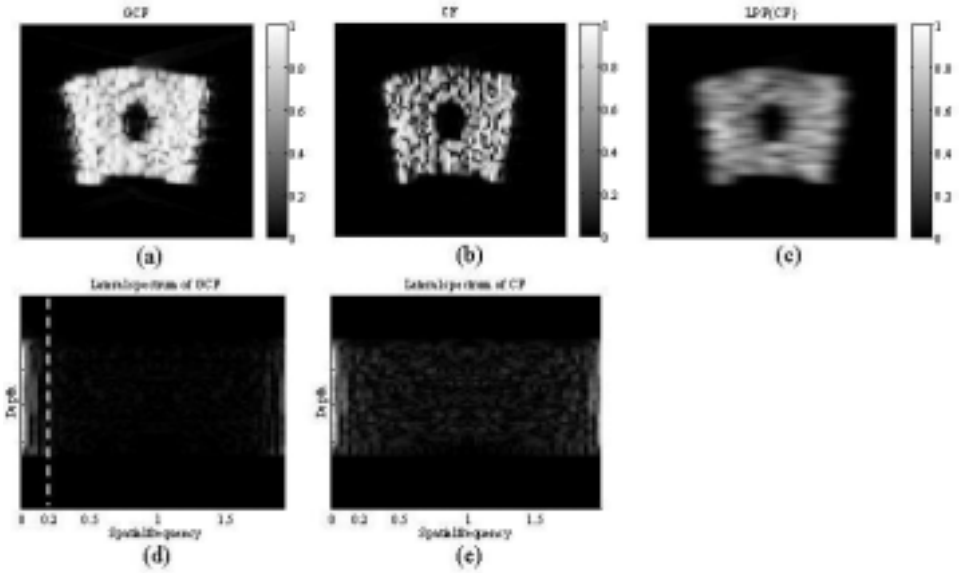

Fig. 6.1. GCF and CF maps of anechoic cyst simulation without aberrations, and their corresponding lateral spatial spectra along the azimuthal direction. (a) GCF map; (b) CF map; (c) LPF{CF} map; (d) Lateral spatial spectrum of GCF map along the azimuthal direction; (e) Lateral spatial spectrum of CF map along the azimuthal direction.

Figs. 6.1(a) and (b) shows the GCF map with M_0 = 1, and CF map that correspond to an anechoic cyst without aberrations, respectively. The vertical axis is the depth and the horizontal axis is the azimuth. Clearly, the GCF map is smoother than the CF map. In order to determine the cut-off frequency of the spatial low pass filter (LPF) used to smooth the CF, the lateral spatial spectrum of GCF, and CF along the azimuth direction are calculated at each imaging depth, as shown in Figs. 6.1 (d) and (e), respectively. In Figs. 6.1(d) and (e), the vertical axis is the depth, and the horizontal is the lateral spatial frequency. Note that the lateral spatial frequency is normalized such that 1 equals half of the sampling rate in the azimuth of CF and GCF maps (i.e., inverse of beam spacing). Since the variation of CF is larger than that of GCF, the spectrum of CF has more high frequency components than that of GCF. The spatial LPF in azimuth is designed according to the lateral spectra. The spectrum of GCF is viewed as the desired spectrum, the cut-off frequency of the desired LPF is set to 0.2 as indicated by the white dashed line shown in Fig. 6.1(d). A 17-tap LPF is applied with the coefficients determined by the MATLAB function “fir1”, that uses the window method to design a FIR filter (note that a hamming window is used here) [62]. The LPF{CF} map with the designed LPF is shown in Fig. 6.1(c).

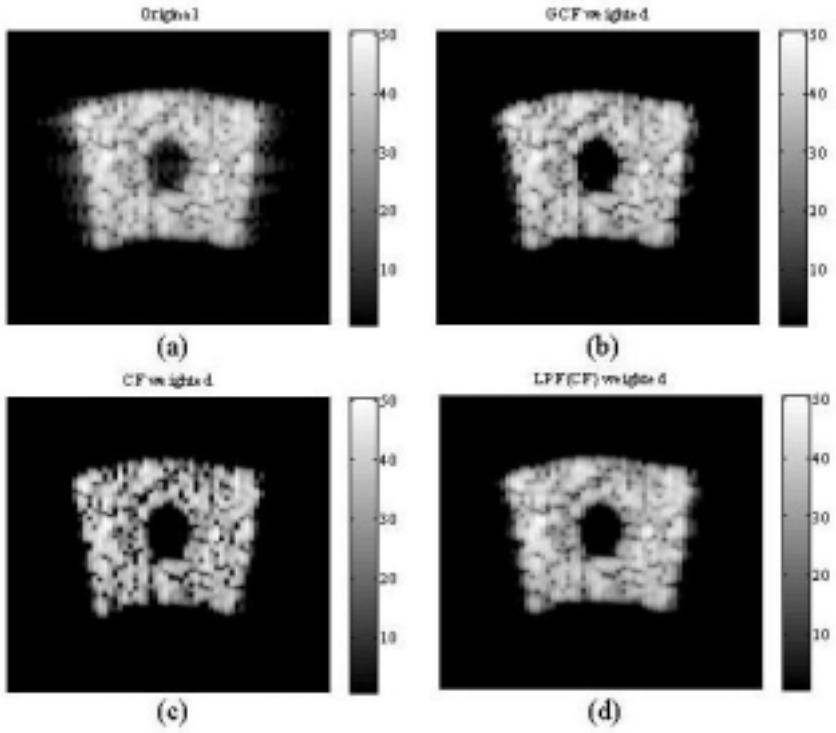

Fig. 6.2. Anechoic cyst images weighted by different weighting factor. (a) Original image; (b) GCF-weighted image; (c) CF-weighted image; (d) LPF{CF} weighted image.

The GCF, CF, and LPF(CF) maps shown in Fig. 6.1 are then applied as the weighting function to the original B-mode image and the weighted images are shown

in Fig. 6.2. Figs. 6.2(a), (b), (c), and (d) show the original B-mode, the GCF-weighted, the CF-weighted, and the LPF{CF} weighted images, respectively. Note the similar effectiveness in sidelobe reduction (or contrast improvement) between the GCF weighting and the LPF{CF} weighting.

When phase aberrations are present, effects of the two weighting functions on the CNR are also tested. Fig. 6.3 shows CNR after the various adaptive weighting schemes under different maximum phase errors. The LPF{CF} weighted images have similar CNR improvement to the GCF weighted ones, and LPF{CF} weighting has lower computational complexity than GCF weighting.

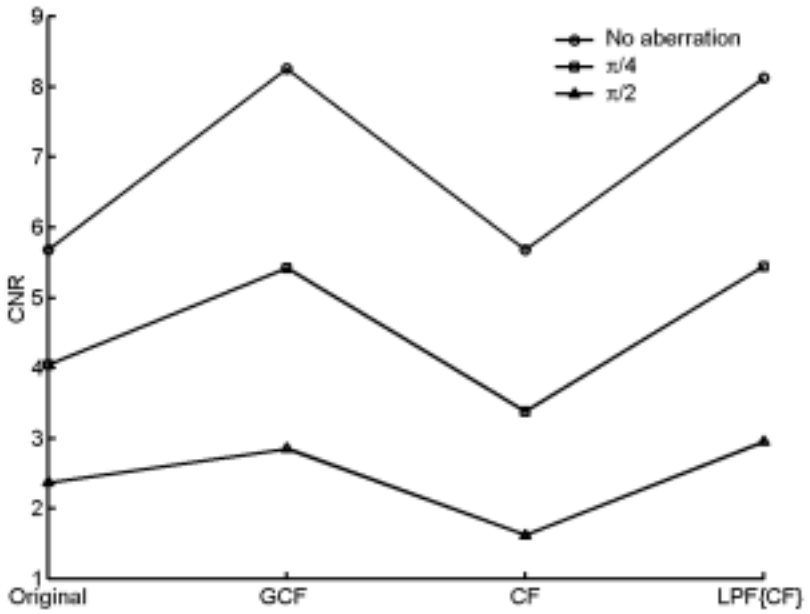

Fig. 6.3. CNR after various adaptive weighting under different maximum phase errors.

The above simulations test the LPF{CF} weighting at the transmit focal depth. To investigate effects of the transmit focal depth on the LPF{CF} weighting, simulated data in section (3.4.2) are used here (the transmit focal point moves from 30 mm to 60 mm while the cyst is still centered at 30 mm). Top panels in Fig. 6.4 shows the GCF, CF, and LPF{CF} maps of the anechoic cyst simulation without aberration when the cyst is around the transmit focus. Bottom panels in Fig. 6.4 are the GCF, CF, and LPF{CF} maps when the cyst is out of the transmit focal zone. Note that the GCF, CF, and LPF(CF) at the focus are higher than those out of the focus. In addition, the CF and the LPF(CF) are more sensitive to the transmit focus depth than the GCF (the value of CF decreases more than that of GCF). Thus, the performance of LPF{CF} weighting will be significantly degraded in the out-of-focused region. Nonetheless,

using LPF{CF} weighting to replace GCF weighting is still feasible in the focused region.

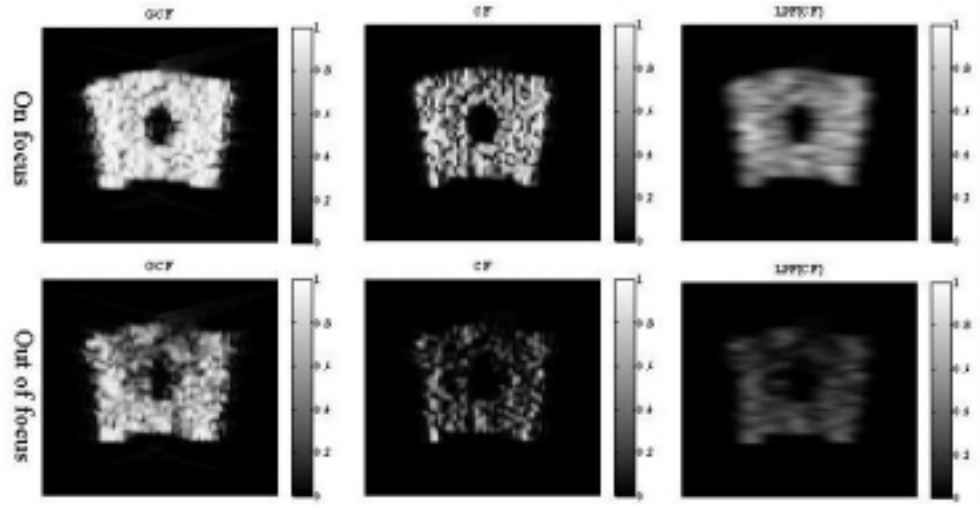

Fig. 6.4. On-focus and out-of-focus GCF, CF, and LPF{CF} maps of anechoic cyst simulation without aberration.

Another disadvantage for lateral filtering CF is the motion artifact. In particular, if the object moves by more than a quarter wavelength over the entire time needed to acquire all beams used to estimate LPF{CF}, significant motion artifacts will occur. As described in this chapter, 17 beams are needed to estimate LPF{CF} of one beam line because the lateral filter has 17 taps. Thus, the motion must be negligible during a period of 17 pulse repetition intervals. For a 160 mm image depth, the object should not move by more than a quarter wavelength in a period of about 3.6 ms. This represents a velocity of about 30 mm/s. Thus, tissue motion may be significant for cardiac applications and the motion must be corrected in order to apply the LPF{CF} weighting technique. Furthermore, because LPF{CF} is used in CF thresholding, the adaptive receive aperture technique proposed in chapter 3 may also be susceptible to motion. Potential degradation due to motion in different clinical situations needs to be further evaluated.

6.2 Combination of Two Adaptive Approaches

In this section, the adaptive receive aperture technique proposed in chapter 3 is combined with the adaptive weighting technique using LPF{CF} mentioned in the last section. LPF{CF} is also used for CF thresholding in the adaptive receive aperture technique. Hence, the LPF{CF} weighting technique can be directly

combined with the adaptive receive aperture technique with only a slight increase in system complexity. The simulated data in section (3.3) are used to test the combined method. The LPF and $CF_{threshold}$ used in this section are the same as those in section (3.3). Note that the CF that is low-pass filtered to be a weighting factor is estimated using the optimal receive aperture size from the adaptive receive aperture technique.

Fig. 6.5 shows the projected radiation patterns for the point target under different aberration conditions. Fig. 6.5(a) is the case for no aberration. Fig. 6.5(b) shows the aberrated case with a $\pi/4$ maximum phase error, and Fig. 6.5(c) is the case with a $\pi/2$ maximum phase error. Fig. 6.5 shows that sidelobes of the point images can be further suppressed by combining the adaptive receive aperture technique with the LPF{CF} weighting technique. The far sidelobes are all further suppressed by about 20 dB using the combined method. Note that the combined method does not increase the mainlobe width, but the adaptive receive aperture technique does.

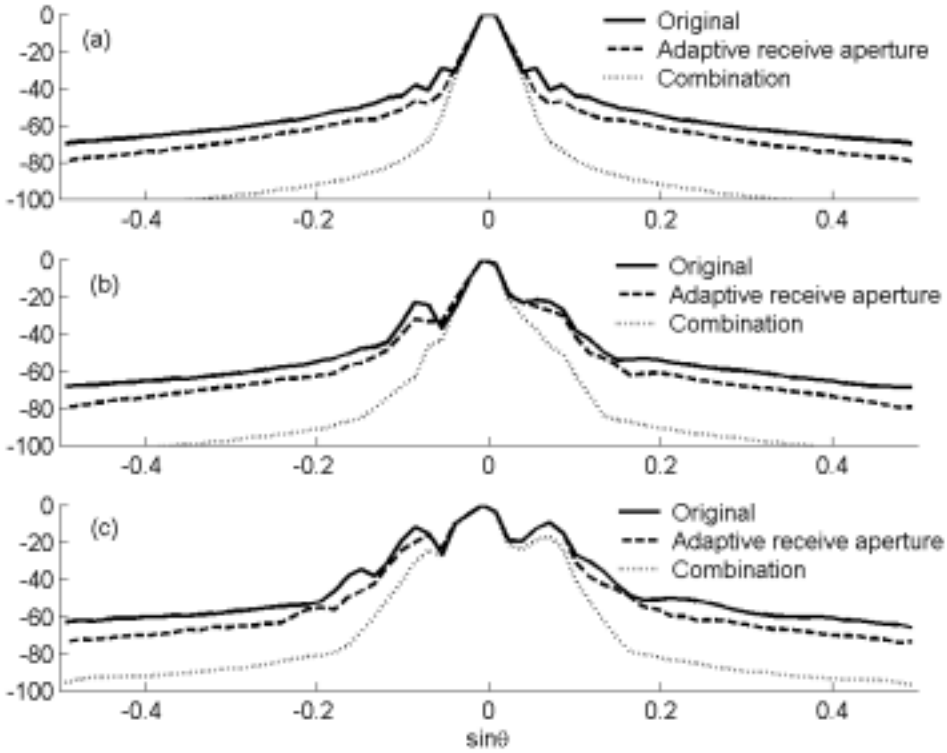

Fig. 6.5. Projected radiation patterns for a point target. (a) No aberration. (b) $\pi/4$ maximum phase error at the imaging frequency of 3.5 MHz. (c) $\pi/2$ maximum phase error. Solid lines, original radiation patterns; dashed lines, radiation patterns with the adaptive receive aperture technique; dotted lines, radiation patterns with the combined method

Figs. 6.6(a)–(c) show the simulated images with no distortion, $\pi/4$ maximum phase error, and $\pi/2$ maximum phase error, respectively. The top row shows the

original images; the middle row shows the images with the adaptive receive aperture technique; the bottom row shows the images with the combined method. Clearly, it is shown that detection of the cyst is further improved by combining the adaptive receive aperture technique with the LPF{CF} weighting technique.

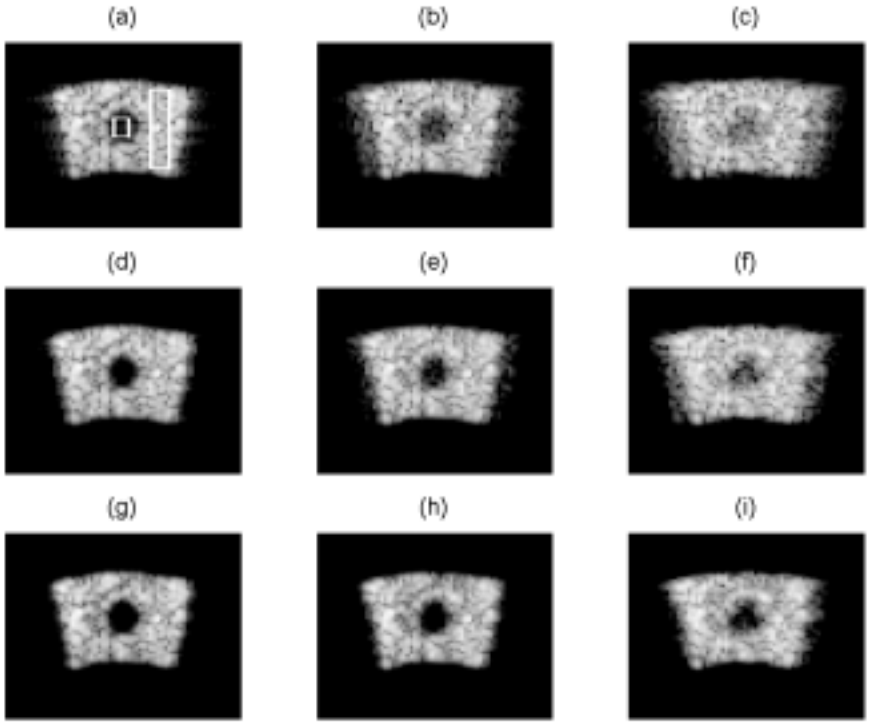

Fig. 6.6. Images of a phantom with an anechoic cyst over a 50 dB dynamic range. The vertical axis represents range and the horizontal axis is azimuth. The top row shows the original images; the middle row shows the images with the adaptive receive aperture technique; the bottom row shows the images with the combined method. (a), (d), and (g) No aberration. (b), (e), and (h) $\pi/4$ maximum phase error at the imaging frequency of 3.5 MHz. (c), (f), and (i) $\pi/2$ maximum phase error.

Figs. 6.7(a), (b), and (c) shows estimated standard deviation in the speckle background, CR and CNR of the cyst images, respectively (note that the right- and left-hand white boxes shown in Fig. 6.6(a) indicate the background and cyst regions, respectively). The solid lines with squares are the original values, the solid lines with circles are the corrected values with the adaptive receive aperture technique, and the solid lines with triangles are the corrected values with the combined method. It is shown that the combined method does not increase the speckle variance in the speckle background for all cases. CR and CNR are also significantly further improved using the combined method.

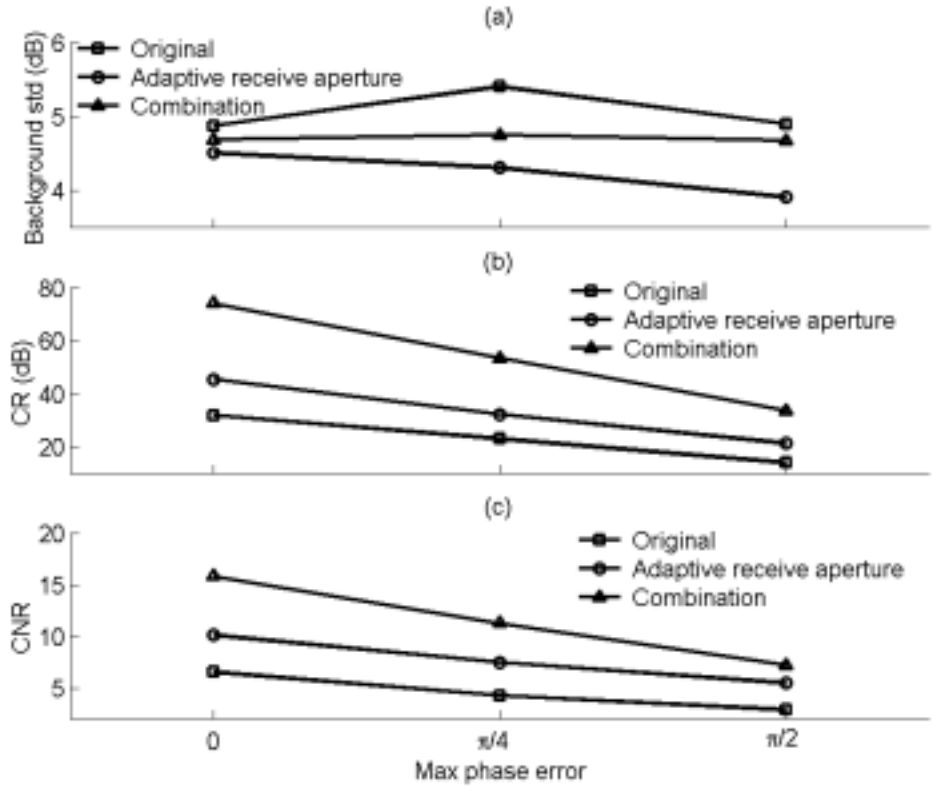

Fig. 6.7. Standard deviation in the speckle background, CR and CNR of the simulated images with an anechoic cyst for different maximum phase errors. 0 means no aberration. $\pi/4$ and $\pi/2$ represent maximum phase errors at the imaging frequency of 3.5 MHz. (a) Standard deviation in the speckle background. (b) CR. (c) CNR. Solid lines with squares, original; solid lines with circles, corrected with adaptive receive aperture technique; solid lines with triangles, corrected with the combined method.

Chapter 7 Conclusions and Future Works

Removing focusing errors resulting from sound-velocity inhomogeneities in human tissue is an important research topic in medical ultrasound imaging. Such focusing errors degrade image quality. In this dissertation, two adaptive sidelobe-reduction techniques – the adaptive weighting technique using GCF and the adaptive receive aperture technique using CF thresholding – are proposed to improve the degraded image quality. Both of the two proposed techniques are independent of the source of the artifacts and thus can be used to reduce other types of focusing errors. The two techniques can be implemented efficiently, and can be incorporated into current medical ultrasonic imaging systems with modest modifications. They both perform better than PARCA2, while their computational complexity and memory requirements are lower, and no iteration is needed. The simulations and experimental results demonstrate the effectiveness of the two proposed techniques: the elevated sidelobe level is effectively suppressed and contrast resolution is noticeably improved. The speckle variance can also be reduced by the adaptive receive aperture technique.

In this dissertation, we also extend the GCF weighting technique to FT-based parallel receive beam formation and high-frequency ultrasound imaging, and explore the feasibility using LPF{CF} weighting to replace GCF weighting. In the focused region, LPF{CF} can be used to replace GCF as the weighting factor in the adaptive weighting technique to further reduce the computational complexity. In addition, the image obtained using the adaptive receive aperture technique and its corresponding CF map can be combined to further improve image quality. For example, the adaptive receive aperture technique can be combined with the adaptive weighting technique using LPF{CF}.

Future works will extend the adaptive receive aperture technique to parallel receive beam formation and high-frequency imaging. The adaptive receive aperture technique has the potential to reduce image-intensity variations resulting from beam asymmetry in parallel receive beam formation. It also can be employed to suppress the high sidelobes of SAFT in high-frequency imaging. Moreover, it has been observed that on-axis and off-axis targets will produce different tilted wavefronts in the acquired channel data. This implies that lateral motion of imaging targets will also result in different tilted wavefronts in channel data acquired at different times. Hence, the slope change of the tilted wavefronts in the channel data is related to lateral velocity of imaging targets. Based on this property, to develop a new aperture domain

2D flow estimator is another work in the future.

References

[1] K. E. Thomenius, “Evolution of ultrasound beamformers,” in *Proc. IEEE Ultrason. Symp.*, 1996, pp. 1615–1622.

[2] S. H. Maslak and H. G. Larsen, “Dynamically focused linear phased array acoustic imaging system,” U.S. Patent 4 699 009, 1987.

[3] D. Lipschutz, “Delay interpolator for digital phased array ultrasound beamformers,” U.S. Patent 5 345 426, 1994.

[4] W. E. Engeler and C. M. W. Daft, “Ultrasonic imager having wide-bandwidth dynamic focusing,” U.S. Patent 5 488 588, 1996.

[5] M. O’Donnell, W. E. Engeler, J. J. Bloomer, and J. T. Pedicone, “Method and apparatus for digital phased array imaging,” U.S. Patent 4 983 970, 1991.

[6] A. Gee, C. R. Cole, and J. N. Wright, “Method and apparatus for focus control of transmit and receive beamformer systems,” U.S. Patent 5 581 517, 1996.

[7] W. E. Engeler, M. O’Donnell, J. T. Pedicone, and J. J. Bloomer, “Dynamic phase focus for coherent imaging beam formation,” U.S. Patent 5 111 695, 1992.

[8] M. O’Donnell, W. E. Engeler, and J. T. Pedicone et al., “Real-time phased array imaging using digital beam forming and autonomous channel control,” in *Proc. IEEE Ultrason. Symp.*, 1990, pp. 1499–1502.

[9] J. Y. Lu and J. Greenleaf, “Ultrasonic nondiffracting transducer for medical imaging,” *IEEE Trans. Ultrason., Ferroelect., Freq. Contr.*, vol. 37, no. 5, pp. 438–447, 1990.

[10] J. Y. Lu, “Designing limited diffraction beams,” *IEEE Trans. Ultrason., Ferroelect., Freq. Contr.*, vol. 44, no. 1, pp. 181–193, 1997.

[11] B. Haider, “Synthetic transmit focusing for ultrasonic imaging,” in *Proc. IEEE Ultrason. Symp.*, 2000, pp. 1215–1218.

[12] B. Robinson and C. Cooley, “Synthetic dynamic transmit focus,” in *Proc. IEEE Ultrason. Symp.*, 2000, pp. 1209–1214.

[13] M. H. Bae and M. K. Jeong, “A study of synthetic-aperture imaging with virtual source elements in B-mode ultrasound imaging systems,” *IEEE Trans. Ultrason., Ferroelect., Freq. Contr.*, vol 47, no. 6, pp. 1510–1518, 2000.

[14] S. Freeman, P.-C. Li, and M. O’Donnell, “Retrospective dynamic transmit focusing,” *Ultrason. Imaging*, vol. 17, no. 3, pp. 173–196, 1995.

[15] M.-L Li and P.-C. Li, “Filter-based synthetic transmit and receive focusing,” *Ultrason. Imaging*, vol. 23, no. 2, pp. 73–89, 2001.

[16] L. M. Hinkelman, D. L. Liu, R. C. Waag, Q. Zhu, and B. D. Steinberg, “Measurement and correction of ultrasonic pulse distortion produced by the human breast,” *J. Acoust. Soc. Am.*, vol. 97, no. 3, pp. 1958–1969, 1995.

[17] L. M. Hinkelman, D. L. Liu, L. A. Metlay, and R. C. Waag, “Measurements of ultrasonic pulse arrival time and energy level variations produced by propagation through abdominal wall,” *J. Acoust. Soc. Am.*, vol. 95, no. 1, pp. 530–541, 1994.

[18] S. W. Flax and M. O’Donnell, “Phase-aberration correction using signals from point reflectors and diffuse scatterers: basic principles,” *IEEE Trans. Ultrason., Ferroelect., Freq. Contr.*, vol. 35, no. 6, pp. 758–767, 1988.

[19] M. O’Donnell and S. W. Flax, “Phase-aberration correction using signals from point reflectors and diffuse scatterers: measurements,” *IEEE Trans. Ultrason., Ferroelect., Freq. Contr.*, vol. 35, no. 6, pp. 768–774, 1988.

[20] S. Krishnan, K. W. Rigby, and M. O’Donnell, “Improved estimation of phase aberration profile,” *IEEE Trans. Ultrason., Ferroelect., Freq. Contr*., vol. 44, no. 3, pp. 701–713, 1997.

[21] D. L. Liu and R. C. Waag, “Correction of ultrasonic wavefront distortion using backpropagation and a reference waveform method for time-shift compensation,” *J. Acoust. Soc. Am.*, vol. 96, no. 2, pp. 649–660, 1994.

[22] G. C. Ng, P. D. Freiburger, W. F. Walker, and G. E. Trahey, “A speckle target adaptive imaging technique in the presence of distributed aberrations,” *IEEE Trans. Ultrason., Ferroelect., Freq. Contr.*, vol. 44, no. 1, pp. 140–151, 1997.

[23] P.-C. Li and M. O’Donnell, “Phase aberration correction on two-dimensional conformal arrays,” *IEEE Trans. Ultrason., Ferroelect., Freq. Contr.*, vol. 42, no. 1, pp. 73–82, 1995.

[24] W. F. Walker and G. E. Trahey, “Aberrator integration error in adaptive imaging,” *IEEE Trans. Ultrason., Ferroelect., Freq. Contr.*, vol. 44, no. 4, pp. 780–791, 1997.

[25] D. L. Liu and R. C. Waag, “A comparison of ultrasonic wavefront distortion and compensation in one-dimensional and two-dimensional apertures,” *IEEE Trans. Ultrason., Ferroelect., Freq. Contr.*, vol. 42, no. 4, pp. 726–733, 1995.

[26] P.-C. Li, S. W. Flax, E. S. Ebbini, and M. O’Donnell, “Blocked element compensation in phased array imaging,” *IEEE Trans. Ultrason., Ferroelect., Freq. Contr.*, vol. 40, no. 4, pp. 283–292, 1993.

[27] P.-C. Li and M. O’Donnell, “Improved detectability with blocked element compensation,” *Ultrason. Imaging*, vol. 16, no. 1, pp. 1–18, 1994.

[28] S. Krishnan, P.-C. Li, and M. O’Donnell, “Adaptive compensation of phase and magnitude aberrations,” *IEEE Trans. Ultrason., Ferroelect., Freq. Contr.,* vol. 43, no. 1, pp. 44–55, 1996.

[29] S. Krishnan, K. W. Rigby, and M. O’Donnell, “Efficient parallel adaptive aberration correction,” *IEEE Trans. Ultrason., Ferroelect., Freq. Contr.,* vol. 45, no. 3, pp. 691–703, 1998.

[30] D.-L.D., Liu, P. Von Behren, and J. Kim, “Single transmit imaging,” in *Proc. IEEE Ultrason. Symp.*, 1999, pp. 1275–1278.

[31] M. O’Donnell, “Efficient parallel receive beam forming for phased array imaging using phase rotation,” in *Proc. IEEE Ultrason. Symp.*, 1990, pp. 1495–1498.

[32] K. W. Hollman, K. W. Rigby, and M. O’Donnell, “ Coherence factor of speckle from a multi-row probe,” in *Proc. IEEE Ultrason. Symp.*, 1999, pp. 1257–1260.

[33] K. W. Rigby, “Method and apparatus for coherence filtering of ultrasound images,” U.S. Patent 5 910 115, 1999.

[34] R. Mallart and M. Fink, “Adaptive focusing in scattering media through sound-speed inhomogeneities: The van Cittert-Zernike approach and focusing criterion,” *J. Acoust. Soc. Am.*, vol. 96, no. 6, pp. 3721–3732, 1994.

[35] S. D. Silverstein, “Ultrasound scattering model: 2-D cross-correlation and focusing criteria – theory, simulations, and experiments,” *IEEE Trans. Ultrason., Ferroelect., Freq. Contr.*, vol. 48, no. 4, pp. 1023–1030, 2001.

[36] J. A. Jensen, “Field: a program for simulating ultrasound systems,” *Med. Biol. Eng. Comput.*, vol. 34, pp. 351–359, 1996.

[37] D. P. Shattuck, M. D. Weinshenker, S. W. Smith, and O. T. von Ramm, “ Explososcan: a parallel processing technique for high speed ultrasound imaging with linear phased arrays,” *J. Acoust. Soc. Am.* vol. 75, pp. 1273–1282, 1984.

[38] S. W. Smith, H. G. Pavy Jr, and O. T. von Ramm, “High-speed ultrasound volumetric imaging system – Part I: transducer design and beam steering,” *IEEE Trans. Ultrason., Ferroelect., Freq. Contr.* vol. 38, pp. 100–108, 1991.

[39] O. T. von Ramm, S. W. Smith, and H. G. Pavy Jr, “High-speed ultrasound volumetric imaging system – Part II: parallel processing and image display,” *IEEE Trans. Ultrason., Ferroelect., Freq. Contr.* vol. 38, pp. 109–115, 1991.

[40] B. Delannoy, R. Torguet, C. Bruneel, E. Bridoux, J. M. Rouvaen, and H. LaSota, “Acoustical image reconstruction in parallel-processing analog electronics systems,” *J. Appl. Phys.* vol. 50, pp. 3153–3159, 1979.

[41] A. Koyano, Y. Yoshikawa, T. Konishi, Y. Kobayashi, Y. Kimita, T. Hidai, N. Okasda, C. Hayashi, and K. Fujie, “A high quality ultrasound imaging system using linear array transducer,” *Ultrasound Med. Biol.* vol. 8, pp. 100, 1982.

[42] F. N. Ucar and M. Karaman, “Beam spacing processing for low-cost scanners,” in *Proc. IEEE Ultrason. Symp.*, 1996, pp. 1349–1352.

[43] M. Berson, L. Vaillant, F. Vaillant, P. Vaillant, and L. Pourcelot, “High-resolution real-time ultrasonic scanner,” *Ultrasound Med. Biol.*, vol. 18, no. 5, pp. 471–478, 1992.

[44] G. R. Lockwood, D. H. Turnbull, D. A. Christopher, and F. S. Foster, “Beyond 30 MHz – applications of high frequency ultrasound imaging,” *IEEE Eng. Med. Biol. Mag.*, vol. 15, no. 6, pp. 60–71, 1996.

[45] F. L. Lizzi, C. X. Deng, E. J. Feleppa, D. J. Coleman, and R. H. Silverman,, “Three-dimensional biometric images of ocular structures using very-high-frequency ultrasound,” in *Proc. IEEE Ultrason. Symp.*, 1999, pp. 1581–1583.

[46] W. H. Chen, E. J. Gottlieb, J. M. Cannata, Y. F. Chen, and K. K. Shung, “Development of sector scanning ultrasonic backscatter microscope,” in *Proc.*

IEEE Ultrason. Symp., 2000, pp. 1681–1684.

[47] D. A. Knapik, B. Starkoski, C. J. Pavlin, and F. S. Foster, " A 100–200 MHz ultrasound biomicroscope," *IEEE Trans. Ultrason., Ferroelect., Freq. Contr.*, vol. 47, no. 6, pp. 1540–1549, 2000.

[48] F. S. Foster, C. J. Pavlin, K. A. Harasiewicz, D. A. Christopher, and D. H. Turnbull, "Advances in ultrasound biomicroscopy," *Ultrasound Med. Biol.*, vol. 26, no. 1, pp. 1–27, 2000.

[49] S. Erickson, D. Kruse, and K. Ferrara, "A hand-held, high frequency ultrasound scanner," in *Proc. IEEE Ultrason. Symp.*, 2001, pp. 1465–1468.

[50] C. Passmann and H. Ermert, "In vivo imaging of the skin in the 100 MHz region using the synthetic aperture concept," in *Proc. IEEE Ultrason. Symp.*, 1995, pp. 1287–1290.

[51] C. Passmann and H. Ermert, "A 100-MHz ultrasound imaging system for dermatologic and ophthalmologic diagnostics," *IEEE Trans. Ultrason., Ferroelect., Freq. Contr.*, vol. 43, no. 4, pp. 545–552, 1996.

[52] G. H. Frazier and W. D. O'Brien, "Synthetic aperture technique with a virtual source element," *IEEE Trans. Ultrason., Ferroelect., Freq. Contr.*, vol. 45, no. 1, pp. 196–207, 1998.

[53] M. Karaman, P.-C. Li, and M. O'Donnell, "Synthetic aperture imaging for small scale systems," *IEEE Trans. Ultrason., Ferroelect., Freq. Contr.*, vol. 42, no. 3, pp. 429–442, 1995.

[54] M.-H. Bae and M.-K. Jeong, "A study of synthetic-aperture imaging with virtual source elements in B-mode ultrasound imaging systems," *IEEE Trans. Ultrason., Ferroelect., Freq. Contr.*, vol. 47, no. 6, pp. 1510–1519, 2000.

[55] W. Masri, M. Mina, S. S. Udpa, L. Upda, T. Xue, and W. Lord, "Synthetic aperture focusing techniques applied in the near field of a focused transducer," in *Proc. IEEE Ultrason. Symp.*, 1995, pp. 783–786.

[56] T. Christopher, "Finite amplitude distortion-based inhomogeneous pulse echo ultrasonic imaging," *IEEE Trans. Ultrason., Ferroelect., Freq. Contr.*, vol. 44, no. 1, pp. 125–139, 1997.

[57] T. Christopher, "Experimental investigation of finite amplitude distortion-based

inhomogeneous pulse echo ultrasonic imaging," *IEEE Trans. Ultrason., Ferroelect., Freq. Contr.*, vol. 45, no. 1, pp. 158–162, 1998.

[58] D. H. Simpson and P. N. Burns, "Pulse inversion Doppler: A new method for detecting nonlinear echoes from microbubble contrast agent," in *Proc. IEEE Ultrason. Symp.*, 1997, pp. 1597–1600.

[59] D. H. Simpson, C. T. Chin, and P. N. Burns, "Pulse inversion Doppler: A new method for detecting nonlinear echoes from microbubble contrast agent," *IEEE Trans. Ultrason., Ferroelect., Freq. Contr.*, vol. 46, no. 2, pp. 372–382, 1999.

[60] C.-C. Shen and P.-C. Li, "Harmonic leakage and image quality degradation in tissue harmonic imaging," *IEEE Trans. Ultrason., Ferroelect., Freq. Contr.*, vol. 48, no. 3, pp. 728–736, 2001.

[61] E. Cherin, J. K. Poulsen, A. F. W. Van der Steen, and F. S. Foster, "Comparison of nonlinear and linear imaging techniques at high frequency," in *Proc. IEEE Ultrason. Symp.*, 2000, pp. 1639–1643.

[62] A. V. Oppenheim, R. W. Schafer, and J. R. Buck, "Discrete-time signal processing," 2nd ed., Prentice-Hall, N.J., 1998.

Publication List

Journal Papers

[1] Meng-Lin Li and Pai-Chi Li, “Filter-based synthetic transmit and receive focusing,” *Ultrason. Imaging*, vol. 23, pp. 73–89, 2001.

[2] Po-Ling Kuo, Pai-Chi Li and Meng-Lin Li, "Elastic properties of tendon measured by two different approaches," *Ultrasound in Med. & Biol.*, vol. 27, no. 9, pp. 1275–1284, 2001.

[3] Wen-Chun Yeh, Pai-Chi Li, Yung-Ming Jeng, Hey-Chi Hsu, Po-Lin Kuo, Meng-Lin Li, Pei-Ming Yang and Po Huang Lee, "Elastic modulus measurements of human liver and correlation with pathology", *Ultrasound in Med. & Biol.*, vol. 28, no. 4, pp. 467–474, 2002.

[4] Pai-Chi Li and Meng-Lin Li, “Adaptive imaging using the generalized coherence factor,” *IEEE Trans. Ultrason., Ferroelec., Freq. Contr.*, vol. 50, no. 2, pp. 128 – 141, 2003.

[5] Meng-Lin Li and Pai-Chi Li, “Improved Fourier-transform-based parallel receive beam formation,” *Ultrason. Imaging*, vol. 25, pp. 73–84, 2003.

[6] Meng-Lin Li, Wei-Jung Guan, and Pai-Chi Li, “Improved synthetic aperture focusing technique with applications in high-frequency ultrasound imaging,” *IEEE Trans. Ultrason., Ferroelec., Freq. Contr.*, vol. 51, no. 1, pp. 63 – 70, 2004.

[7] Meng-Lin Li, Sheng-Wen Huang, and Pai-Chi Li, “Adaptive imaging using the optimal receive aperture size,” (submitted) *IEEE Trans. Ultrason., Ferroelec., Freq. Contr.*

Conference Presentations

[1] M.-L. Li and P.-C. Li, “Filter-based synthetic aperture imaging for ultrasonic imaging,” Symposium of Annual Conference of the Biomedical Engineering Society, Taipei, Taiwan, R.O.C., December 15-16, 2000.

[2] M.-L. Li and P.-C. Li, “Filter-based synthetic two-way focusing for ultrasonic imaging,” Symposium of Annual Conference of the Biomedical Engineering

Society, Taipei, Taiwan, R.O.C., December 15-16, 2001.

[3] M.-L. Li and P.-C. Li, “A new adaptive imaging technique using generalized coherence factor,” in *Proc. IEEE Ultrason. Symp.*, 2002, pp. 1627–1630.

[4] M.-L. Li and P.-C. Li, “Generalized coherence factor based ultrasonic adaptive imaging,” Symposium of Annual Conference of the Biomedical Engineering Society, Taipei, Taiwan, R.O.C., December 14-15, 2002.

[5] M.-L. Li, W.-J. Guan, and P.-C. Li, “Sidelobe reduction for synthetic aperture focusing in high-frequency ultrasonic imaging,” in *Proc. IEEE Ultrason. Symp.*, 2003.

[6] M.-L. Li, W.-J. Guan, and P.-C. Li, “Weighted Synthetic Aperture Focusing with Applications in High-Frequency Ultrasonic Small Animal Imaging,” Symposium of Annual Conference of the Biomedical Engineering Society, Taipei, Taiwan, R.O.C., December 12-13, 2003.